

1-1-2003

The design and performance of an x-ray emission spectrometer using the polarized K α spectra of chlorine and potassium

Amanda C Hudson
University of Nevada, Las Vegas

Follow this and additional works at: <https://digitalscholarship.unlv.edu/rtds>

Repository Citation

Hudson, Amanda C, "The design and performance of an x-ray emission spectrometer using the polarized K α spectra of chlorine and potassium" (2003). *UNLV Retrospective Theses & Dissertations*. 1597.
<http://dx.doi.org/10.25669/fqe4-ikzi>

This Thesis is protected by copyright and/or related rights. It has been brought to you by Digital Scholarship@UNLV with permission from the rights-holder(s). You are free to use this Thesis in any way that is permitted by the copyright and related rights legislation that applies to your use. For other uses you need to obtain permission from the rights-holder(s) directly, unless additional rights are indicated by a Creative Commons license in the record and/or on the work itself.

This Thesis has been accepted for inclusion in UNLV Retrospective Theses & Dissertations by an authorized administrator of Digital Scholarship@UNLV. For more information, please contact digitalscholarship@unlv.edu.

NOTE TO USERS

Page(s) missing in number only; text follows. Page(s) were scanned as received.

88

This reproduction is the best copy available.

UMI[®]

THE DESIGN AND PERFORMANCE OF AN X-RAY EMISSION
SPECTROMETER USING THE POLARIZED $K\alpha$
SPECTRA OF CHLORINE AND POTASSIUM

by

Amanda C. Hudson

Bachelor of Science in Chemistry
University of Nevada, Reno
2001

thesis submitted in partial fulfillment
of the requirements for the

Master of Science Degree in Chemistry
Department of Chemistry
College of Sciences

Graduate College
University of Nevada, Las Vegas
December 2003

UMI Number: 1417774

INFORMATION TO USERS

The quality of this reproduction is dependent upon the quality of the copy submitted. Broken or indistinct print, colored or poor quality illustrations and photographs, print bleed-through, substandard margins, and improper alignment can adversely affect reproduction.

In the unlikely event that the author did not send a complete manuscript and there are missing pages, these will be noted. Also, if unauthorized copyright material had to be removed, a note will indicate the deletion.

UMI[®]

UMI Microform 1417774

Copyright 2004 by ProQuest Information and Learning Company.

All rights reserved. This microform edition is protected against unauthorized copying under Title 17, United States Code.

ProQuest Information and Learning Company
300 North Zeeb Road
P.O. Box 1346
Ann Arbor, MI 48106-1346



Thesis Approval

The Graduate College
University of Nevada, Las Vegas

November 19, 20 03

The Thesis prepared by

Amanda C. Hudson

Entitled

The Design and Performance of an X-Ray Emission Spectrometer Using
the Polarized K Alpha Spectra of Chlorine and Potassium

is approved in partial fulfillment of the requirements for the degree of

Master Of Science

Examination Committee Chair

Dean of the Graduate College

Examination Committee Member

Examination Committee Member

Graduate College Faculty Representative

ABSTRACT

The Design and Performance of an X-Ray Emission Spectrometer using the Polarized $K\alpha$ Spectra of Chlorine and Potassium

by

Amanda C. Hudson

Dr. Dennis W. Lindle, Examination Committee Chair
Professor of Chemistry
University of Nevada, Las Vegas

The x-ray emission spectrometer was designed to observe the polarization of x-ray fluorescence resulting from the excitation of a sample by synchrotron radiation. The incident photons are intense, monoenergetic and linearly polarized along the plane of the storage-ring orbit. The emission spectrometer records the entire $K\alpha$ spectrum by dispersing the emitted radiation with a curved Si (111) crystal and detecting the resulting radiation with a resistive anode position sensitive detector; both of which are situated on a Rowland circle. A sample is fixed in position and located in the middle of the Rowland circle. The spectrometer can be positioned to detect fluorescence emitted at 0° and 90° with respect to the polarization/propagation direction of the incident x-rays. In KCl, there was no observable polarization dependence of the emission spectra at the chlorine edge and a large effect seen in potassium below the ionization threshold. There were also small effects seen in freon-13 when excitations were to Rydberg states.

TABLE OF CONTENTS

ABSTRACT.....	iii
LIST OF FIGURES	vi
LIST OF TABLES.....	vii
ACKNOWLEDGEMENTS.....	viii
CHAPTER 1 INTRODUCTION	1
Spectroscopic Methods	3
CHAPTER 2 THEORY	11
Time Perturbation Theory.....	11
Stimulated Absorption	13
Spontaneous Emission	16
Dipole Selection Rules.....	18
CHAPTER 3 REVIEW OF RELATED LITERATURE.....	20
Gas-Phase Soft X-Ray Regime	20
N ₂	20
O ₂	22
CO ₂	23
CO	26
Gas-Phase Hard X-Ray Regime: Methyl Chloride.....	29
Chlorofluoromethanes.....	30
H ₂ S	35
Liquids (H ₂ O).....	36
Non-Dipole X-Ray Emission.....	37
CHAPTER 4 EXPERIMENTAL SET-UP	39
Advanced Light Source (ALS)	39
X-Ray Emission Spectrometer (XES)	39
Electronics.....	46
Sample Holders.....	48
Alignment	51
XES Testing.....	53
Software	53
KCl.....	56
Freon-13.....	57

CHAPTER 5	RESULTS AND DISCUSSION.....	58
	KCl.....	58
	Chlorine Edge	58
	Potassium Edge.....	70
	Freon-13.....	79
CHAPTER 6	CONCLUSION	90
APPENDIX I	93
APPENDIX II	94
REFERENCES	101
VITA	103

LIST OF FIGURES

Figure 1	Bonding and Anti-bonding Representation	2
Figure 2	Absorption and Photoelectron Production.....	5
Figure 3	Photon and Auger Electron Emission.....	8
Figure 4	Resonant X-ray Emission	9
Figure 5	Flow Diagram of the X-ray Emission Spectrometer	40
Figure 6	Schematic of the X-ray Emission Spectrometer.....	42
Figure 7	Emission Spectrometer Electronic Rack	47
Figure 8	Interlock Boxes.....	49
Figure 9	Gas Cell Schematic.....	51
Figure 10	Alignment of the Emission Spectrometer.....	52
Figure 11	Rotation of the Detector Image using Igor	55
Figure 12	Generating a Spectra using Igor	56
Figure 13	Total Fluorescence Yields of Chlorine and Potassium Near the K-edge	59
Figure 14	Emission Spectra of Chlorine at 2826 eV	60
Figure 15	Emission Spectra of Chlorine at 2830 eV	62
Figure 16	Emission Spectra of Chlorine at 2832 eV	63
Figure 17	Emission Spectra of Chlorine at 2836.3 eV	65
Figure 18	Emission Spectra of Chlorine at 2845.5 eV	66
Figure 19	Emission Spectra of Chlorine at 2853.2 eV	68
Figure 20	Emission Spectra of Chlorine at 2875 eV	69
Figure 21	Emission Spectra of Potassium at 3612.4 eV	71
Figure 22	Emission Spectra of Potassium at 3616 eV	72
Figure 23	Emission Spectra of Potassium at 3618 eV	74
Figure 24	Emission Spectra of Potassium at 3621.4 eV	75
Figure 25	Emission Spectra of Potassium at 3629.1 eV	77
Figure 26	Emission Spectra of Potassium at 3645 eV	78
Figure 27	Emission Spectra of Potassium at 3670 eV	80
Figure 28	Absorption Scan Near the Chlorine K-edge in CF ₃ Cl.....	81
Figure 29	Cl Emission Spectra of CF ₃ Cl at 2824.3	83
Figure 30	Cl Emission Spectra of CF ₃ Cl at 2828.7	84
Figure 31	Cl Emission Spectra of CF ₃ Cl at 2830	86
Figure 32	Cl Emission Spectra of CF ₃ Cl at 2845	87
Figure 33	Cl Emission Spectra of CF ₃ Cl at 2875	89

LIST OF TABLES

Table 1	Emission Bands for N ₂	21
Table 2	Emission Bands for O ₂	23
Table 3	O-K Emission Bands for CO	27
Table 4	Cl K-V X-ray Emission Bands in CF ₃ Cl	32
Table 5	Cl K-V X-ray Emission Bands for CFC1 ₃	33
Table 6	Cl K-V X-ray Emission Bands of CF ₂ Cl ₂	33
Table 7	Preliminary Testing of the Emission Spectrometer's Energy Range	53

ACKNOWLEDGEMENTS

I would like to thank the following people for their knowledge and expertise: Dr. Wayne Stolte for knowing so much about running an experiment, Dr. Renaud Guillemin for being an expert with Igor, Dr. Dennis Lindle for being the group expert on just about everything (especially x-ray emission spectroscopy and wine), Dr. Ania Wolska for watching the “kids” when things got hectic at the beamline, and my mother Georgeanne Hess and my aunt Sue Morris for being ever supportive of my goals. I would also like to thank Mark and Debbie in the chemistry office for being my “legs” in Las Vegas on many occasions.

Finally, I would like to thank my committee members, Dr. Vernon Hodge, Dr. Boyd Earl, and Dr. James Selser for taking the time to help improve the content of this work.

CHAPTER 1

INTRODUCTION

In 1808, John Dalton presented his theory of atoms in *A New System of Chemical Philosophy*. Dalton postulated that each element is made up of tiny particles called atoms and that atoms of a given element are identical, and those of unlike elements differ in some fundamental way. J. J. Thompson used partially evacuated cathode-ray tubes to produce a stream of negatively charged particles emanating from a negative electrode and found that they were repelled by the negative pole of an applied electric field. The particles produced in the tube were later named electrons. Ernest Rutherford then discovered the nucleus in 1911 by bombarding a thin gold foil with α particles. From the scatter of the particles, he postulated that there was a center of concentrated positive charge, which contains most of the atom's mass, and that the electrons surround the nucleus. Finally, using the emission spectrum of hydrogen, previously studied by Balmer and Rydberg, and the wave/particle duality postulated by de Broglie, quantum mechanics was developed to explain the physics that classical mechanics could not.

The electrons in a system can be described using a set of four quantum numbers; n , the principle quantum number which designates the energy level of the electron, l the angular momentum quantum number which states which type of orbital the electron is in (s, p, d, f), m_l , the magnetic quantum number which describes the orbital's orientation in space (p_x , p_y , p_z , ect.) , and m_s , or the spin of the electron ($\pm \frac{1}{2}$). The combination of

these quantum numbers leads to orbital designation; for example a 2s electron has quantum numbers 2, 0, 0, $\pm \frac{1}{2}$, respectively. The outermost orbitals, the valence orbitals, in an atom can be combined with those from another atom to produce chemical bonds. The bonding electrons depend mainly on the shared chemical environment, while the tightly bound core electrons remain largely atomic in nature. Molecular orbitals are approximated using linear combinations of atomic hydrogen orbitals; see Figure 1. In this approximation, a 1s orbital from atom A and 1s orbital from atom B atom would be combined to form a bonding orbital, $\psi = c_1\phi_{1sA} + c_2\phi_{1sB}$, and an antibonding orbital, $\psi = c_1\phi_{1sA} - c_2\phi_{1sB}$, ect.

Spectroscopic Methods

Fundamental investigations in spectroscopy have led to our understandings of the electronic structures of atoms and the geometry and bonding of different molecules. Infrared (IR) spectroscopy has been used to study the vibrations of different functional groups in molecules. It is frequently used by organic chemists to identify vibration, rotation, and bending of chemical bonds. In IR spectroscopy, the molecule retains its electronic ground state. Radiation in the frequency is typically from 0.01 to 2 eV and is often used to help identify unknown compounds. Ultraviolet (UV) spectroscopy is typically used to study valence shell electrons. The binding energies of valence electrons are on the order of 5-20 eV, which falls in the UV range.

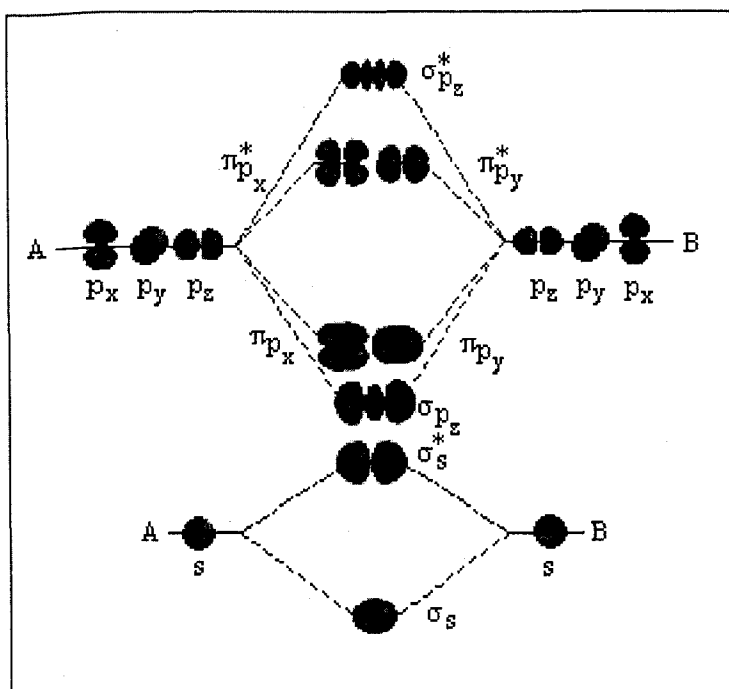


Figure 1. Bonding and antibonding representation of sigma and pi orbitals between atom A and atom B are represented here. In this diagram, antibonding, or destructive interference, is represented with an *.

To study core electrons, or those tightly bound to the nucleus, higher energy photons are used, namely x-rays. X-rays have energies between 15 and 150,000 eV and are usually divided into two different regions: soft x-rays and hard x-rays. Soft x-rays are lower in energy and are not energetic enough to penetrate the skin. Hard x-rays are highly energetic and are able to penetrate the skin, and therefore can be useful in medicine. X-rays can be produced by fast electrons stopping suddenly, by ionization of core electrons in an atom, or by acceleration of a charged particle. In space, they can also be produced by high energy processes such as gases being sucked in to a black hole and becoming compressed or by the explosions of stars. The waves are small enough to pass

between atoms and molecules so they can be used to determine molecular structures (the wavelengths of x-rays are typically smaller than the radii of core orbitals).

X-rays can interact with matter in a number of different ways; x-rays can be absorbed by an atom or a molecule and x-rays can interact with core electrons to produce a photoelectron, both processes result in an excited system. Atoms or molecules that have been excited can relax in the following ways: an electron fills the core hole and an Auger electron is emitted, or a photon of light can be emitted. Resonant x-ray emission occurs when absorption to bound states is followed by a relaxation of an electron into the core hole.

In x-ray absorption, a photon of light interacts with a core electron to promote it to a higher energy state or to ionize it; see Figure 2. The interacting photon gives up some of its energy and therefore has less energy, or $E_0 > E$, where E_0 is the energy of the incident radiation and E is the energy of the final radiation. The difference between the energies E_0 and E is equal to the energy difference between the initial and the final state of the electron. X-ray absorption is used to evaluate unoccupied electronic states, since the electrons are promoted to these orbitals. Two types of x-ray absorption measurements are conducted, extended x-ray absorption fine structure (EXAFS) and near edge x-ray absorption fine structure (NEXAFS). In EXAFS, the energy is extended beyond the absorption edge; usually about 400-1000 eV above the edge; the shortened range is due to limitations caused by experimental noise and/or by the presence of another absorption edge. In the experiment, the energy E of the x-ray photon is varied from several hundred electron-volts below the absorption edge up to about 1000 eV above the edge, and the x-ray absorption coefficient $\mu(E)$ is determined. Modulations in

the absorption coefficient provide structural information of molecules or solid in question [1]. NEXAFS is a much more difficult measurement to make, the ejected electrons are much less energetic because measurements are conducted only a few eV away from the ionization threshold. A simple kinematic theory cannot describe the behavior of these electrons, a more complex multi-scatter technique must be used (a computer generates theoretical spectra based on user supplied chemical structures that is then compared to experimental data). NEXAFS is useful in that it provides structural information about surfaces of materials, bulk materials, and isolated molecules. Near edge spectra yield information on coordinate geometry, molecular orientation, and density and symmetry of unoccupied valence electron states [2].

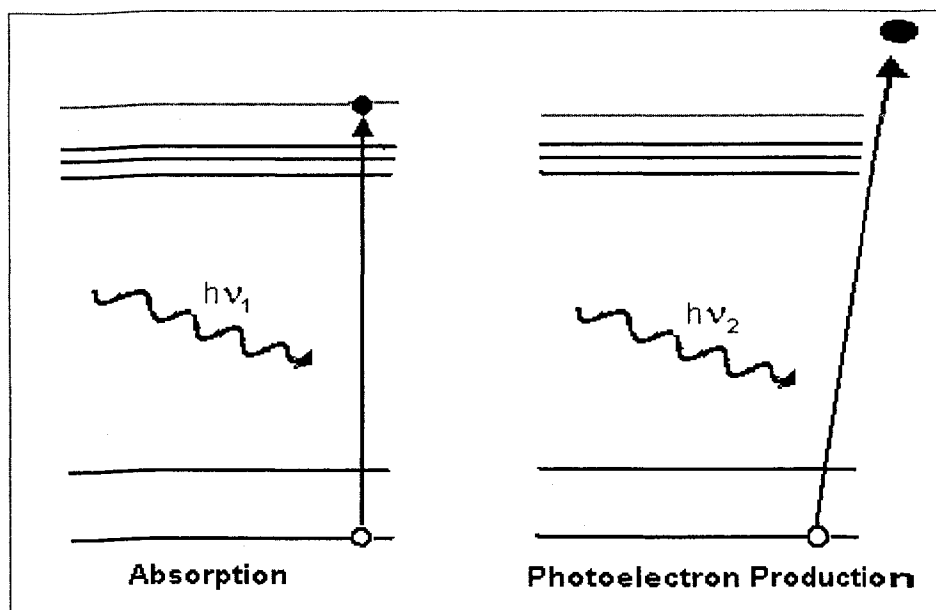
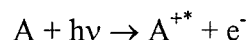


Figure 2. Illustration of photon absorption by an electron and the production of a photoelectron from a photon-electron interaction.

X-rays are energetic enough to ionize an atom or a molecule and produce a photoelectron, see Figure 2. One of the photons from an x-ray beam displaces an electron from a core orbital as follows:



where A can be an atom, molecule, or an ion, A^{+*} is an electronically excited ion with a positive charge one greater than that of A, $h\nu$ is the photon energy and e^{-} is an electron that is emitted as the result of the interaction. The kinetic energy of the emitted electron can be measured with an electron spectrometer, and thus the binding energy of the electron to the nucleus can be calculated using the following:

$$E_b = h\nu - E_k$$

where E_b is the electron binding energy and E_k is the kinetic energy of the electron.

When an electron absorbs a photon, part of the absorbed photon energy is used to overcome the forces holding the electron to its orbital, and the remainder of the energy appears as the emitted electron's kinetic energy. The binding energy of an electron is characteristic of both the atom and the orbital it arises from.

Once excited by a photon, a molecule or an atom has many different channels in which it can relax. Relaxation mainly occurs by photon emission or Auger electron emission. A core-excited system will decay to a lower energy state quite rapidly, usually within 10^{-14} seconds due to its instability. X-ray absorption spectroscopy (XAS) and x-ray emission spectroscopy (XES) provide complementary information in that XAS provides information on the unoccupied orbitals of an electronic system and XES provides information on the occupied orbitals. Photon emission occurs when a vacancy in a core electron shell is filled by an electron from one of the outer shells; see Figure 3.

The outer shells include other core orbitals or valence orbitals. The x-ray photon emission process can be shown as the following:



The energy of the emitted photon is the difference between the initial and the final states of the electron and is independent of the excitation energy. The result of this decay process is a cation (A^+) and a photon of light. XES, like XAS, is symmetry, orientational, and polarization selective and can probe the electronic structure of specific atoms in a system. The final state contains only a valence hole, since the core hole was filled by a valence electron, so the x-ray emission spectroscopy relates more directly to chemistry and physics of the ground state species [3-8].

In Auger electron spectroscopy, an electron (e_1) fills a core hole generated by an x-ray and a second electron (e_2) is ejected from the system to compensate for the energy differences in the initial and final states of e_1 ; see Figure 3. Auger decay occurs as follows:



The ejected electron has a characteristic kinetic energy based on the element and the orbital it arises from and is also independent of the excitation energy, so it effectively takes a fingerprint of the sample. Auger electron emission and x-ray photon emission are competitive processes and their rates depend on the atomic number (Z) of the element involved. High Z elements favor x-ray emission decay channels while lower Z elements favor Auger electron emission. The strengths of Auger electron spectroscopy include its sensitivity for low Z elements, its minimal matrix effects, and its high spatial resolution, which is in particular interest for detailed examination of a solid surface [4].

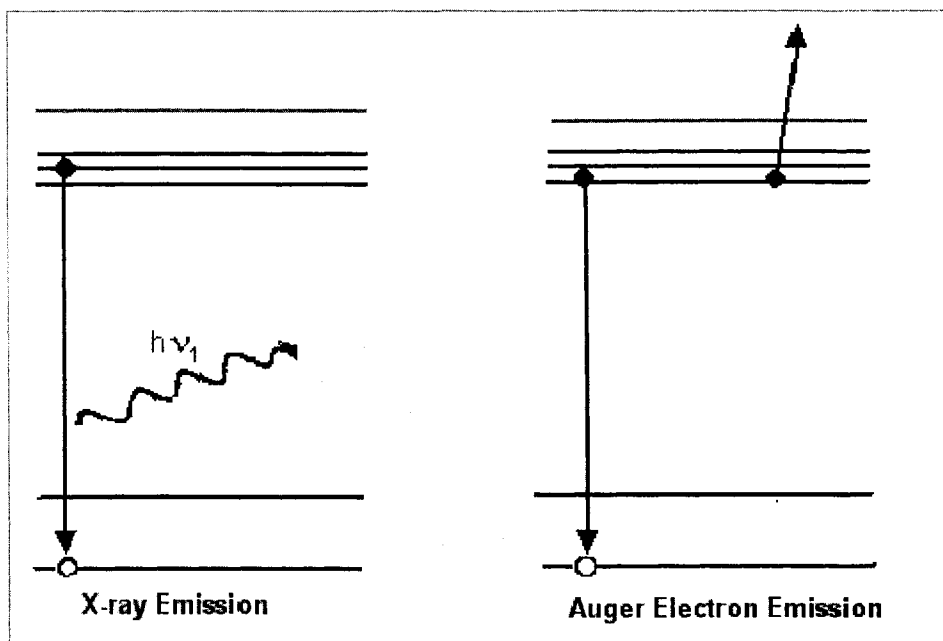
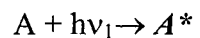


Figure 3. Illustration of the x-ray photon emission process (left) and the Auger electron emission process (right). Gray lines represent unoccupied orbitals.

The final spectroscopic technique discussed in this work is resonant x-ray emission spectroscopy. In this process a photon of light is absorbed by an electron, promoting it to an unoccupied atomic or molecular orbital; see Figure 4. Another electron, an electron from a valence orbital, fills the core hole and the resulting atom or molecule has a valence hole, as follows:



In this equation, A is the neutral atom or molecule, A^* is the system with a core hole excitation and A' is the system with a valence hole excitation. The lifetimes of valence holes are long lived compared to core holes, 10^{-10} s for the valence hole compared to 10^{-14} s for the core hole. This spectroscopic technique yields information on both the

unoccupied and the occupied orbitals of an electronic system, since absorption and emission are both measured. Absorption is usually done in the NEXAFS region by selecting a core electron on a specific atom, or picking a specific resonance; and the emission is measured from a valence orbital filling the core hole.

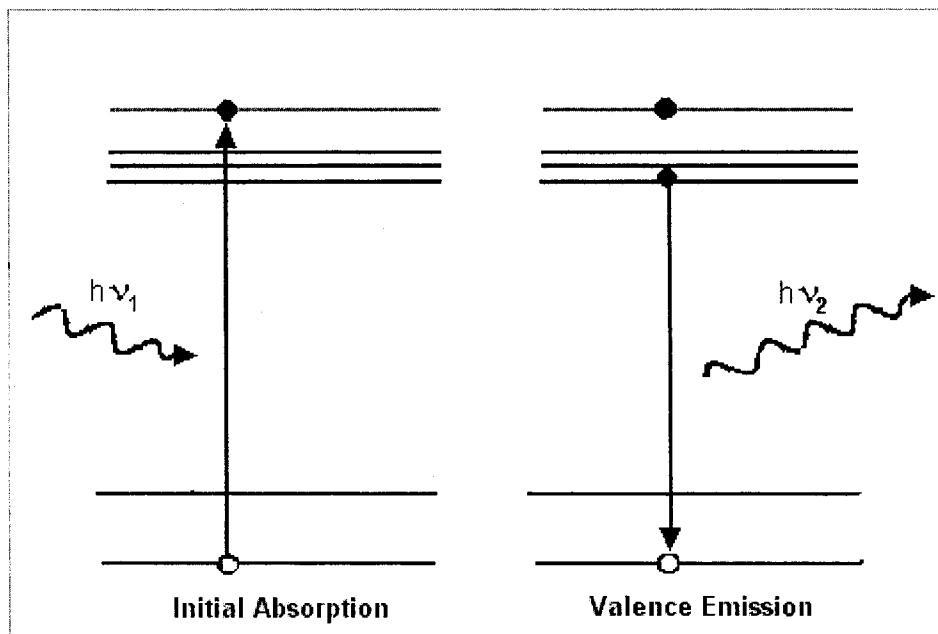


Figure 4. Illustration of the resonant x-ray emission process. In the initial absorption, electron is promoted to an unoccupied orbital (gray line), and the black horizontal lines represent occupied orbitals.

The organization of matter has been theorized and studied for over 100 years. It has long been a goal of scientists to further explain how the protons, electrons, and the neutrons behave in different atomic or molecular environments. With the development of quantum mechanics, calculations could be done to estimate the energies of electronic states, electron spectroscopy, and molecular bonding. Quantum mechanics could then be

used in conjunction with experimental techniques, such as x-ray emission spectroscopy and x-ray absorption, to further explain the organization and behavior of matter and the nature of bonding.

CHAPTER 2

THEORY

Time-Perturbation Theory

When an atom or molecule interacts with electromagnetic radiation, like an x-ray, stimulated absorption occurs when an electron is transmitted from a lower energy state to a higher energy state. To understand the properties of atoms and molecules, one must examine how the system responds to newly imposed perturbations and how it settles into a stationary state after an interval. To do this, time-perturbation theory is applied to a two-level system (one with an initial state and a final state).

Applying the time-dependent perturbation theory to the Hamiltonian yields the following total Hamiltonian:

$$H = H^0 + H'(t) \quad (1)$$

where $H'(t)$ is the time-dependent Hamiltonian and H^0 is the hydrogenic Hamiltonian.

The time-dependent Schrödinger equation is

$$H\Psi = i\hbar \frac{\partial \Psi}{\partial t} \quad (2)$$

The initial state of the system, or the ground state, is denoted as ψ_i with an energy of E_i while the final state is ψ_k with an energy of E_k where the subscripts represent all the quantum numbers of that particular state. These two wavefunctions are the solutions to the Schrödinger equation as follows:

$$H^0\psi_n = E_n\psi_n \quad (3)$$

The wavefunctions are related to the time-dependent unperturbed wavefunctions by the following:

$$\Psi_n(t) = \psi_n e^{-iE_n t / \hbar} \quad (4)$$

In this equation, n can represent either the initial (i) or the final (k) states. Because the functions ψ_n forms a complete basis set, the true time-dependent state can be written as a linear combination of the ψ_n functions according to $\Psi = \sum_k a_k \psi_k$. In the two state treatment, the system is expressed as a linear combination of the two basis functions, the initial and the final states, as the following:

$$\Psi(t) = a_i(t)\Psi_i(t) + a_k(t)\Psi_k(t) \quad (5)$$

The coefficients a_n are also time-dependent since the composition of the system can change with time. The probability that at any time t the system is in state n is $|a_n(t)|^2$ which means that $a_i^2 + a_k^2 = 1$. Substitution of the linear combination into the Schrödinger equation (1) yield the following:

$$H\Psi = a_1 H^0 \Psi_1 + a_1 H'(t) \Psi_1 + a_2 H^0 \Psi_2 + a_2 H'(t) \Psi_2 \quad (6)$$

$$= i\hbar \frac{\partial}{\partial t} (a_1 \Psi_1 + a_2 \Psi_2) \quad (7)$$

$$= i\hbar a_1 \frac{\partial \Psi_1}{\partial t} + i\hbar \Psi_1 \frac{da_1}{dt} + i\hbar a_2 \frac{\partial \Psi_2}{\partial t} + i\hbar \Psi_2 \frac{da_2}{dt} \quad (8)$$

Each basis function satisfies

$$H^0 \Psi_n = i\hbar \frac{\partial \Psi_n}{\partial t} \quad (9)$$

so equation 8 simplifies to

$$a_i H'(t) \Psi_i + a_k H'(t) \Psi_k = i\hbar \dot{a}_i \Psi_i + i\hbar \dot{a}_k \Psi_k \quad (10)$$

where $\dot{a} = da/dt$. The explicit time-dependent wavefunctions are given by:

$$a_i H'(t) |i\rangle e^{-iE_i t/\hbar} + a_k H'(t) |k\rangle e^{-iE_k t/\hbar} = i\hbar \dot{a}_i |i\rangle e^{-iE_i t/\hbar} + i\hbar \dot{a}_k |k\rangle e^{-iE_k t/\hbar} \quad (11)$$

where $\psi_n = |n\rangle$ is the ket notation. Equation 11 is multiplied through from the left by $\langle i|$ and the orthonormality of the states is used to obtain

$$a_i H'_{ii}(t) e^{-iE_i t/\hbar} + a_k H'_{ik}(t) e^{-iE_k t/\hbar} = i\hbar \dot{a}_i \quad (12)$$

where $H'_{ik}(t) = \langle i|H'(t)|k\rangle$. To simplify equation 12, the following substitution is made:

$\hbar\omega_{ki} = E_k - E_i$ to obtain

$$a_i H'_{ii}(t) + a_k H'_{ik}(t) e^{-i\omega_{ki} t} = i\hbar \dot{a}_i \quad (13)$$

In most cases, the perturbation has no diagonal elements so $H'_{ii}(t) = H'_{kk}(t) = 0$ and equation 13 reduces to

$$a_k H'_{ik}(t) e^{-i\omega_{ki} t} = i\hbar \dot{a}_i \quad (14)$$

which arranges to

$$\dot{a}_i = \frac{1}{i\hbar} a_k H'_{ik}(t) e^{-i\omega_{ki} t} \quad (15)$$

Similarly, to obtain \dot{a}_k equation 11 is multiplied through from the left by $\langle k|$ to obtain

$$\dot{a}_k = \frac{1}{i\hbar} a_i H'_{ik}(t) e^{i\omega_{ki} t} \quad (16)$$

Stimulated Absorption

When an electromagnetic field interacts with matter, it can cause one or more electrons to be promoted to a higher energy state. In most cases, the electric field of the radiation reacts more strongly with the electrons than the magnetic field of the radiation, so the magnetic portion of the radiation is neglected and only the electric field

interactions are considered. This is the electric dipole approximation. The oscillating electric field of the radiation is given by the following:

$$\varepsilon = \varepsilon_0 (e^{i\omega t} + e^{-i\omega t}) \quad (17)$$

where ε is the electric field produced by the radiation, ε_0 is the maximum amplitude, $\omega=2\pi\nu$ is the frequency, and t is time. When considering the sizes involved, the size of the electron orbital is usually smaller than the wavelength of light in question, so ε is said to be constant in space, but not in time; this is the second part to the dipole approximation. The time-dependent Hamiltonian in this case is

$H'(t) = V_e = -e\varepsilon\hat{e}_0 \cdot \vec{r} = -e\varepsilon_0\hat{e}_0 \cdot \vec{r}(e^{i\omega t} + e^{-i\omega t})$ where \hat{e}_0 is a unit polarization vector, \vec{r} is the position vector of the electron, and e is the charge of an electron.

If the condition of $t = 0$ is applied to the perturbation $H'(t)$ to stationary state i with energy E_i then $\Psi_i = \exp(-iE_i t/\hbar)\psi_i$ and the expansion coefficients are then $a_i(0) = 0$ and $a_k(0) = 0$ for $i \neq k$:

$$a_k(0) = \delta_{ki} \quad (18)$$

The term δ_{ki} implies $\langle \psi_k | \psi_i \rangle = 1$ when $k = i$ and is zero when $k \neq i$. It is assumed that the perturbation is small and acts for only a short time. Under these conditions, the change in the expansion coefficients from their initial values at the time the perturbation is applied will be small, thus:

$$\frac{da_k}{dt} \approx -\frac{i}{\hbar} \exp[i(E_k - E_i)t/\hbar] \langle \psi_k | H'(t) | \psi_i \rangle \quad (19)$$

If the perturbation acts from $t = 0$ to $t = t'$, integrating over this range yields the following:

$$a_k(t') \approx \delta_{ik} - \frac{i}{\hbar} \int_0^{t'} \exp[i(E_k - E_i)t/\hbar] \langle \psi_k | H'(t) | \psi_i \rangle dt \quad (20)$$

The probability that at any time the system is in the state n is given by $|a_n(t)|^2$. In the dipole approximation

$$H'(t) = -\varepsilon_0 (e^{i\omega t} + e^{-i\omega t}) \int \psi_k^*(r) \hat{e}_0 \cdot D\psi_i(r) dr \quad (21)$$

where

$$\int \psi_k^*(r) \hat{e}_0 \cdot D\psi_i(r) dr = D_{ki} = \langle k | \hat{e}_0 \cdot \mathbf{r} | i \rangle \quad (22)$$

which is the dipole matrix element between states k and i .

At time $t = 0$, the system is in state $|i\rangle$ and from above, $a_i = 1$ then

$$a_k(t) = \frac{i}{\hbar} \varepsilon_0 D_{ki} \int_0^t \left\{ \frac{\exp(i(\omega_{ki} + \omega)t) - 1}{\omega_{ki} + \omega} + \frac{\exp(i(\omega_{ki} - \omega)t) - 1}{\omega_{ki} - \omega} \right\} dt \quad (23)$$

$$= \frac{1}{\hbar} \varepsilon_0 D_{ki} \left[\frac{\exp(i(\omega_{ki} + \omega)t) - 1}{\omega_{ki} + \omega} + \frac{\exp(i(\omega_{ki} - \omega)t) - 1}{\omega_{ki} - \omega} \right] \quad (24)$$

In these equations, $\omega_{ki} = (E_k - E_i)/\hbar$. For $\omega_{ki} = \omega$ gives $E_k - E_i = \hbar\omega$. Exposure of the system to radiation of the frequency ν has produced a transition from state i to state k and since ν is positive, $E_k > E_i$. In this system, there is energy uptake, or absorption, and only the 2nd term in the above equation makes a significant contribution. So for absorption,

$$a_k(t) = \frac{\varepsilon_0 D_{ki}}{\hbar} \frac{\exp(i(\omega_{ki} - \omega)t) - 1}{\omega_{ki} - \omega} \quad (25)$$

The probability of finding the system in the discrete state $|k\rangle$ after time t if it were initially in state $|i\rangle$ at $t=0$ is

$$P_k(t) = \frac{4|H'_{ki}(t)|^2}{\hbar^2(\omega_{ki} - \omega)^2} \sin^2 \frac{1}{2}(\omega_{ki} - \omega)t \quad (26)$$

The amplitudes oscillate in time, known as Rabi oscillations. The rate of absorption is given by the following:

$$R_{k \leftarrow i}(t) = \frac{|a_k(t)|^2}{t} = \frac{\pi \epsilon_0^2}{2\hbar^2} |D_{ki}|^2 \quad (27)$$

In reality, the radiation interacting with the electronic system is not monochromatic, but has a frequency spectrum of $\epsilon_0 = \epsilon_0(\omega)$. It is therefore more convenient to think of the radiation in terms of its density function, or

$$\rho(\omega) = \frac{1}{2} \epsilon_0 \epsilon_0(\omega)^2 \quad (28)$$

This is then integrated over all polarizations and spatial directions to yield the following expression for stimulated absorption:

$$R_{k \leftarrow i}(t) = \frac{2\pi}{3\hbar^2} \frac{1}{4\pi\epsilon_0} \rho(\omega_{ki}) |D_{ki}|^2 = B_{ki} \rho(\omega_{ki}) \quad (29)$$

where B_{ki} is the Einstein coefficient for stimulated absorption.

Spontaneous Emission

Generally, resonant x-ray emission is treated as a two step process, first is the absorption process stimulated by the presence of an x-ray, followed by relaxation as a spontaneous emission process. In quantum field theory, the electromagnetic radiation is also described using a quantum mechanical equation and the Hamiltonian of the system includes contributions from the atom and the field. This means the eigenstates obtained from solving this equation are not true energy eigenstates, but differ very slightly from the atomic energies. Perturbation theory is also used here to describe the interaction as the following:

$$H = H_0 + V' \quad (30)$$

Where V' describes the coupling of the atom to the field of quantisation. If we apply the time dependent perturbation theory to this state to obtain a transition rate between an initial state to a final state the following results:

$$A_{ik} = \frac{4\omega_{ik}^3}{3\hbar c^3} \frac{1}{4\pi\epsilon_0} \left| \langle k | V' | i \rangle \right|^2 \quad (31)$$

where A is the coefficient for spontaneous emission. This equation is dependent on the density of the final states of the atom-field system; which is assumed to form a continuum. From this treatment, it is concluded that the decay is exponential and yields a Lorentzian lineshape as the natural lineshape of atomic transitions. It has been seen that at short decay times, the system deviates from the exponential function.

A system is considered that is in state s at time $t = 0$. The energy of the initial state, $\langle s | H | s \rangle$ is finite. Over time, the system changes as the following:

$$i\hbar \frac{\partial}{\partial t} |\psi(t)\rangle = H |\psi(t)\rangle \quad (32)$$

in this equation, $|\psi(0)\rangle = |s\rangle$. Defining $c_s(t) = \langle s | \psi(t) \rangle$ as the surviving amplitude and multiplying by the above equation gives the following:

$$i\hbar a(t) = \langle s | H | \psi \rangle \quad (33)$$

At time $t=0$ with $[a(0)]^2 = 1$ (from the same argument as in stimulated absorption), the following results:

$$i\hbar a(t) = \langle s | H | s \rangle = E_s \quad (34)$$

The energy of the initial state is real and finite so $a(0)$ must be imaginary. The probability of the survival of the initial state is $P_s(t) = a(t) a^*(t)$. Taking the derivative and using $[a(0)]^2 = 1$ yields the following:

$$\frac{dP_s}{dt} = a(0) + a^*(0) = 0 \quad (35)$$

This is zero because $a(0)$ is imaginary. This equation says that the slope of the decay must be zero at $t=0$. This violates the approximation that the decay is exponential. The quantum mechanics say that the decay curve of an excited state is flat at small times. At larger decay times, the decay behaves more closely to an exponential decay with small deviations from this.

Dipole Selection Rules

To evaluate the different dipole integrals, $\langle \phi_n | \epsilon \cdot \vec{r} | \phi_i \rangle$ is evaluated for the spherical harmonics. If an absorption is allowed, the integral above would have to be non-zero. The total wavefunction is separated as follows:

$$\langle \phi_n | \epsilon \cdot \vec{r} | \phi_i \rangle = \langle R_f | R_i \rangle \langle Y_{l_f, m_f} | \epsilon \cdot r | Y_{l_i, m_i} \rangle \quad (36)$$

In this equation, R represents the radial wavefunctions and Y represent the angular part to the wavefunction. In spherical coordinates the quantity $\epsilon \cdot r$ is represented as follows¹:

$$\vec{\epsilon} \cdot \vec{r} = \epsilon_x \sin \theta \cos \phi + \epsilon_y \sin \theta \sin \phi + \epsilon_z \cos \theta \quad (37)$$

This can be represented as a sum of Y_{10} , Y_{11} , and Y_{1-1} terms. These are then substituted into the spherical harmonic integral as follows:

¹ $x=r\sin\theta\cos\phi$, $y=r\sin\theta\sin\phi$, and $z=r\cos\theta$; r is from the origin to (x,y,z) , θ is the angle of r and the positive z axis and ϕ is the angle r projected in the xy plane and the positive x axis.

$$\langle Y_{l_f m_f} | \vec{\epsilon} \cdot \vec{r} | Y_{l_i m_i} \rangle = \left\langle Y_{l_f m_f} \left| \epsilon_z Y_{10} + \frac{-\epsilon_x + i\epsilon_y}{\sqrt{2}} Y_{11} + \frac{\epsilon_x + i\epsilon_y}{\sqrt{2}} Y_{1-1} \right| Y_{l_i m_i} \right\rangle \quad (38)$$

To evaluate the integral with three spherical harmonics, a Clebsch-Gordan series is used to simplify the problem. The total equation then becomes:

$$\begin{aligned} \langle \phi_n | \vec{\epsilon} \cdot \vec{r} | \phi_i \rangle &= \langle R_f | R_i \rangle \langle Y_{l_f m_f} | \vec{\epsilon} \cdot \vec{r} | Y_{l_i m_i} \rangle \\ &= \sqrt{\frac{(2l_i + 1)}{(2l_f + 1)}} \langle l_n 0 | l_i 100 \rangle \langle R_f | R_i \rangle^* \end{aligned} \quad (39)$$

$$\left(\epsilon_z \langle l_f m_f | l_i 1 m_i 0 \rangle + \frac{-\epsilon_x + i\epsilon_y}{\sqrt{2}} \langle l_f m_f | l_i 1 m_i 1 \rangle + \frac{\epsilon_x + i\epsilon_y}{\sqrt{2}} \langle l_f m_f | l_i 1 m_i -1 \rangle \right)$$

The Clebsch-Gordan coefficients², the terms multiplied by the ϵ_z , ϵ_y , and ϵ_x terms above, are chosen so that one of the states, either the initial or the final, has $l=0$, and are the results of the addition of the angular momentum of the photon to the state $(l_i m_i)$, the photon can be thought of as Y_{1m} . The addition of 1 to l gives answers in the range $|l_i - 1| < l_f < l_i + 1$. The change of l between the initial and final states can only be $\Delta l = 0, \pm 1$; for other values, the Clebsch-Gordan coefficients will be zero. Also, Y_{1m} is odd under parity, so the initial state and the final state must have opposite parity, or $l_f \neq l_i$ so $\Delta l = \pm 1$.

The z-components of the angular momentum add like integers, so the three Clebsch-Gordan coefficients allow $\Delta m = 0, \pm 1$. Since there is no operator which can change the spin here, $\Delta s = 0$. These selection rules only apply for the electric dipole approximation.

² The coefficients are defined as $C(l; m | l_A l_B; m_A m_B)$ and can be calculated using simple equations.

CHAPTER 3

REVIEW OF RELATED LITERATURE

Gas Phase Soft X-ray Regime

Research in the field of x-ray emission spectroscopy dramatically increased with the development of third generation synchrotron-radiation facilities. Synchrotron radiation provides intense photons that are tunable and polarized; conditions that are favorable to x-ray emission spectroscopy. In the late 90's, Nordgren et al. ran experiments on diatomic and linear molecules using x-ray emission techniques. Their primary goals were to investigate symmetry breaking, or core-hole localization, upon excitation and vibrational overlapping. In all molecules they examined two techniques were used, resonant x-ray emission spectroscopy was the primary spectroscopic technique because the discrete nature of core-excited states prepares the symmetry for the emission step, or the lifetime of the core-excited state is much shorter than the rotation of the molecule. Nonresonant x-ray emission spectroscopy, or ionization of the core electron, was the second technique used in their studies [6-13].

N₂

Molecular nitrogen makes up almost 80% of the atmosphere, has a closed shell electronic structure, and is one of the most studied molecules. Glans et al [7] studied the role of parity selection and of lifetime-vibrational interference effects in the resonant x-ray emission spectra of N₂. The ground state electronic configuration for N₂ is $(1\sigma_g)^2$

$(1\sigma_u)^2 (2\sigma_g)^2 (2\sigma_u)^2 (1\pi_u)^4 (3\sigma_g)^2 {}^1\Sigma_g^+$. The first two molecular orbitals are made up of nitrogen core electrons, the remaining three are valence orbitals, contain substantial N 2p character and are the most likely to fill the core hole. In non-resonant x-ray emission, or ionization of the core electron, all three bands are seen. When core ionization occurs, the photoelectron can be either gerade or ungerade, since the electron is being ionized, there is no symmetry dependence of the final state; both gerade and ungerade final states are possible; see Table 1.

Table 1. Non-resonant emission bands for N₂ with an excitation energy of 412 eV.

N K emission	Energy	Shape
3 σ_g	394.2 eV	strong and narrow
1 π_u	392.75 eV	strong and broad
2 σ_u	391.1 eV	weak

In the resonant x-ray emission study, a core electron was excited to the lowest unoccupied molecular orbital, the 1 π_g orbital. The emission spectra were collected by tuning the excitation energy to the five lowest vibrational energies of the 1 π_g electronic orbital; yielding only two emission bands in each of the spectra. The high-energy band is due to the participator electron, or the electron originally excited, and the other is due to a 3 σ_g electron filling the core hole; electrons from the ungerade orbitals are forbidden to fill the core hole due to the dipole selection rules. The two emission peaks for nitrogen are narrow at $v=0$ and become gradually broader as the excitation energy is tuned to higher vibrational levels, showing that the emission bands are sensitive to the potential

curves of the states involved and it becomes necessary to account for interference effects. Because the lifetime width of the core-excited state is of the same order of magnitude as the spacing of the vibrational levels, an excitation of several vibrational levels could occur for each photon energy.

O₂

Nordgren et al applied the techniques of resonant x-ray emission spectroscopy to study symmetry breaking upon core-hole excitation in molecular oxygen [8]. To accomplish this, they used the symmetry selection rules to probe whether the intermediate core-excited state has broken symmetry or not. Their main goal was to test if core-orbitals delocalize, or share the core hole, according to the irreducible representations of the point group of the molecule upon excitation.

The electronic configuration of O₂ in the ground state is $(1\sigma_g)^2 (1\sigma_u)^2 (2\sigma_g)^2 (2\sigma_u)^2 (3\sigma_g)^2 (1\pi_u)^4 (1\pi_g)^2 {}^3\Sigma_g^-$. In the first set of measurements, a $1\sigma_u$ core electron was promoted to the $1\pi_g$ partially filled orbital. Due to the selection rules for both spin and spatial symmetries, the final states of the molecule must be of triplet multiplicity and Σ , Π , or Δ symmetries. There are only three possible bands in the XES spectrum; see Table 2. From the dipole selection rules, the $2\sigma_g \rightarrow 1\sigma_u$ transition is forbidden because the angular momentum does not change by one ($\Delta l = 0$). The only peaks present in the emission spectrum arise from the two allowed, valence orbitals and the parity selection rule was not broken.

Table 2. Resonant x-ray emission bands for molecular oxygen taken with incident photon energies of 530.8 eV, 539.2 eV and 441.1 eV.

O K Emission	Energy	O Character
<i>530.8 eV Excitation Energy</i>		
$1\pi_g$	530.8 eV	2p derived
$3\sigma_g$	523.3 eV	2p derived
$2\sigma_g$	503 eV	2s derived
<i>539.2 eV Excitation Energy</i>		
$1\pi_u$	526 eV	2p derived
<i>541.1 eV Excitation Energy</i>		
$1\pi_u$	527 eV	2p derived

In their second set of measurements, Glans et al. used two separate excitation energies; one at 539.2 eV (which is thought to be composed mainly of the $3\sigma_u$ unoccupied orbital or the σ^*) and at 541.1 eV (which consists of a vast number of Rydberg lines). The emission spectra from these two energies are similar; both consisting of one main emission line, the $1\pi_u \rightarrow 1\sigma_g$. From this information, they conclude that the parity selection rule applies for molecular oxygen excited below threshold and that the inversion symmetry of the core-excited states is retained. It was found, however, that the appearance of dipole forbidden emission peaks did not depend on core-hole localization, but on the internuclear separation [20].

CO₂

The appearance of a carbon atom in between two oxygen atoms greatly changes the O K β emission spectrum by introducing an antisymmetric stretch mode [9]. CO₂ has a ground state electronic configuration of $(1\sigma_g)^2 (1\sigma_u)^2 (2\sigma_g)^2 (3\sigma_g)^2 (2\sigma_u)^2 (4\sigma_g)^2 (3\sigma_u)^2 (1\pi_u)^4 (1\pi_g)^4 {}^1\Sigma_g^+$. Core excitation occurs from either the $1\sigma_g$ or the $1\sigma_u$ O1s orbital to the $2\pi_u$ lowest unoccupied molecular orbital. There are four possible valence emission bands, originating from the $1\pi_g$, $1\pi_u$, $3\sigma_u$ and $4\sigma_g$ orbitals. The emission spectra of CO₂ show three bands, one due to the participator electron and two due to spectator electrons; the emission spectra of molecular oxygen only yielded two bands, a participator and a spectator band. If the parity selection rules held, only gerade final states would be seen, but the $1\pi_g^{-1}2\pi_u^1$ has significant intensity in the O K emission spectra. Calculations show that the nonadiabatic symmetric vibronic coupling, due to the antisymmetric vibrational mode, is responsible for the breaking of the parity selection rules as seen above.

Theoretical calculations for CO₂ show that the symmetry breaking is due to pseudo Jahn-Teller-like vibronic coupling³ between near degenerate core excited states. Vibronic interactions between the $1\sigma_g^{-1}2\pi_u^1$ and the $1\sigma_u^{-1}2\pi_u^1$ intermediate states allows a transition otherwise forbidden to occur in CO₂ [9].

The degree of symmetry breaking depends on the vibrational frequency and the duration of the resonant x-ray scattering process, or the correlation time between absorption and emission. If the duration time is much smaller than the vibrational time period, the molecule has no time to execute the antisymmetric vibration that introduces

³ In Jahn-Teller vibronic coupling, the total wavefunction is not a product of the electronic and the vibronic wavefunctions. The electronic character changes as a function of molecular geometry.

the forbidden parity, and there is no vibronic coupling. Tuning away from resonance shortens the duration of the resonant x-ray scattering process, and one is probing transitions with shorter lifetimes. Vibronic coupling becomes less and less effective. As the absorption energy is tuned farther and farther away from resonance, the forbidden band becomes smaller, and the spectrum becomes symmetry purified.

Scattering theory and a few-level model system were used to explain the symmetry purification. The theory shows that the dynamical vibronic coupling effectively vanishes in the limit of large detuning, or at higher energies, and that in this limit, the transitions between the initial ground state and the final states can be regarded as sudden, or the molecule does not have time to vibrate [10].

A final technique was used by the soft x-ray group in characterizing CO₂: angular resolved resonant x-ray emission spectroscopy [11]. This technique is useful in determining the parity and the spatial symmetry of the unoccupied orbital reached in the absorption step. Since the rotation of molecules occurs on a time frame that is much larger than the lifetime of the core-excited molecule, the molecule are assumed to be frozen during the duration of the absorption/emission process. If the valence electron that fills the core hole is from a σ orbital, the photons are mostly emitted perpendicular to the molecular axis with their polarization vectors parallel to the molecular axis. Transmission from π orbitals gives maximum emission intensity parallel to the molecular axis. By examining the emission spectrum at different energies, five below threshold and two above threshold, Gunnelin et al. found that the first band (A) in the absorption spectrum was the excitation to the $2\pi_u$ unoccupied orbital and that the second (B) and third (C) bands were excitations to unoccupied orbitals with gerade parity.

At absorption features B and C, the intensity ratios of the emission bands are quite different when measured at 0 and 90°, the angle of the spectrometer in relation to the incident radiation. There are two emission bands seen, a high energy feature composed of $1\pi_g$ and a low energy feature composed of $3\sigma_u$, $4\sigma_g$, and $1\pi_u$ with the σ contributions on the low energy side of the peak. At both peaks, the intensity is smaller in the 90° orientation of the spectrometer. The greatest anisotropy occurs on the low energy sides of the lowest energy (composed of $3\sigma_u$, $4\sigma_g$, and $1\pi_u \rightarrow 1\sigma_g$) emission band. This side is considered to be mainly due to $3\sigma_u$ contribution. From this, it was concluded that absorption features B and C are mainly due to unoccupied orbitals of σ symmetry. Above threshold, there is no alignment of the core-excited molecules so the emission in this region is isotropic and the intensity ratios are equal. By performing static exchange calculations on their findings, Gunnelin et al. conclude that the first absorption feature is mainly from the $2\pi_u$ orbital. Their calculations show that the first Rydberg resonance, σ_g symmetry, should appear on the high-energy side of the first absorption peak with little intensity. At higher energies, two groups of transitions are found below the ionization threshold. These are mostly due to the excitation to σ_g orbitals, which indicate a considerable valence-Rydberg mixing in the discrete region of the O K x-ray absorption spectrum of CO₂ similar to that found in O₂.

CO

As a final investigation into soft x-ray emission spectroscopy, Skytt et al. chose carbon monoxide to study angular distribution, electron screening, and vibrational interferences [12-13]. In their first study [12], nonresonant spectra were recorded, so that

satellites are suppressed, and were compared to resonant spectra. The resonant spectra were excited to the π^* orbital and to different Rydberg levels. The ground state configuration of CO is $(1\sigma)^2(2\sigma)^2(3\sigma)^2(4\sigma)^2(1\pi)^4(5\sigma)^2 {}^1\Sigma^+$, where the 1σ corresponds to the core 1s electrons on the oxygen atom and the 2σ correspond to the 1s electrons on the carbon atom. The 4σ , 1π , and 5σ correspond to the valence electrons, and the 3σ is one-center forbidden and is not seen in nonresonant spectra. Nonresonant spectra were recorded a few eV above the O and C ionization thresholds to minimize the effects of shake-up⁴ or shake-off⁵ satellites. The nonresonant bands for both carbon and oxygen are seen in Table 3.

Table 3. Satellite-free nonresonant bands for the C-K emission and O-K emission spectra for CO.

<i>295 eV Excitation Energy</i>		
C-K Emission	Energy	C Character
5 σ	282.0 eV	2p centered on C
1 π	278.4 eV	Shared by C and O
4 σ	276 eV	Little C 2p
<i>545 eV Excitation Energy</i>		
O-K Emission	Energy	O Character
5 σ	528.3 eV	Little O 2p
1 π	525.5 eV	Shared by C and O
4 σ	523 eV	Predominantly O 2p

⁴ Shake-up occurs when excitation of a core electron leaves the valence electrons in a non-eigenstate.

⁵ Shake-off occurs when shake-up results in the release of low energy electrons with the Auger electron.

Resonant emission spectra were recorded by exciting a core electron to the π^* molecular orbital. The carbon spectrum was recorded by tuning the excitation energy to the $v = 0$ vibrational level at 287.40 eV. The emission spectrum yields two features; a high energy band at 287 eV due to the participator electron and a broad, double peak feature around 276-280 eV due a spectator transition. Energy shifts occurring in the resonant spectrum are due to a screening effect caused by the core-excited electron. The 5σ emission band is down-shifted by 2.9 eV and the 1π emission band is down-shifted by 0.6 eV. For the oxygen spectrum, the excitation energy was set to 534.2 eV. Energy shifts in the O-K emission spectrum are -2.9 for the $5\sigma \rightarrow 1\sigma$ transition and -0.8 eV for the $1\pi \rightarrow 1\sigma$ transition.

Resonant x-ray spectra were also recorded by exciting the core electron to the $3s\sigma$ and the $3p\pi$ Rydberg resonances. These emission spectra appear more like the resonant spectra in terms of energy positions. Emission spectra were taken at two different angles, 0° and 90° . For transitions where a core hole, after an initial excitation to a σ orbital, is filled by a σ electron, the emission intensity is maximum at $\theta = 90^\circ$ and is minimum at $\theta = 0^\circ$. For transitions involving a π electron, the maximum is at $\theta = 0^\circ$ and the minimum is at $\theta = 90^\circ$. When the initial excitation is to a π orbital, the trend is reversed, and the molecule is aligned with its nuclear axis perpendicular to the linear polarization vector of the incident x-ray beam. When the excitation is tuned to the C $1s \rightarrow 3s\sigma$ Rydberg resonance, the intensity of the 1π band at $\theta = 0^\circ$ is larger than at $\theta = 90^\circ$, as opposed to the $3p\pi$ spectra where the intensity is largest at $\theta = 90^\circ$.

Since core-hole states have such short lifetimes, each energy level becomes broadened. Because of this, there is an overlap between neighboring vibrational levels in

a molecule if the lifetime width is on the same order of magnitude as the vibrational spacing. In this case, excitation may occur to more than one vibrational level [13]. Since all the vibrational levels can decay into the same final state, the excited levels can cause interference effects. The $[C\ 1s]2\pi$ core excited state has an equilibrium bond length slightly longer than that of the ground state, and the vibrational energy is more than twice the natural lifetime width of the core-excited state. The $[O\ 1s]\ 2\pi$ core excited state has a significantly longer bond length, leading to the excitation of multiple vibrational levels. The lifetime width is approximately equal to the vibrational spacing, yielding a broad, structureless band in the O-K emission spectrum.

For the carbon vibrational profile, three bands are clearly seen, $v = 0, 1$, and 2 . At $v = 0$, there is almost no excitation of the other two states. At the $v = 1$ and $v = 2$ levels, however, vibrational interference is greater and all three levels are excited. In the oxygen case, vibrational interferences occur at all excitation energies. To properly describe the band profiles in the oxygen emission spectra it is necessary to include the interference contributions. For carbon, however, the interference effects are important only at higher vibrational levels.

Gas Phase Hard X-ray Regime

Methyl Chloride

Polarization measurements were first conducted in the late 1980's using chlorinated methanes [14]. The endstation contained a Si(111) crystal which utilizes Bragg angles to be energy selective as well as polarization selective; the crystal rejects all radiation out of the plane of the crystal surface. Polarization selection then occurs by

orienting the crystal surface either parallel or perpendicular to the synchrotron radiation propagation direction. Methyl chloride is the target gas used; the initial absorption occurs from the $1a_1$, or the Cl $1s$, orbital to the $8a_1$ molecular orbital; see Appendix I for a C_{3v} character table. There are three possible valence emission bands which can result from this excitation: $3e$, $7a_1$, and $2e$ filling the $1a_1$ core hole. There are only two peaks in the $K\beta$ spectrum because the fluorescence due to $7a_1$ and $2e$ orbitals is unresolved.

Molecular orbital and static exchange calculations were performed on the $8a_1$, $7a_1$, $3e$ and $2e$ molecular orbitals. They showed that the $8a_1$ and the $7a_1$ axes were oriented along the symmetry axis and with character over both the carbon and the chlorine atoms. The $3e$ and the $2e$ orbitals occurred perpendicular to the symmetry axis, the $2e$ orbital containing mostly carbon character and the $3e$ being the chlorine lone pair of electrons. Since the $8a_1$ orbital is oriented along the molecular symmetry axis, the molecules that are excited are those with their symmetry axes oriented mostly in the synchrotron radiation polarization direction. The resulting emission reflects the molecular alignment produced by the absorption step. The $7a_1 \rightarrow 1a_1$ emission band (B) is also polarized along the symmetry axis so it should be stronger than $3e \rightarrow 1a_1$ (C) when viewed in the parallel polarization. When the excitation energy is well above threshold, the emission bands are more isotropic, and the polarization effect on the fluorescence intensity ratio diminishes.

Quantitative interpretation of the data include molecular-orbital and static-exchange calculations of the occupied and virtual states of the molecule. The measured B-to-C ratios are 0.86 and 0.29 for parallel and perpendicular polarizations, respectively. The corresponding calculated values are 0.90 and 0.24, showing good agreement between theoretical and experimental results.

Chlorofluoromethanes

Due to the discovery of polarized x-ray emission spectroscopy (PXES see above) a study of chlorofluoromethanes was conducted [15-16]. Four compounds were used in this investigation; methyl chloride (CH_3Cl), chlorotrifluoromethane (CF_3Cl), trichlorofluoromethane (CFCl_3), and dichlorodifluoromethane (CF_2Cl_2). In all four of the compounds, three spectra were taken, an absorption spectrum, a resonant emission spectrum and a non-resonant emission spectrum. All the non-resonant emission spectra were taken with an incident photon energy of 2880 eV, well above the Cl 1s threshold, and all the resonant spectra were tuned to the Cl 1s \rightarrow LUMO; 2823.4 eV, 2823.5 eV, 2822.8 eV and 2823.0 eV, respectively.

Their findings for methyl chloride agree well with the work done in [14]. By summing the K-V x-ray emission energy and binding energy for a given valence MO, the ionization potential (IP) for the Cl 1s electron can be calculated. The Cl 1s IP was determined to be 2828.7 eV using the resonant x-ray emission spectra. Due to the improved analysis techniques of emission spectra, the B-to-C intensity ratios were recalculated. They were found to be 0.86 for parallel polarization and 0.34 for perpendicular (compared to 0.86 and 0.29 previously).

Using the non-resonant x-ray emission spectra for CF_3Cl , the Cl 1s IP was determined to be 2830.2. The resonant x-ray emission spectrum was taken while tuned to the excitation of a Cl 1s electron to the $11a_1$ molecular orbital at 2823.5 eV. Three peaks can be seen in the corresponding emission spectra; peak A at 2810.1 eV, peak B at 2815.1 eV and peak C at 2817.1 eV. There are five valence orbitals in CF_3Cl with partial 3p character that can fill the core hole. These are $7e$, $10a_1$, $5e$, $9a_1$, and $4e$, see Table 4.

Since CF_3Cl has the same symmetry as CH_3Cl , the excitation and emission transitions are analogous. Since there is a third peak in the CF_3Cl emission spectra, two comparisons are made; an A-to-C and a B-to-C intensity ratio. The A-to-C peak ratio is 0.18 for parallel polarization and 0.05 for perpendicular polarizations. The B-to-C peak ratios are 0.47 and 0.10, respectively.

Table 4. Energies and assignments of Cl K-V x-ray emission peaks of CF_3Cl .

<i>Peak</i>	<i>Energy</i>	<i>Assignment</i>
A	2810.1 eV	4e, $9a_1 \rightarrow 1a_1$
B	2815.1 eV	$10a_1, 5e \rightarrow 1a_1$
C	2817.1 eV	$7e \rightarrow 1a_1$

The absorption and emission spectra of CFCl_3 are more complicated due to the three chlorine atoms. The six chlorine 1s electrons reside in two molecular orbitals; the $1a_1$ and the $1e$ molecular core orbitals. The presence of three chlorine atoms also triples the number of Cl 3p electrons, increasing the number of valence MO's that can interact with the Cl 1s hole. Using the non-resonant emission spectra, the Cl 1s IP was found to be 2829.3 eV. Resonant excitation was tuned to the $1a_1, 1e \rightarrow 11e$ transitions, which are near degenerate at 2822.8 eV. As with CF_3Cl , there are three emission peaks in the CFCl_3 emission spectrum; peaks A, B and C; see Table 5.

Table 5. Energies and assignments of Cl K-V x-ray emission peaks for CFCl_3 .

<i>Peak</i>	<i>Energy</i>	<i>Assignment</i>
A	2811.5 eV	$7e \rightarrow 1a_1, 1e$
B	2814.5 eV	$8e \rightarrow 1a_1, 1e$
C	2816.7 eV	$11a_1, 9e, 10e, 2a_2 \rightarrow 1a_1, 1e$

There is a rather dramatic polarization effect observed in CFCl_3 . Peaks A and B essentially disappear in perpendicular polarization. The $1e \rightarrow 11e$ absorption followed by the $8e \rightarrow 1e$ emission and the $1a_1 \rightarrow 11e$ absorption followed by the $8e \rightarrow 1a_1$ emission are strongly polarized parallel to the synchrotron radiation; the $1e \rightarrow 11e$ and the $8e \rightarrow 1e$ transitions occur along the symmetry axis which is parallel to the SR polarization. The same can be said for emission peak A.

Finally, CF_2Cl_2 has C_{2v} symmetry, all the other molecules studied have C_{3v} symmetry, which results in the addition of more valence MO's; see Appendix I for a C_{2v} character table. There are 10 valence electrons that contribute to three emission peaks; see Table 6. The Cl 1s IP was found to be 2829.6 eV for CF_2Cl_2 .

Table 6. Energies and assignments of Cl K-V x-ray emission peaks of CF_2Cl_2 .

<i>Peak</i>	<i>Energy</i>	<i>Assignment</i>
A	2810.4 eV	$10a_1, 4b_1, 6b_2 \rightarrow 1a_1, 1b_2$
B	2813.1 eV	$11a_1, 2a_2 \rightarrow 1a_1, 1b_2$
C	2816.5 eV	$12a_1, 3a_2, 6b_1, 7b_2, 8b_2 \rightarrow 1a_1, 1b_2$

Using modified neglect of diatomic-overlap (MNDO) calculations, the amount of 3p character in the chlorofluoromethanes was established [17]. In these calculations, the molecular geometry was varied to minimize the orbital energy, while retaining the proper ground-state molecular symmetry. Chlorotrifluoromethane has 32 valence electrons in the following orbitals: $6a_1$, $3e$, $7a_1$, $8a_1$, $9a_1$, $4e$, $5e$, $1a_2$, $6e$, $10a_1$, and $7e$. The first three unoccupied orbitals are $11a_1$, $12a_1$, and $8e$ in order of increasing energy. The results from the MNDO calculation showed that the $7e$ and the $10a_1$ orbitals contained the most chlorine 3p character and the $6e$ and the $1a_2$ orbitals contained the least (these orbitals are largely fluorine 2p). The rest of the remaining valence orbitals contain various amounts of chlorine 3p character. From this information, it is expected that the emission peaks are dominated by the transitions from the $7e$ and the $10a_1$ to the $1a_1$.

Dichlorodifluoromethane has 32 valence electrons in 16 different valence molecular orbitals; which include $7a_1$, $2b_1$, $8a_1$, $6b_2$, $9a_1$, $7b_2$, $10a_1$, $3b_1$, $11a_1$, $2a_2$, $4b_1$, $8b_2$, $12a_1$, $3a_2$, $5b_1$ and $9b_2$. The lowest unoccupied orbitals are the $13a_1$, $10b_2$, $14a_1$, and $6b_1$. Most of the chlorine 3p character resides in five orbitals, the $9b_2$, $3a_2$, $5b_1$, $12a_1$, and $8b_2$. Four other orbitals contain a significant amount of chlorine 3p character as well, the $11a_1$, $7b_2$, $10a_1$ and $8a_1$. These other orbitals also include large amounts of carbon and fluorine character as well.

Trichlorofluoromethane has 32 valence electrons which reside in 11 different valence molecular orbitals. These 11 orbitals are $7a_1$, $8a_1$, $6e$, $9a_1$, $10a_1$, $7e$, $8e$, $11a_1$, $9e$, $10e$, and $2a_2$. The lowest unoccupied molecular orbitals are $12a_1$, $11e$, and $13a_1$. A large portion of the chlorine 3p character lies in six valence MO's. These are $2a_2$, $10e$, $9e$,

11a₁, 8e, and 7e. Other molecular orbitals that contain a fair amount of chlorine 3p character include the 10a₁ and 8a₁ molecular orbitals.

From studying these molecules, it has been seen that the degree and the direction of x-ray polarization is sensitive to the initial excitation energy in the core-level region, and to the symmetry properties of the valence molecular orbitals involved in the x-ray emission process.

H₂S

The molecule H₂S belongs to the symmetry group C_{2v} and has a subthreshold absorption resonance [18]. It is predicted that this is composed of excitations to the 3b₂ and 6a₁ orbitals. The polarization of the K-V emission varied as the incident photon energy was scanned across the absorption resonance. This was due to excitations to the two predicted absorption resonances, which have different symmetries. There are three peaks found in the x-ray emission spectrum of H₂S, 2b₁ → 1a₁ (A), 5a₁ → 1a₁ (B), and 2b₂ → 1a₁ (C). The MO's are derived from S 3p and H 1s atomic orbitals, 5a₁ and 2b₂ are combinations of S 3p_z and 3p_y AO's with H(1) 1s and H(2) 1s orbitals while 2b₁ is a nonbonding orbital (3p_x). Peak C is suppressed, while A and B are enhanced when the spectrometer is aligned to detect perpendicular polarization; meaning the peaks have strong polarizations of opposite sign. Classically, the polarization, P, for an electric dipole absorber and remitter is given by $P = (3 \cos^2 \gamma - 1) / (\cos^2 \gamma + 3)$ where γ is the average angle between the emission and absorption oscillators, and P reaches limiting values of 1/2 and -1/3 for angles 0° and 90°, respectively. Using the C_{2v} group character table, the 1a₁ → 3b₂ and 1a₁ → 6a₁ absorption dipole moments point along the y and z

axes, respectively. The emission dipole moments for peaks A ($2b_1 \rightarrow 1a_1$), B ($5a_1 \rightarrow 1a_1$) and C ($2b_2 \rightarrow 1a_1$) point along the x, z, and y axes, respectively. The classical model then predicts the polarizations of peaks A, B, and C to be $P_A = -1/3$, $P_B = -1/3$, and $P_C = 1/2$ for the $1a_1 \rightarrow 3b_2$ transition, while $P_A = -1/3$, $P_B = 1/2$, and $P_C = -1/3$ for the $1a_1 \rightarrow 6a_1$ excitation. At excitation energies at or below the peak of the absorption resonance, data is consistent with the $1a_1 \rightarrow 3b_2$ assignment. As the excitation energy is increased to the high-energy side of the absorption maximum, the emission peak polarizations shift towards the polarization values that are consistent with the addition of the $1a_1 \rightarrow 6a_1$ excitation; P_A remains large and negative, P_B becomes less negative and P_C becomes less positive.

Liquids (H₂O)

Emission studies have recently been extended to study the structure of liquids. In 2002, Guo et al. [19] used x-ray emission spectroscopy to study the hydrogen-bonding effect on the electronic structure in liquid water. The application of x-ray techniques in studying liquids has been hampered because of the incompatibility of wet samples and high vacuum conditions needed to use x-rays. The water molecule has C_{2v} symmetry with electronic configuration $1a_1^2 2a_1^2 1b_2^2 3a_1^2 1b_1^2$. There are three transitions that dominate the emission spectrum, the $1b_2$, $3a_1$, $1b_1 \rightarrow 1a_1$. Two orbitals, $1b_2$ and $3a_1$, are derived from a combination of O 2p orbitals and H 1s orbitals and are parallel to the nuclei. The third orbital, $1b_1$, is the lone-pair of O 2p electrons and is perpendicular to the nuclei. The nonresonant excited x-ray emission spectrum of liquid water is similar to that of gas phase water except there is less intensity in the peak that corresponds to the $3a_1 \rightarrow 1a_1$ transition; experimental evidence that the $3a_1$ orbitals are shared when condensation occurs. Calculations show that the major influence of the hydrogen

bonding on the electronic structure is due to the first coordination shell; the energy levels are split as the three valence orbitals interact with surrounding orbitals. Calculations also show that the larger the number of hydrogen bonds formed by a single H₂O molecule (up to four), the greater the sharing of 3a₁ orbital is, which decreases the intensity, agreeing well with experimental data.

Nondipole X-Ray Emission

Strong nondipole features were observed in Cl₂ molecules when measured near the chlorine K edge [20]. In polyatomic molecules, vibrational coupling can lift the degeneracy of equivalent core-excited electronic states. In diatomic molecules, however, vibronic core-excited states remain degenerate. The pre-edge absorption feature of Cl₂ taken near the K edge comprised of two degenerate transitions: a dipole allowed transition $1\sigma_g \rightarrow 5\sigma_u$, and a dipole forbidden $1\sigma_u \rightarrow 5\sigma_u$ transition. It was discovered that the absorption feature had two contributions because there were two emission peaks, one corresponding to the dipole allowed $2\pi_u \rightarrow 1\sigma_g$ transition and a dipole forbidden $2\pi_g \rightarrow 1\sigma_u$ transition. The dipole approximation is normally applied in x-ray processes because the incident wavelength is much larger than the radius of the core orbital. This is not valid in molecular chlorine, however, because the internuclear separation is not negligible relative to the wavelength when considering the delocalized $1\sigma_g$ and $1\sigma_u$ orbitals. Phase variation of the incident radiation over the entire molecule must be considered, or the dipole approximation is not valid here. Theoretical calculations show that there is an equilibrium bond length dependence in the normalization factor for the transition $\langle 1s | \hat{\mu}_z | 5\sigma_u \rangle$, where $1s$ is the atomic-hydrogen like $1\sigma_g$ and $1\sigma_u$ orbital, $\hat{\mu}_z$ is the dipole-

moment operator along the molecular axis, and $5\sigma_u$ is a linear combination of atomic orbitals. Calculations show that as the internuclear separation increases, the nondipole effects also increase until the allowed and the forbidden transitions are equal.

CHAPTER 4

EXPERIMENTAL SET-UP

Advanced Light Source (ALS)

Experiments were conducted at beamline 9.3.1 at the ALS, Lawrence Berkeley Laboratory, Berkeley, CA. Beamline 9.3.1 has an energy range of 2.2 keV to 6.0 keV and is over 99% linearly polarized along the plane of the storage ring orbit. The energy selection is accomplished through two Si(1,1,1) crystals which utilize Bragg diffraction, below, to provide intense (10^{11} photons/sec) monochromatic light, see Figure 5.

$$n\lambda = 2d \sin \theta_{\text{Bragg}} \quad (\text{Bragg Equation})$$

In this equation θ_{Bragg} is the Bragg angle, d is the lattice spacing, and λ is the wavelength of light (in Angstroms). For Si(1,1,1), the $2d$ in Angstroms is 6.2712.

X-ray Emission Spectrometer (XES)

The x-ray emission spectrometer consists of three main parts, the sample, or main, chamber, the spectrometer, and the detector. The detector and the spectrometer are situated on a Rowland circle and the sample is situated in the interior of the circle. The main chamber is cylindrical with a radius of 6.1 inches and a length of 7.2 inches. Separating the main chamber from the spectrometer is a rotatable arm 13.4 inches long. The spectrometer is a Si(1,1,1) crystal, which is 40 mm x 20 mm x 0.3 mm housed in a 4-way cross 6.2 inches long and 6.2 inches wide. A movable arm 25.3 inches long

separates the spectrometer from the detector, and is responsible for selecting the radius of the Rowland circle. To record the x-ray emission spectrum, three micro-channel plates and a square position sensitive resistive anode are used. The micro-channel plates have a radius of 40.0 mm and the entire detector sits 2.10 inches high including the mount, see Figure 5 for the x-ray emission spectrometer flow diagram.

Attached to the front of the main chamber are three devices, a 4-jaw, an alignment plate, and a gate valve. The 4-jaw consist of four 1.3 x 1.2 x 0.1 inch coplanar aluminum plates 90° apart. They are painted with phosphor, which fluoresces upon contact with x-ray radiation, and are designed to cut off any stray light emerging from the monochromator. The alignment plate enters the beam pipe at a 45° angle. It is 2.50 x 1.0 x 0.1 inches with a rounded top and a 1 mm hole drilled 1.53 inches and at 45° from the square end. This device is used to align the front of the main chamber with the beamline. Last, the beamline isolation valve is used to vacuum isolate the main chamber from the beamline.

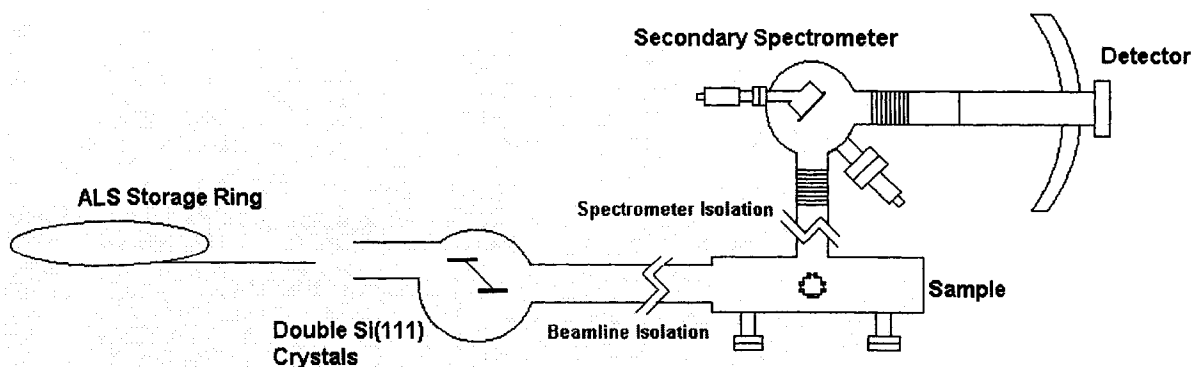


Figure 5. Flow diagram of beamline 9.3.1 and the x-ray emission spectrometer.

Inside the main chamber there is an ionization gauge, convection gauge, a back alignment plate, a sample manipulator and a Si diode. The convection gauge and the ionization gauge are used to read the pressure inside the chamber in the range of 10^3 to 10^{-4} torr for the convection and 10^{-3} to 10^{-10} for the ionization gauge. The back alignment plate is 3.75 x 2.12 x 0.1 inches and curved with a 6 inch radius. It has a 1 mm alignment hole in the center of the plate used to align the back of the chamber. A sample manipulator is attached to the top of the main chamber. It is responsible for moving the sample in and out of the path of the beam, to rotate the sample from 0 to 360°, and for up and down and in and out movement of the sample with relation to the incoming photons. There is a four-inch movement of the sample manipulator feedthrough, and the feedthrough has a diameter of 0.25 inches. This feedthrough is where a sample holder is attached. The Si diode enters the chamber at a 45° angle, pointed at the sample manipulator; it is used to take total fluorescence measurements.

Between the main chamber and the spectrometer there is a spectrometer isolation gate valve, a rotary seal, and a bellow. The gate valve is used to isolate the spectrometer from the main chamber, thus protecting the detector if a leak should occur. The rotary seal allows the spectrometer and detector to rotate from -5 to 180° independent of the main chamber to make polarization measurements. The bellow allows the spectrometer tank to be slightly rocked to optimize the Bragg angle.

In and attached to the spectrometer tank are the following: a crystal bending device, an ionization gauge, and a convection gauge, previously discussed. The crystal bending device was designed to bend a crystal into a near perfect circular arc, which provides focusing and energy tuning of the x-rays. Radii of 0.6m to 0.8m are produced

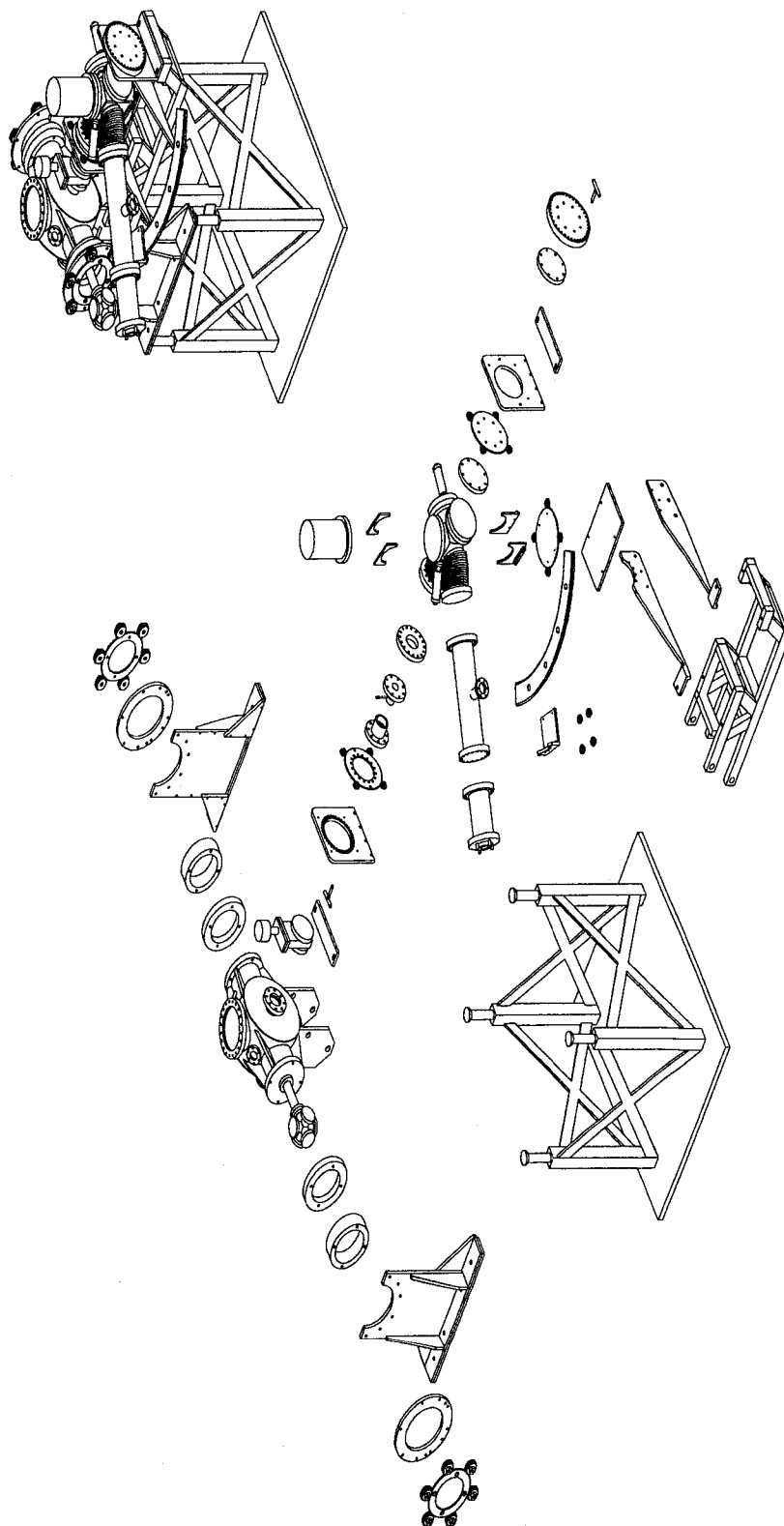


Figure 6. Blow-up drawing of the x-ray emission spectrometer.

by the bending device, and its vertical axis is located on the vertical axis of the main chamber. Bending action occurs by a rotary linkage controlled by a micrometer.

The detector is an electron-optical device which converts an incoming charged particle, neutral particle, or energetic photon to four charge signals proportional to the spatial position of incidence. This device consists of a resistive anode position encoder, three wafer-type microchannel-plate electron multipliers (MCPs), and integral biased and signal decoupling circuits. This is mounted in an alumina-ceramic and gold-plated stainless-steel holder assembly operated in clean vacuum with pressures lower than 10^{-6} torr. The microchannel plates are supported above the resistive anode encoder (RAE) by gold-plated stainless steel rings, and held in place by spring loaded 3-point contacts. All bias and signal connections are made to pins on the underside of the ceramic baseplate. Signal leads are capacitively de-coupled, so the detector is biased with respect to ground.

Incident photons strike the front surface of the first MCP, which is coated with CsI a coating that is most effective for photon detection, resulting in secondary electron production from the wall of one or more microchannels. Because of the applied electric field, an electron avalanche occurs. This resulting charge cloud travels in a uniform electric field and strikes the RAE. This charge packet then diffuses in the uniform resistive sheet surface of the RAE toward collection electrodes located at the four corners of the anode (A, B, C, and D). The relative charge reaching each of the four corners contacts is a linear function of the position along X and Y orthogonal axes of the RAE.

Vacuum in the main chamber is achieved by using a Turbovac 151 turbo pump operating at 833 Hz. A Turbovac 50 operating at 1200 Hz provides vacuum for the spectrometer and the detector. Both pumps are backed by a mechanical pump and

monitored with thermocouple pressure gauges. Vacuum in both sections of the x-ray emission spectrometer (XES) reaches pressures of 10^{-7} torr. To control the vacuum in the XES, seven different valves are used. The beamline isolation valve and the spectrometer isolation valve were previously discussed. There are two foreline valves between the mechanical pump and each of the turbo pumps, two vent valves attached to each of the turbo pumps, and a gas manifold which allows gas to enter the gas cell and also allows gas to be pumped out of the gas cell. All controls to the valves are routed to the interlock boxes inside the electronics rack (discussed at a later time). All pressure sensing devices, thermocouples, convectrons and a baratron (a pressure sensor for the gas cell), are routed to a pressure sensor box on the XES frame and then to an interface box on the electronics rack (discussed at a later time). Ionization gauges are routed to the interlock boxes.

Since the XES can rotate in three different ways, position sensitive devices were installed. To track the position of the detector on the curved way (this movement selects the radius of the Rowland circle), a cable-extension position transducer is used. This device measures the displacement of the detector from 90° (θ_{Curved}) and gives a voltage output. To calculate θ_{Curved} , the Bragg angle is used:

$$\theta_{Curved} = 2 \cdot (45^\circ - \theta_{Bragg})$$

The displacement from 90° directly correlates to the energy region the detector can view. To find the voltage output of the position transducer, the following equation is used:

$$V_{Out} = -0.136\theta_{Curved} + 3.4304.$$

The voltage range for the curved way is $7.372 \geq V_{Out} \geq 0.206$ which corresponds to a displacement of 29.8° to the right of 90° and 24° to the left of 90° . The position of the spectrometer tank and the angle of the spectrometer are measured using rotational position transducers, which provides a linear output voltage with respect to the angle. The spectrometer angle can be calculated using the following equation:

$$V_{Out} = -0.0278\theta_{Spect} + 8.5883$$

and corresponds to a voltage output range of $8.705 \geq V_{Out} \geq 3.554$. The tank angle is not calculated directly; instead it is measured versus the photon energy, since the voltage output range is less than two volts. The equation is as follows:

$$V_{Out} = 3 \cdot 10^{-7} (h\nu)^2 - 0.0021(h\nu) + 8.7956$$

The angle of the main chamber is measured using two biaxial clinometers (tilt sensors). These two devices work together to cover the full range of rotation. Tilt one measures angles below zero up to an angle of 42° and tilt two covers angles above 42° . The tilt of the chamber can be calculated using the following set of equations:

$$\text{when } \theta_{Chamb} \leq 42^\circ; V = -1.0 \cdot 10^{-5} \theta^3 + 0.0003\theta^2 - 0.0376\theta - 0.0025$$

$$\text{when } \theta_{Chamb} \geq 42^\circ; V = 5.0 \cdot 10^{-6} \theta^3 + -0.0013\theta^2 + 0.1422\theta - 5.854$$

The voltage range for the tilt sensors is tilt one, $-4.193 < V_{tilt} < (4.0)$, and for tilt two, $-4.22 < V_{tilt} < (4.0)$. All angular data from the tilt sensors, the spectrometer position, the detector position, and the tank are routed to the position sensor box mounted to the frame

of the chamber. One cable is then plugged into the interface box on the electronics rack (discussed at a later time).

Electronics

All electrical components from the XES are routed to the electronics rack, see Figure 7. The rack is composed of eighteen different components; two power strips, two ionization gauge controllers, an oscilloscope, the interface box, two blue boxes, two thermocouple controllers, two turbo controllers, a baratron controller, a convectron controller, the detector electronics box, a power supply, a digital signal box and an analog signal box. The position sensor data is run to the interface box where it is routed to a digital output on the front of the box. The knobs on the front of the box allow one to select a specific parameter to view. Vacuum sensor data is also routed to the interface box. From here, the components are separated and sent to the individual controllers. All data entering the interface box is sent to the computer via the analog signal box and recorded.

Signal from the detector is routed to the electronics rack through a bundle of six cables. These cables run from the pre-amp attached to the detector arm of the XES to the detector electronics box. They are labeled A, B, C, D, E and power; they plug into their respective slots at the back of the electronics box; A, B, C, and D where previously discussed, E measures the counts/second striking the anode and the power cord supplies a voltage to the pre-amp. The signal is then routed to the computer through the digital signal box. The image on the detector is also sent to the oscilloscope through the detector electronics box so that a real time image can be viewed. There is also a high voltage cord which runs from the voltage supply to the voltage divider box on the detector arm. The

input voltage is 2500V and the three output voltages are, Z_{in} , Z_{out} , and RAE; 0 V, -2400 V and -2500V respectively. This is set up so that there is a -800 V drop across each plate and the anode is 5 V more negative.

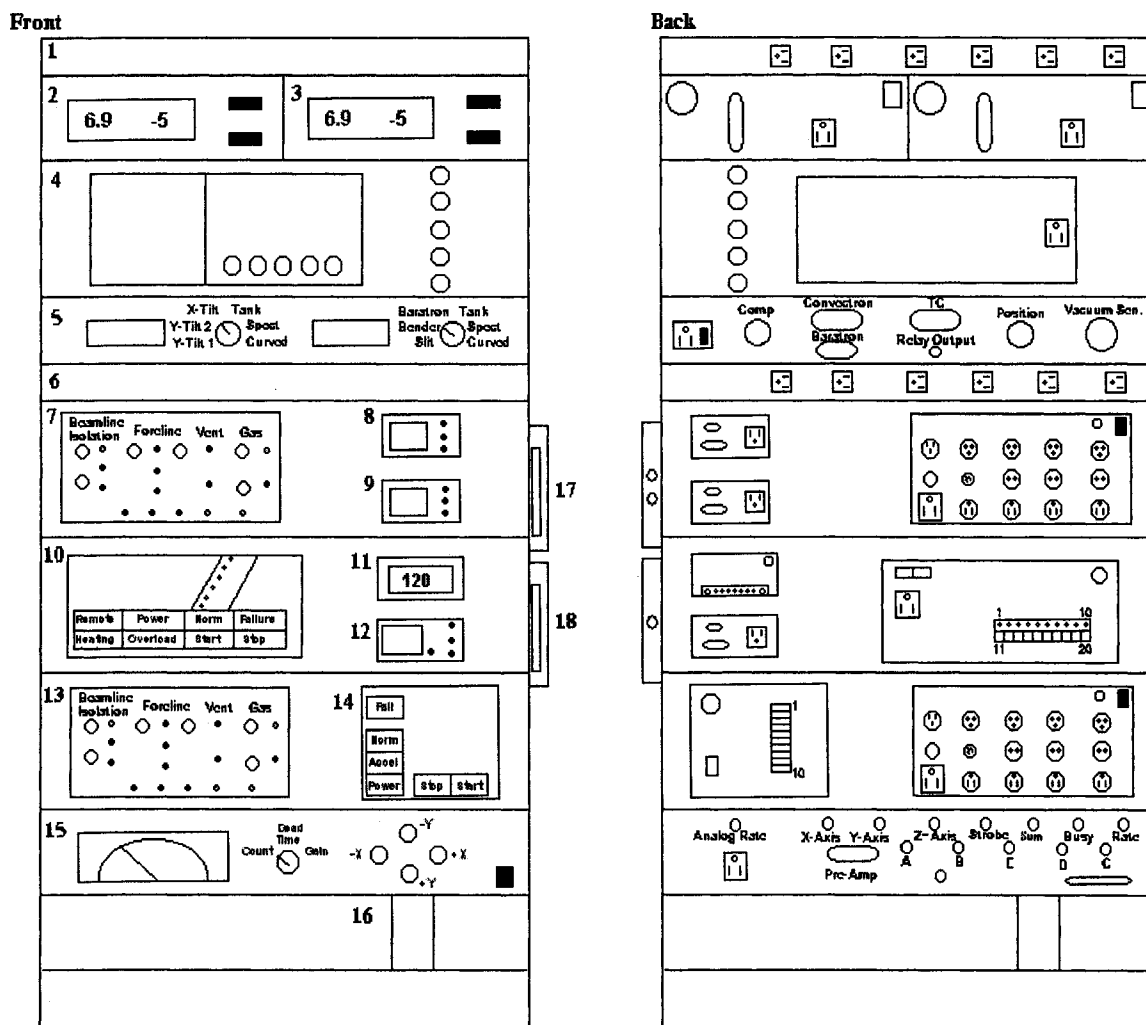


Figure 7. Front and back views of the electronics rack. Key: 1 & 6: power strips, 2 & 3: ionization gauge controllers, 4: oscilloscope, 5: interface box, 7 & 13: interlock boxes, 8 & 9: Thermocouple controllers, 10 & 14: turbo pump controllers, 11: baratron controller, 12: convectron controller, 15: detector electronics box, 16: power supply, 17: digital signal box, and 18: analog signal box

The gate valve switches are also run through a series of boxes before reaching the interlock boxes. One cable runs from the XES to the rack where it is then separated into its components and routed to one of the two interlock boxes. The beamline isolation valve runs to the “beamline gate valve” output at the back of the chamber (1) blue box, the foreline chamber valve runs to the “foreline valve”, the chamber vent valve runs to the “vent valve” and the gas manifold runs to the “gas inlet valve”. The beamline isolation valve, the foreline valve, and the gas inlet valve can all be opened and closed from the front of the interlock box. The same set-up is valid for the spectrometer (2) interlock box as well, except the gas inlet switch controls the power supply. Both of the two interlock boxes have inputs for the turbo pumps, the ionization gauge, or convectron gauge, upstream interlock, and downstream interlock. When all conditions are met, i.e. the pressure is low (10^{-5} torr), the turbo is up to speed, and the same conditions are met for upstream (another interlock box), the valves can be opened and photons can enter the XES. When conditions are not met, i.e. the turbo stops, there is a leak, or the upstream conditions are not met, the interlock box shuts off, closes all valves, turns the power to the detector off, and begins to vent the XES after a delay period, see Figure 8 for further discussion.

Sample Holders

There are two sample holders designed in conjunction with the XES; a solid sample holder and a gas sample holder. The solid sample holder measures 1.200 x 4.300 x 0.250 inches, has a removable sample plate which is 1.00 x 2.25 x 0.10 inches in volume. Three different samples can be mounted at once; each contained in a circular

aluminum frame that is bolted to the sample plate. The sample holder is electrically isolated from the manipulator by a series of Al_2O_3 cylindrical ceramics; thus allowing a current to be measured from the sample plate. To allow for rotation, the part was designed to have the face of the sample, or a crystal, on the manipulator's axis of rotation.

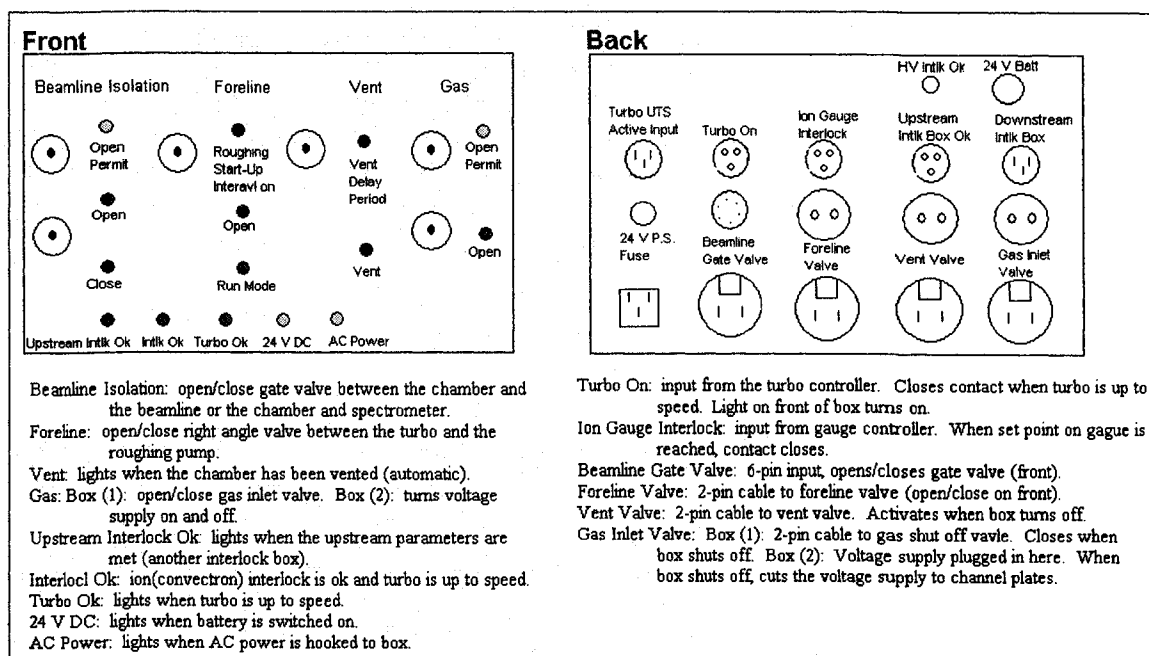


Figure 8. Description of the interlock box and its various functions.

To run a gas sample, a containment device was designed to allow x-rays to enter and exit, but keep the gas inside. Silicon nitride (Si_3N_4) windows were first selected because there is over 90% transmittance of x-rays in the energy range of 2400-3500 eV, the energy range of the spectrometer. The entrance and exit windows are 1.0 mm x 1.0 mm x 200 nm on a 5.0 mm x 5.0 mm x 200µm frame; while the viewing window (the window that transmits x-rays that will be measured by the detector) measures 6.0 mm x

2.0 mm x 200 nm and sits on a 10.0 mm x 5.0 mm x 200 μ m frame. The windows are all glued to 0.10 inch thick aluminum plates, so when a window breaks, another window/plate can replace it with ease.

The skeleton of the gas cell is a 1.360 inch cube, which allows for attachments on each of the six faces. Attached to the front face of the cube is the entrance window mount, a cylindrical piece that extends 0.3775 inches into the cube with a 0.1575 inch diameter hole drilled into the center to allow x-rays to pass through and four O-80 drilled and tapped holes to allow the aluminum window plates to be attached. Bolted to the back face of the cube is the exit window mount; similar design as above except a diode and a diode mount are attached to the back-side of the window to allow for transmission measurements; see Figure 9 and Appendix II.

X-rays emitted from the gas sample exit the cube through the view window mount on the right side of the cube. This mount extends 0.280 inches into the cube and has a rectangular 0.30 x 0.085 inch hole drilled in the center to allow the x-rays to exit. As with the entrance and exit window mounts, the Al view window plate with a glued window attach to the mount. Through a flange on the left side of the cube, gas enters the cell. A custom piece was welded to a mini conflat flange to allow gas to be pumped into the cell or evacuated from the cell. This piece has a 0.25 inch tube with a VCR fitting on the end; see Figure 9 and Appendix II.

To support the gas cell on the 0.250 inch sample manipulator feedthrough, the top piece of the gas cell has a 0.50 diameter x 1.00 inch length cylindrical extrusion with a 0.25 inch hole drilled 0.75 inches deep. To tighten the feedthrough in, two 4-40 screws 90 ° apart are used. There is also a 1mm alignment hole drilled through the gas cell

support, see Figure 9. To test the focus of the entering x-rays, a YAP crystal and a 90° prism are attached to holding plates and mounted to the bottom of the gas cell which can be viewed through the sample loading window; see Figure 9 and Appendix II.

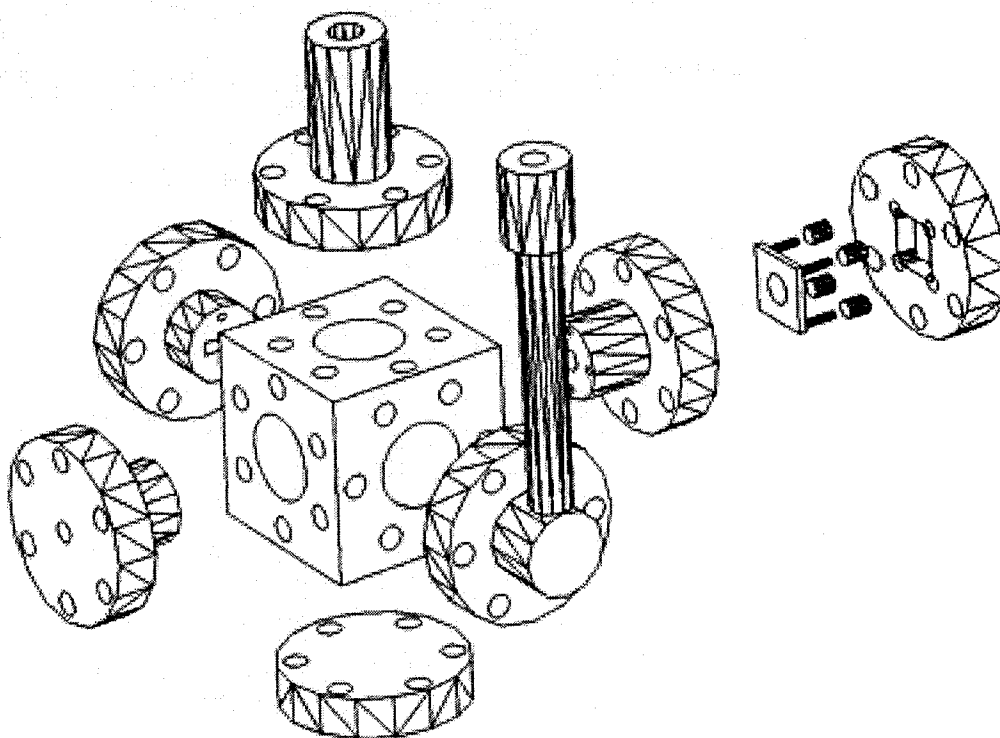


Figure 9. The cube and various attachments for the gas cell.

Alignment

Photons travel down three different paths in the XES, axis A, B and C. Axis A is the path the incident photons follow that intersects the main chamber through the center and is parallel to the floor. Axis B is defined by the center point in the main chamber (the spot where the sample is located) and by the crystal. This axis is perpendicular to axis A. The third axis, C, contains the crystal and the detector, and is movable. In order to

collect data, the chamber must sit so that axis A is in line with the beamline, axis B is in fact perpendicular, and that the photons will bounce off the crystal and strike the detector. To accomplish this, all three axes are aligned separately. The front and back alignment plates and a phosphor covered window at the rear of the chamber aid in the alignment of axis A. Axis A is aligned by moving the main chamber left/right and up/down until the photons are traveling through the center of the main chamber. To align axis B, a Si(1,1,1) crystal is mounted on the solid sample holder to bounce light from the center of the main chamber to the sample loading window, and then to the spectrometer. The energy used for this is 2816 eV, so the crystal is at a Bragg angle of 45° . The four corners of the chamber are moved to accomplish this. To align axis C, the spectrometer tank is rocked so that the photons bounce off the crystal and on to a phosphor window at the end of the axis; see Figure 10.

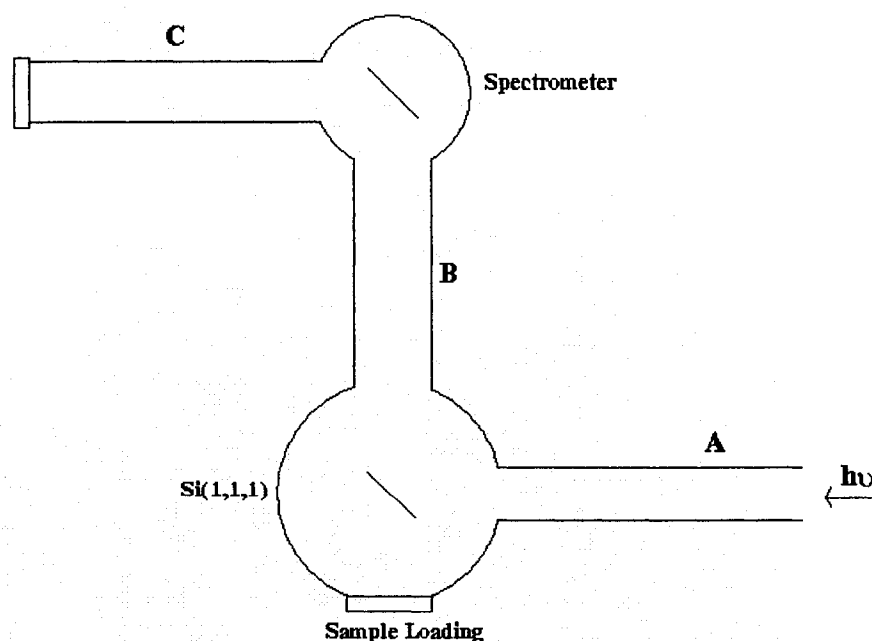


Figure 10. Diagram of the alignment of axes A, B and C.

XES Testing

Before the detector was mounted and data collection began, preliminary testing was done to test the energy range of the XES. Light from the monochromator was passed straight down axis B through the sample loading window and on to a phosphor window. The energy of the photons was changed and the detector arm was moved according to the calculated Bragg angle. The energy range tested was 2400 to 3500 eV, and all parameters were recorded, see Table 9.

Table 9. Preliminary testing of the emission spectrometer's energy range.

Energy, eV	Tank, V	Curved, V	Spect, V	Bragg Angle	Curved Angle
2400	5.327	6.576	6.02	55.46	-20.9
2464	5.269	5.97	6.018	53.75	-17.5
2600	5.154	4.939	6.015	49.5	-9
2816	4.997	3.515	6.024	44.6	0
2900	4.971	2.962	6.014	42.98	4.02
3050	4.911	2.208	6.018	40.41	9.2
3190	4.848	1.603	6.018	38.29	13.42
3350	4.793	1.007	6.018	36.17	17.66
3500	4.737	0.552	6.016	34.4	21.2

Software

A signal originating from the anode travels to the detector electronics box where it is converted from a set of four voltages (A, B, C, and D) to x and y coordinates. The x and y coordinates are sent to the computer where a customized version of Labview has been designed to sum the x and y coordinates over a user designated time frame. The x and y coordinates correspond to channels in the x and y directions, 0 to 1023 channels for both axes. When a background scan is run, data appears on the screen in a circular area

(due to the fact that the channel plates are round). When an x-ray emission strikes the detector, the signal appears as a line crossing the length of the circle approximately 13° off of vertical since the detector was mounted to the XES off center. This line corresponds to the width of the spectrometer crystal, the width of the signal, or the energy separation, corresponds to the length of the crystal.

After data has been collected, Labview, a data acquisition program, saves the image as a 1023 x 1023 matrix. To analyze the image and get a spectrum, a procedure was written in Igor, a graphical and data analysis program. It first converts the 1023 x 1023 matrix into 1023 lines, each line containing 1023 entries. Once converted, Igor then allows the user to manually rotate the image, or to have Igor automatically rotate the image to give the narrowest peak using a Gaussian approximation; see Figure 11. Due to the bend of the crystal, the image is not a straight line, which makes the peaks in the spectrum wider than they would normally be. Igor has a function designed into it that will transform the curved image into a straight line. The user also has the option to select a certain region in the spectrum to view. This makes the background of the image smaller; not selecting the edge of the image rids the spectrum of the edge effect of the MCPs; see Figure 12. From here, the energy scale can be calculated and added to the spectrum using the positions and the known energies of the two peaks.

Data analysis was accomplished using Origin. The energy versus intensity spectra were plotted in Origin and a Gaussian function was fit to the two peaks. The fitting program calculates the total area under each peak and the width of the peaks. The relative intensities of α_1 and α_2 can then be compared for different energies and polarizations.

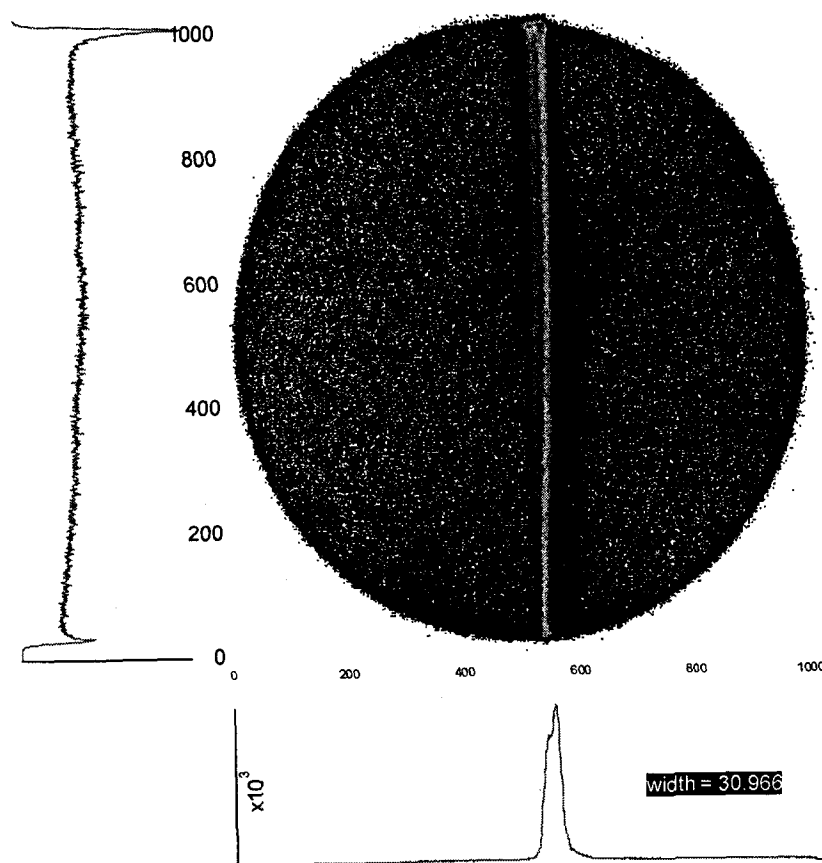


Figure 11. Spectrum rotated by Igor using a Gaussian function. Width of the peak is in channels.

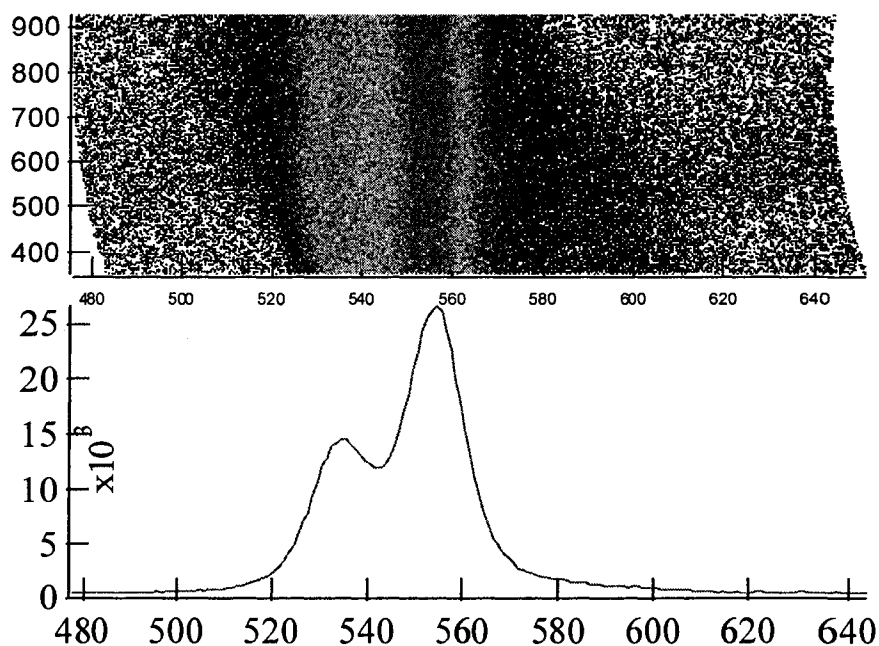


Figure 12. Selection of channels 480 through 640 from Figure 11. This image has also been straightened using Igor.

KCl

Solid KCL was formed into a 0.52 inch diameter pellet and taped onto the solid sample holder using carbon tape. The holder was positioned so that the incident photons would strike the sample in the center when the sample was perpendicular to the beam. The sample was then rotated approximately 30° off perpendicular to give the maximum counts/second on the detector. A total fluorescence scan was run at the Cl K-edge and also at the K K-edge; shown in Chapter 5. The detector arm was positioned to collect the Cl $K\alpha$ spectrum ($K\alpha_1$ is at 2622 eV and $K\alpha_2$ is at 2620 eV with a 2/1 intensity ratio, respectively). Parameters for this energy range are as follows: curved way = 4.728 V, tank = 5.125 V, bender = 2.359 V, spectrometer = 8.538 V for parallel polarizations and

6.050 V for perpendicular polarizations, $x = -0.050$ V, $y_1 = -0.936$ V and $y_2 = 0.044$ V. The $K K\alpha$ spectrum was also measured ($K\alpha_1$ is at 3313 eV and $K\alpha_2$ is at 3311 eV). The parameters for this energy region are as follows: curved way = 1.212 V, tank = 4.797 V, bender = 2.300, spectrometer, x , y_1 , and y_2 are the same as for chlorine. Both energy regions were run with the crystal slit 1mm from the face of the crystal at parallel polarizations and 5 mm from the crystal face at perpendicular polarizations.

Freon-13 (CF_3Cl)

Gas was pumped into the gas cell at pressures of 600 and 500 torr, and at room temperature. An absorption scan was run at the Cl K-edge to find any major resonances; this is located in Chapter 5. As with the solid, emission spectra were collected in the parallel and in the perpendicular orientations at energies above and below threshold. All parameters for this gas were run the same as for chlorine in the KCl sample.

CHAPTER 5

RESULTS AND DISCUSSION

KCl

A total fluorescence scan was run at the chlorine and at the potassium K-edges. Chlorine was scanned from 2815 eV to 2900 eV and based on this scan, seven incident photon energies were chosen, 2826.0 eV, 2830.0 eV, 2832.0 eV, 2836.3 eV, 2845.5 eV, 2853.0 eV and 2875.0 eV. The potassium scan was run from 3600 eV to 3700 eV. There were also seven incident energies chosen for potassium based on this scan at 3612.4 eV, 3616.0 eV, 3618.8 eV, 3621.4 eV, 3621.4 eV, 3645.0 eV, and 3670.0 eV; see Figure 13. Two emission spectra were taken at each of the fourteen incident photon energies, one parallel to the incident photons and one perpendicular to the incident photons.

Chlorine Edge

At 2826 eV, an energy below the ionization threshold, the emission spectrum of chlorine looks slightly different at the two polarizations. In the perpendicular polarization, there is a better separation of α_1 and α_2 compared to the parallel polarization. The heights of α_1 are 31220 and 20784 and α_2 are 17564 and 13858, respectively. This corresponds to a ratio of 1.8/1 in the perpendicular and 1.5/1 in the parallel. When comparing the total area under the two peaks, the perpendicular orientation yields areas of 40038 and 21931 and the parallel yields 26587 and 16643; this

corresponds to the following ratios: 1.8/1 and 1.6/1, respectively. When comparing the widths, α_1 and α_2 have roughly the same width; 1.12 eV in the parallel direction and 1.04 in the perpendicular; see Figure 14.

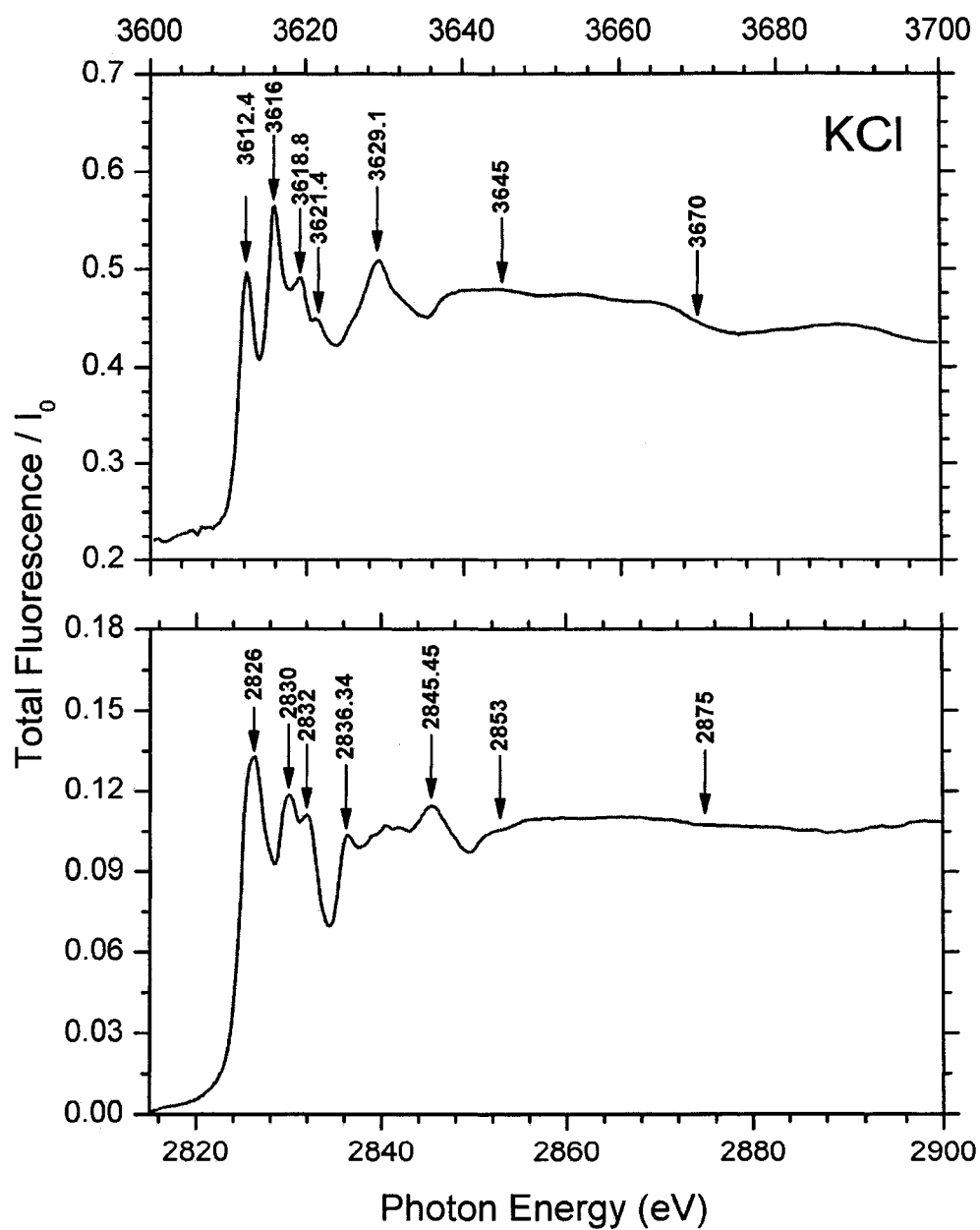


Figure 13. Total fluorescence yields of chlorine and potassium near the K-edge.

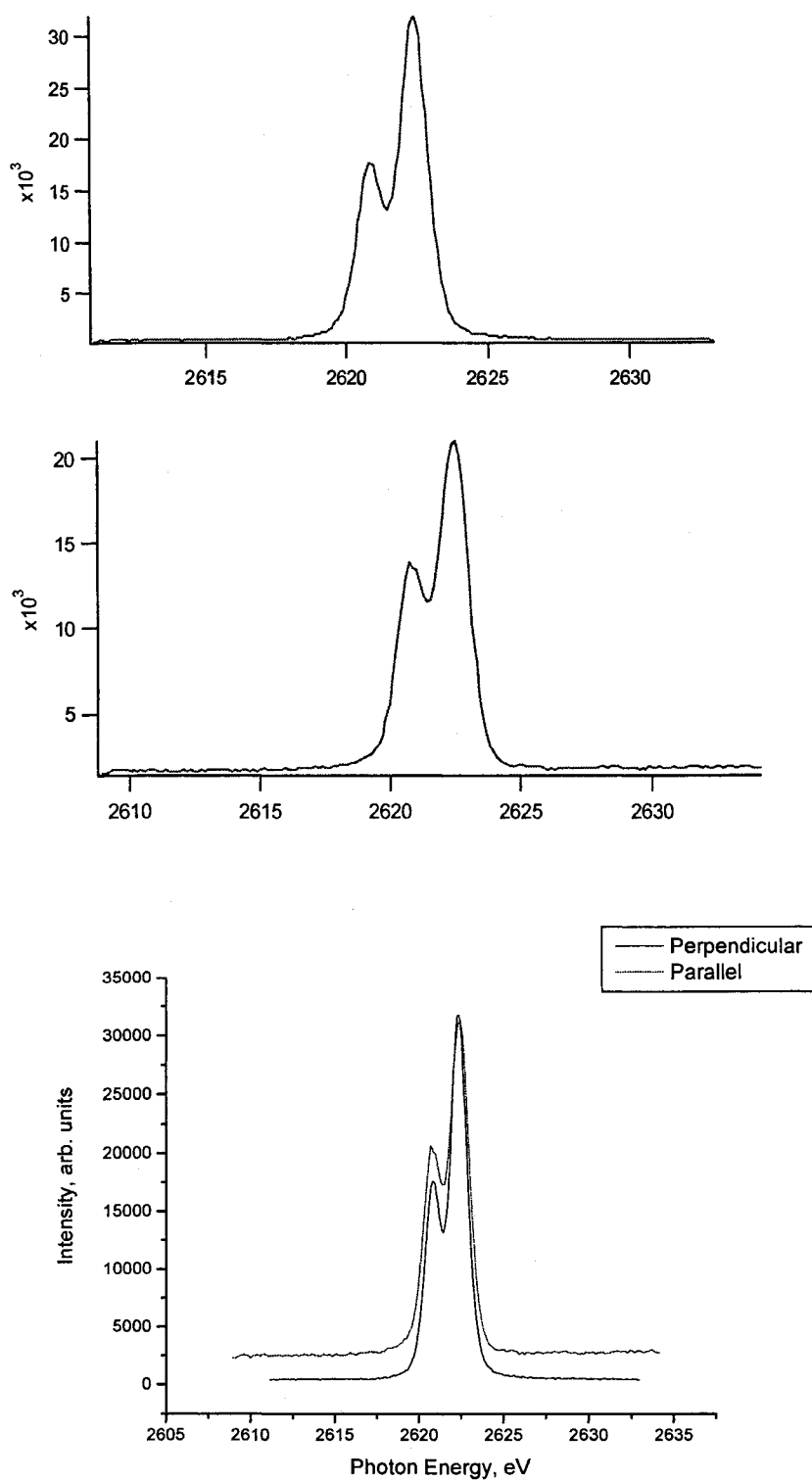


Figure 14. Perpendicular polarized x-ray emission spectrum (top) and parallel x-ray emission spectrum (middle) and a scaled comparison (bottom) taken at 2826 eV (Cl).

The next photon energy considered was 2830 eV; the same effect is seen here when comparing the perpendicular polarization to the parallel polarization: the perpendicular polarization has much narrower peaks with better separation. The height of α_1 is 21804 and α_2 is 12335 in the perpendicular and 6444 and 3977 in the parallel. This corresponds to the following ratios: 1.8/1 and 1.6/1, respectively. The total area under each curve is the following: 30646 and 17581 for perpendicular; 9128.2 and 5434.7 for the parallel orientation, which gives a ratio of 1.7/1 and 1.7/1, respectively. The widths of the peaks are approximately the same as for the measurements taken at 2826 eV; 1.2 eV in the perpendicular and 1.25 eV in the parallel direction; see Figure 15.

When the incident photon energy was 2832 eV, the perpendicular and the parallel polarizations look similar. At this energy, the height of α_1 is 24958 and α_2 is 13111 when the orientation is perpendicular and 6509 and 3701 when it is parallel; the height ratios are therefore 1.9/1 and 1.8/1, respectively. The total area under each curve is 35587 and 16249, with a ratio of 2.2/1 in the perpendicular direction and 8921.2 and 3998.5, which corresponds to a ratio of 2.2/1 in the parallel orientation. The width of the peaks in the perpendicular direction is 1.2 eV, and is the same in the parallel orientation; roughly the same as the two previous excitation energies. Resolution at increasing energies appears to be declining; the widths of the peaks are increasing in both polarizations; see Figure 16.

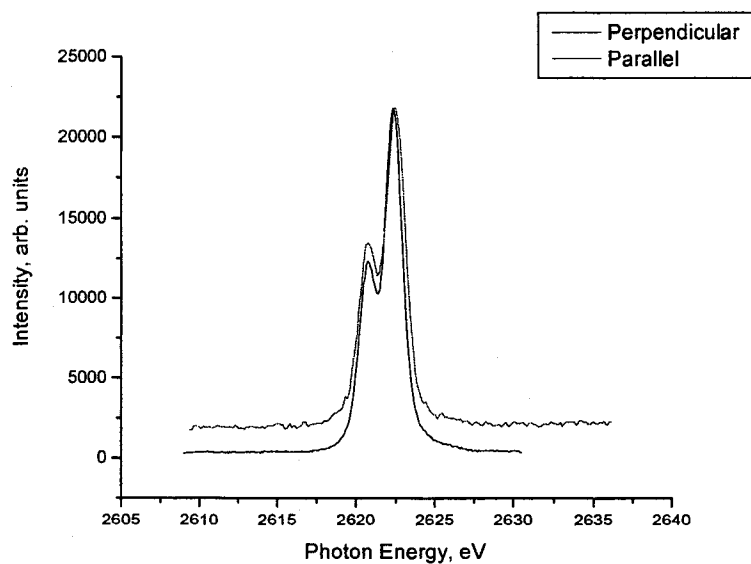
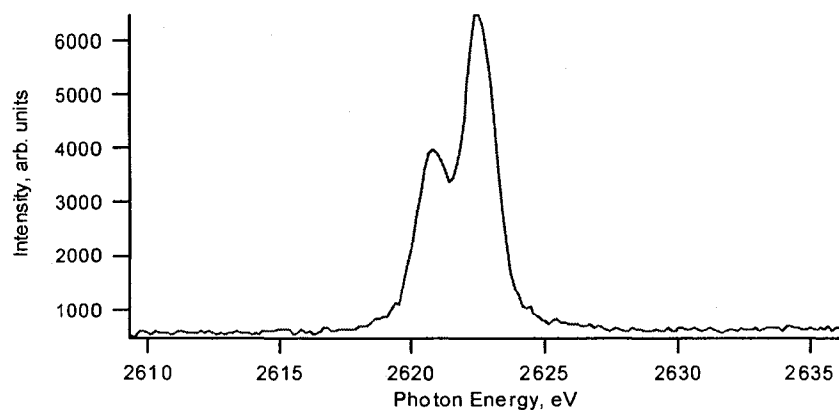
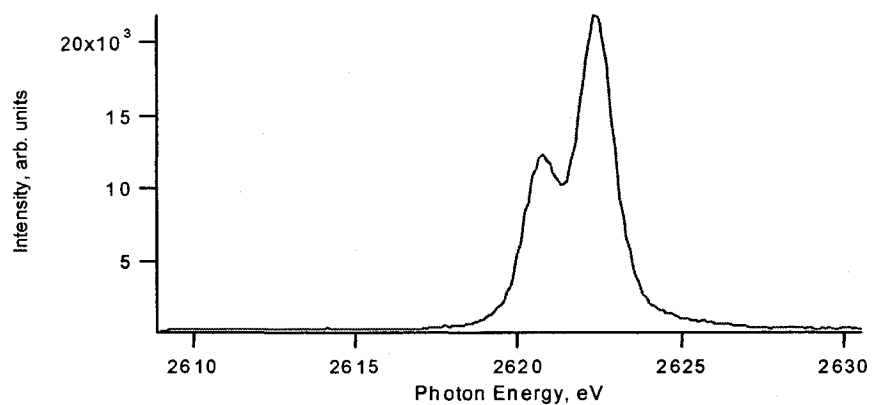


Figure 15. Perpendicular polarized x-ray emission spectrum (top) and parallel x-ray emission spectrum (middle) and a scaled comparison at 2830 eV (Cl).

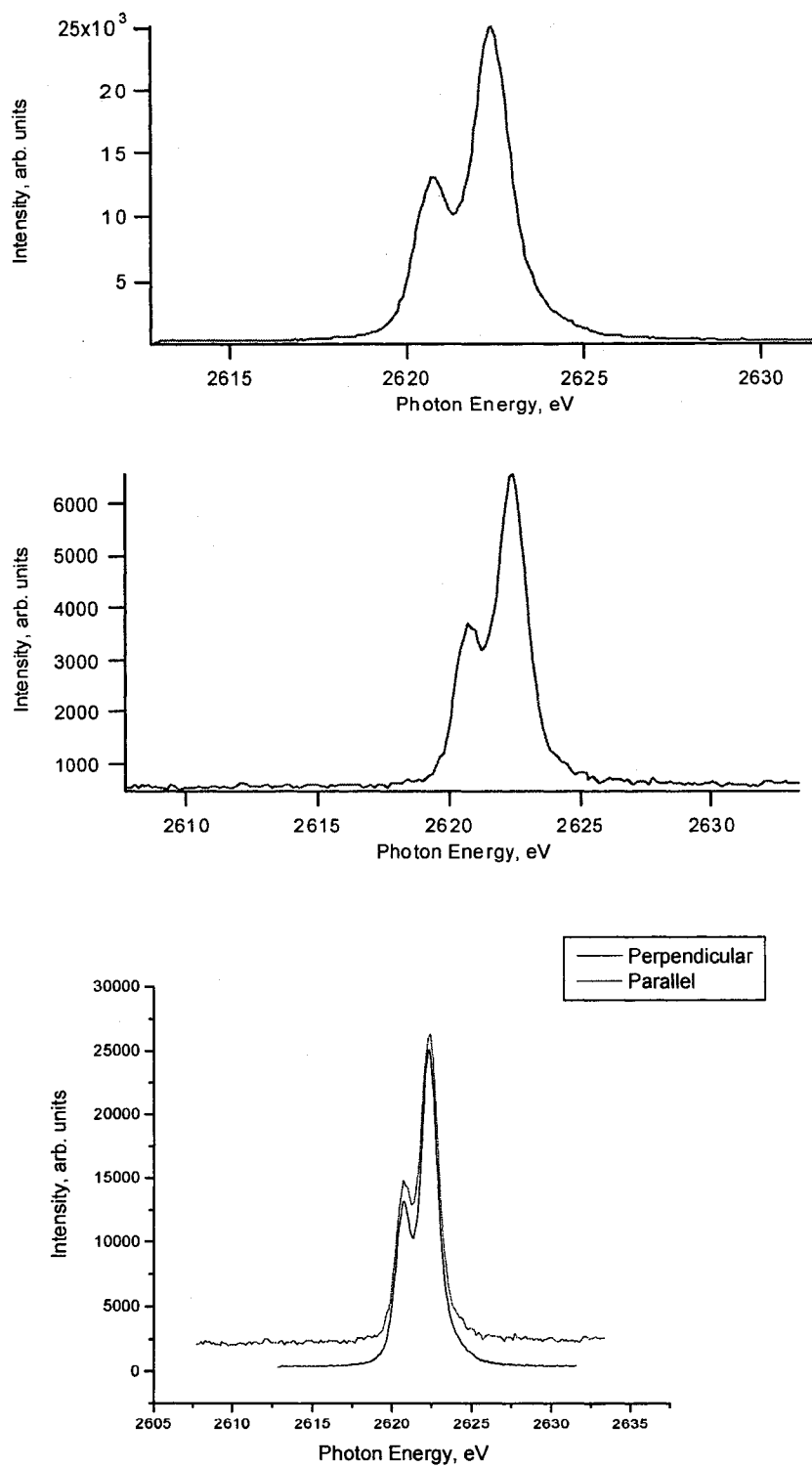


Figure 16. Perpendicular polarized x-ray emission spectrum (top) and parallel x-ray emission spectrum (middle) and a scaled comparison (bottom) at 2832 eV (Cl).

At the next photon energy, 2836.3 eV, the peaks have the same shape as the previous energy and the peaks are still separated by a wide gap. The height of α_1 is 20164 and α_2 has a height of 11426 in the perpendicular orientation and 4998 and 3063 when it is collecting the spectrum parallel; the height ratios are therefore 1.8/1 and 1.6/1, respectively. The total area under each curve is 28132 and 19490, which corresponds to a ratio of 1.4/1 in the perpendicular direction. For the parallel orientation, the total area is 6515.8 and 3522.1, which corresponds to a ratio of 1.8/1. The width of the peaks in the perpendicular direction is 1.2 eV, and 1.1 eV in the parallel orientation; roughly the same as the previous photon energy; see Figure 17.

At the higher incident photon energy of 2845.5 eV, the perpendicular and the parallel polarizations have become broader. At this energy, the height of α_1 is 40233 and α_2 is 23494 when the orientation is perpendicular; it is 5902 and 3658 when it is parallel; the height ratios are therefore 1.7/1 and 1.6/1, respectively. The total area under each curve is 66773 and 31334, with a ratio of 2.1/1 in the perpendicular direction and 8651.8 and 4365.1, which corresponds to a ratio of 2.0/1 in the parallel orientation. The width of the peaks in the perpendicular direction is 1.3 eV, and 1.3 eV in the parallel orientation; wider than all the previous excitation energies. When examining the spectra, the tails of the peaks take much longer to reach the background level in both polarizations. The gap separating the two peaks from one another is much narrower, this is most apparent in the parallel orientation; see Figure 18.

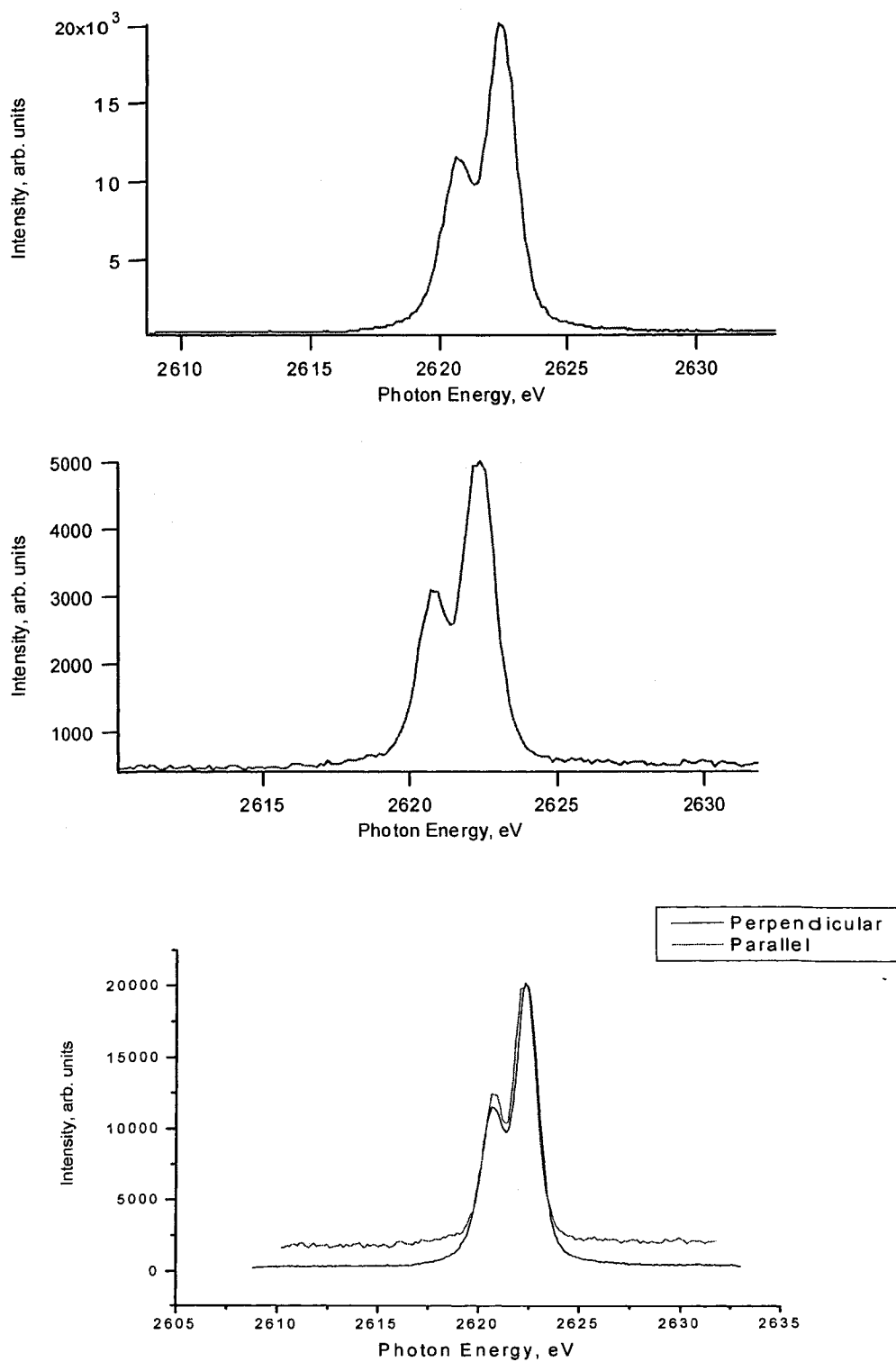


Figure 17. Perpendicular polarized x-ray emission spectrum (top) and parallel x-ray emission spectrum (middle) and a scaled comparison (bottom) at 2836.3 eV (Cl).

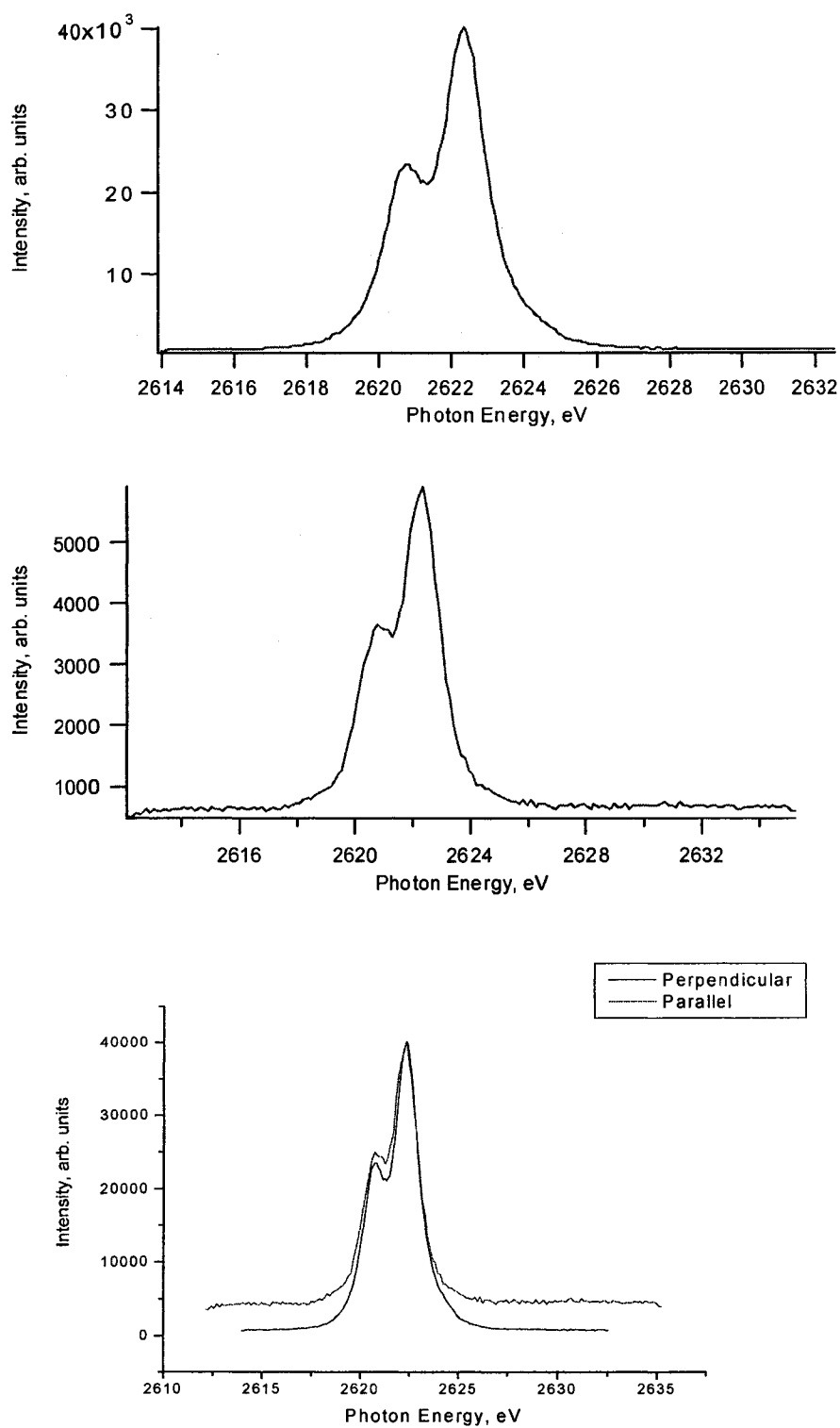


Figure 18. Perpendicular polarized x-ray emission spectrum (top) and parallel x-ray emission spectrum (middle) and a scaled comparison (bottom) at 2845.5 eV (Cl).

When the incident photon energy was 2853.2 eV, the perpendicular and the parallel polarizations look similar to those at 2845.5 eV. The height of α_1 is 51268 and α_2 is 30943 in the perpendicular orientation and 5321 and 3507 in the parallel; the height ratios are therefore 1.7/1 and 1.5/1, respectively. The total area under each curve is 81294 and 41186 in the perpendicular direction, with a ratio of 2.0/1 and 9479.3 and 4073.6, which corresponds to a ratio of 2.3/1 in the parallel orientation. Peak width in the perpendicular direction is 1.3 eV, and 1.5 eV in the parallel orientation; nearly the same as the previous excitation energy; the tails on both of the peaks are broader at this excitation energy; see Figure 19.

The final excitation energy considered is 2875 eV. This energy is well above the ionization threshold. At this photon energy, the height of α_1 is 60923 and the height of α_2 is 39007 when the orientation is perpendicular and 6536 and 3858 when it is measured parallel; the height ratios are therefore 1.6/1 and 1.7/1, respectively. The total area under each curve is 147000 and 45616, with a ratio of 3/1 in the perpendicular direction and 11981 and 3751.8, which corresponds to a ratio of 3/1 in the parallel orientation. At this high of an energy, the width of the peaks in the perpendicular direction is 1.6 eV, and 1.8 eV in the parallel orientation; slightly higher at this final energy. Peak shape and the broadness of the tails is also the same as in the two previous excitation energies; see Figure 20.

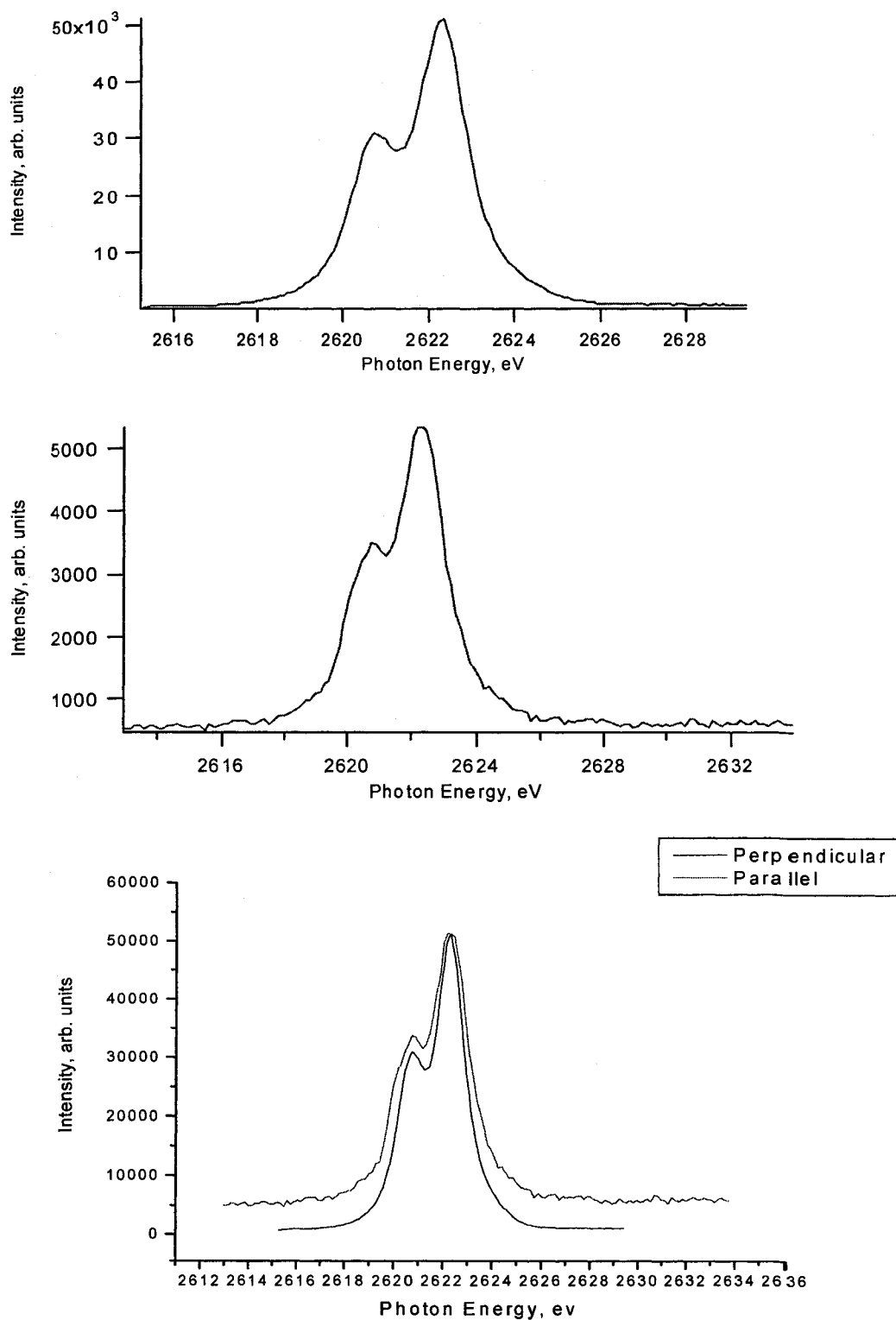


Figure 19. Perpendicular polarized x-ray emission spectrum (top) and parallel x-ray emission spectrum (middle) and scaled comparison (bottom) at 2853.2 eV (Cl).

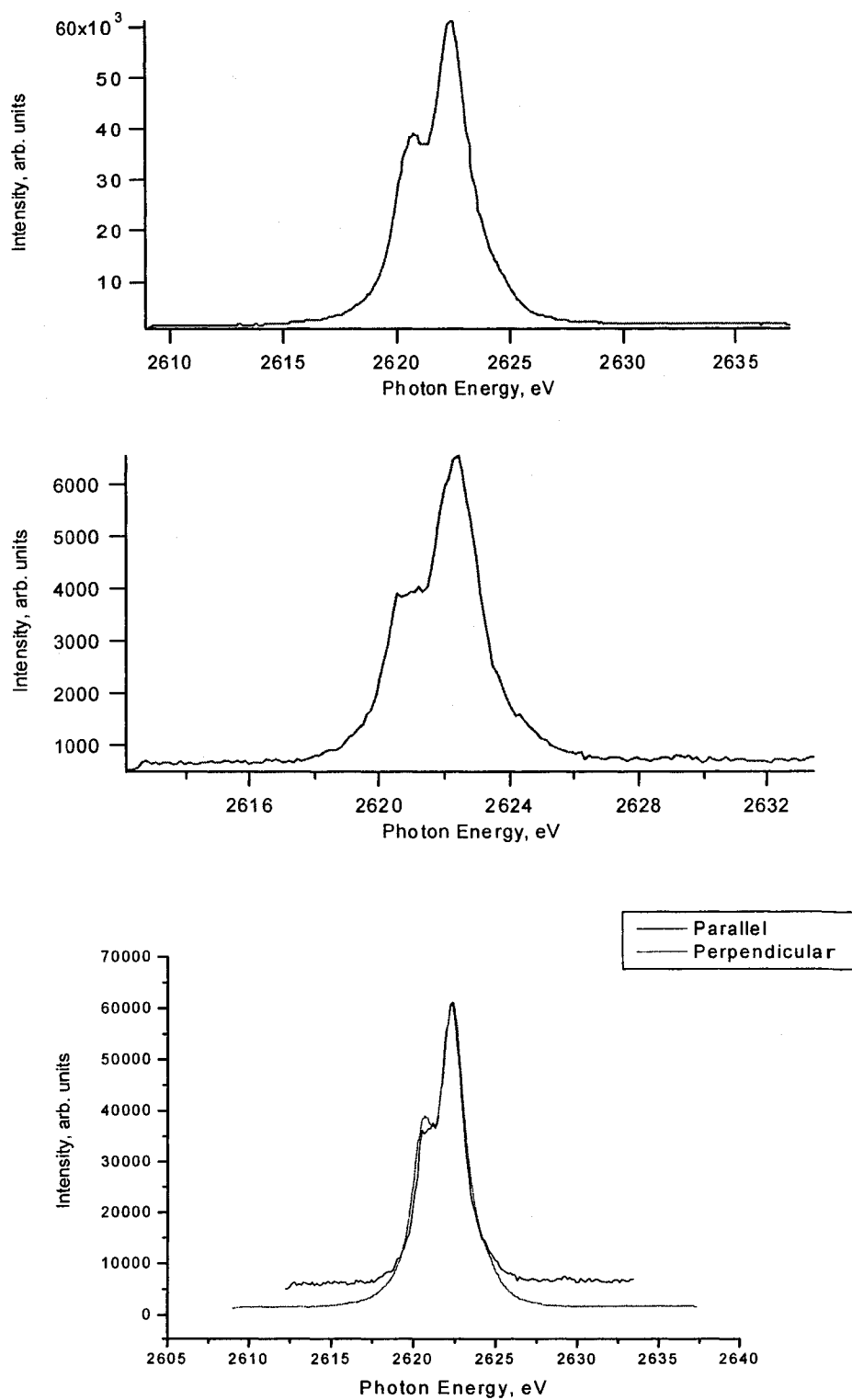


Figure 20. Perpendicular polarized x-ray emission spectrum (top) and parallel x-ray emission spectrum (middle) and a scaled comparison at 2875 eV (Cl).

Potassium Edge

The first energy examined near the potassium K-edge was 3612.4, an energy below the ionization threshold. In the parallel polarization, there is a better separation of α_1 and α_2 compared to the perpendicular polarization. However, both spectra have peaks with narrow tails. The height of α_1 is 5790 and α_2 is 2453 in the parallel direction and 12553 and 7717, respectively, in the perpendicular. This corresponds to a ratio of 2.4 to 1 in the parallel and 1.6 to 1 in the perpendicular. When comparing the total area under the two peaks, the parallel orientation yields are 11472 and 5218.8 and the perpendicular yields 40899 and 28069; this corresponds to the following ratios: 2.2/1 and 1.5/1, respectively. When comparing the widths, α_1 and α_2 are roughly the same; 1.6 eV in the parallel direction and 3.0 eV in the perpendicular; see Figure 21. It is obvious that there is better resolution in the parallel direction for this set of measurements.

At the next photon energy considered, 3616 eV, the same effect is seen when comparing the parallel polarization to the perpendicular polarization: the parallel polarization has much better separation of α_1 and α_2 . The height of α_1 is 4999 and α_2 is 2476 in the parallel and 15175 and 9396 in the perpendicular. This corresponds to the following ratios: 2.0/1 and 1.6/1, respectively. The total area under each curve is the following: 9359.5 and 5299.2 for the parallel direction; 44996 and 27959 for the perpendicular orientation, which gives a ratio of 1.8/1 and 1.6/1, respectively. The widths of the peaks are approximately the same as for the measurements taken at 2826 eV; 1.6 eV in the parallel and 2.6 eV in the perpendicular direction; see Figure 12.

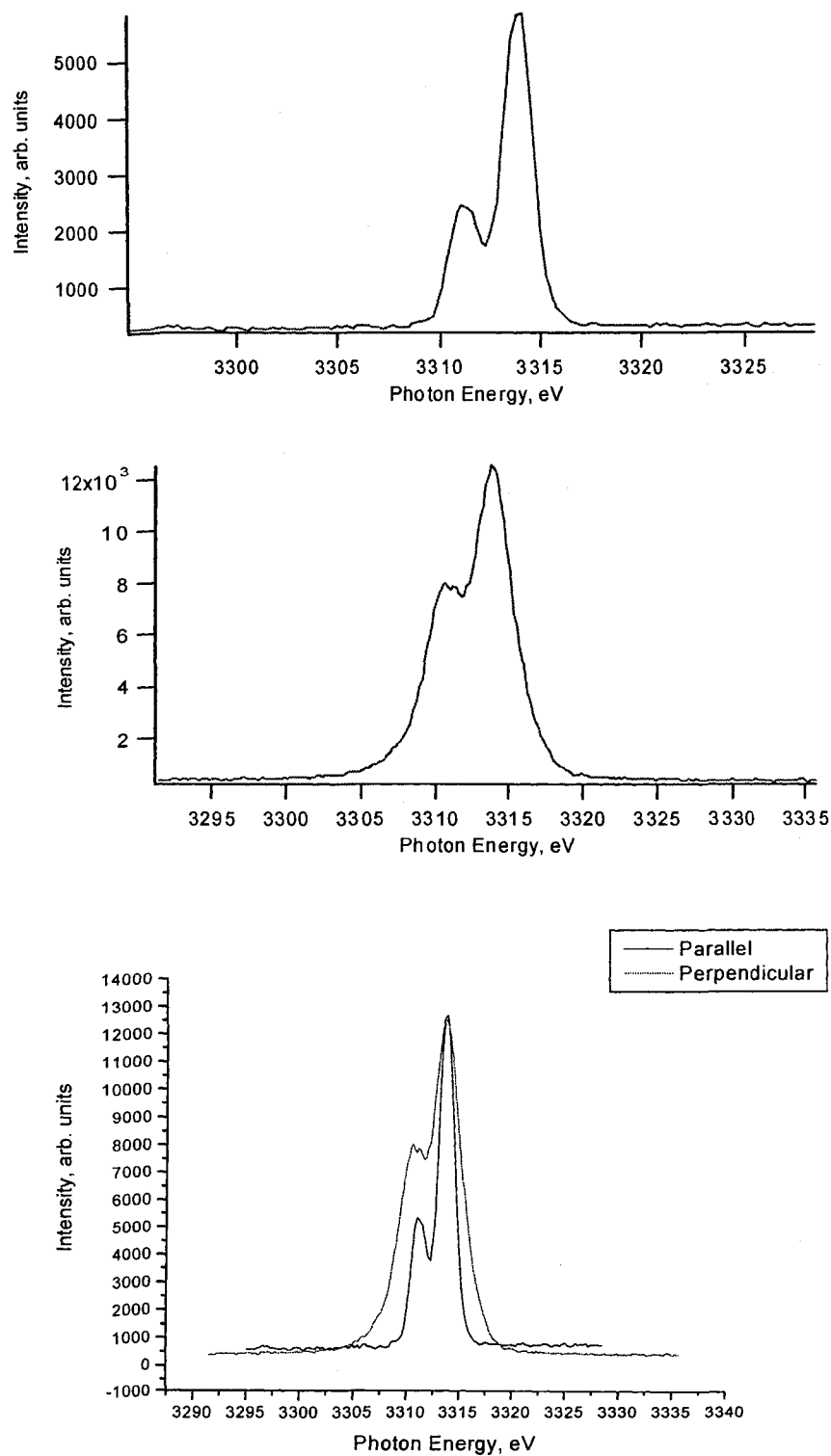


Figure 21. Parallel polarized x-ray emission spectrum (top) and perpendicular polarized x-ray emission spectrum (middle) and a scaled comparison (bottom) at 3612.4 eV (K).

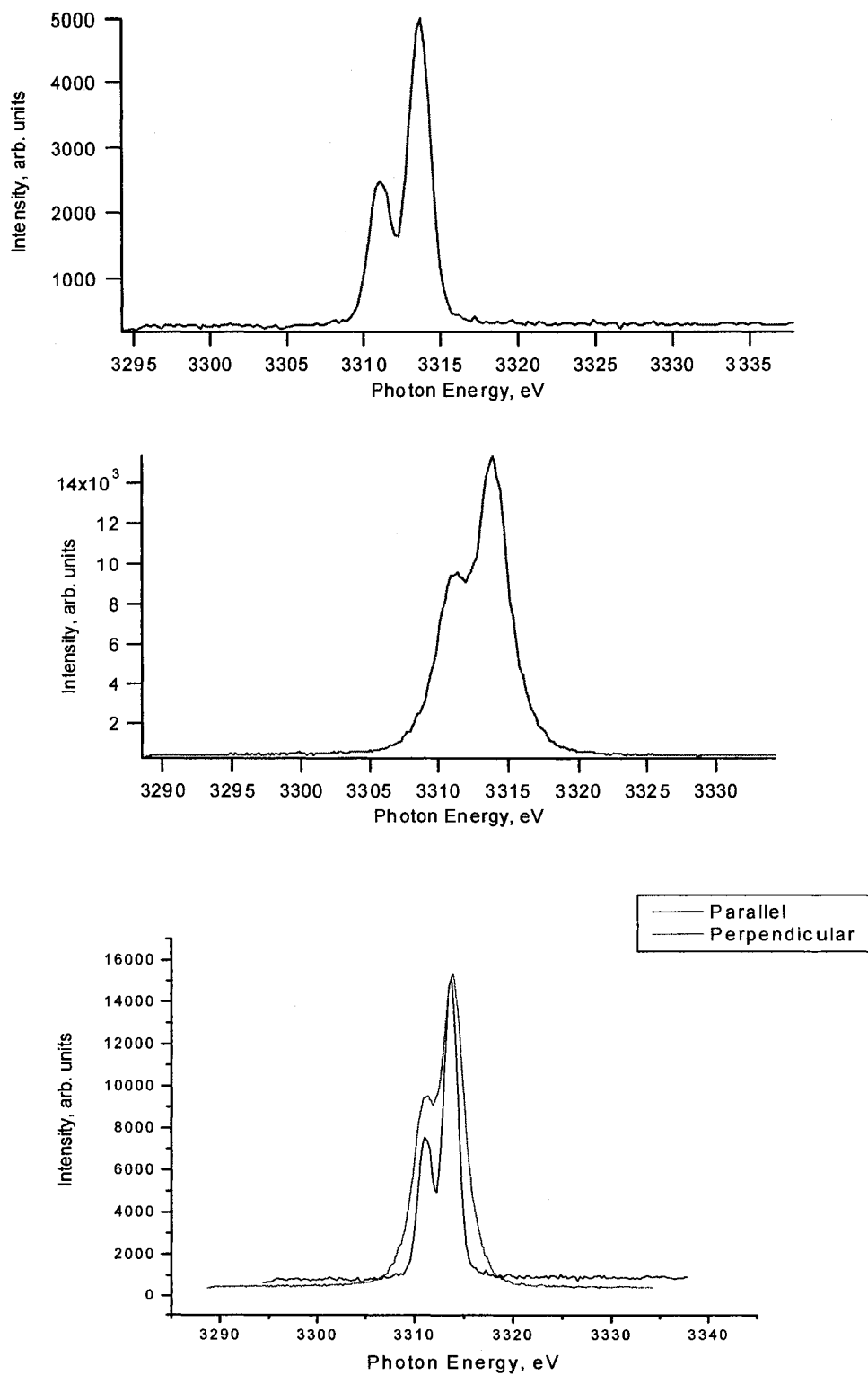


Figure 22. Parallel-polarized x-ray emission spectrum (top) and perpendicular polarized x-ray emission spectrum (middle) and a scaled comparison (bottom) at 3616 eV (K).

When the incident photon energy was 3618 eV, the parallel polarization looks similar to the two spectra before, but the perpendicular polarization has less separation of the two peaks. At this energy, the height of α_1 is 3914 and α_2 is 1774 when the orientation is parallel and 11401 and 6801 when it is perpendicular; the height ratios are therefore 2.2/1 and 1.7/1, respectively. The total area under each curve is 7782.8 and 3314.3, with a ratio of 2.3/1 in the parallel direction and 46075 and 15927, which corresponds to a ratio of 2.9/1 in the perpendicular orientation. The width of the peaks in the parallel direction is 1.7 eV, and 3.2 eV in the perpendicular orientation; roughly the same as the two previous excitation energies for the parallel orientation, but an increase for the perpendicular; see Figure 23.

At the next photon energy, 3621.4 eV, the peaks have the same shape as the previous energy in both orientations. The height of α_1 is 2675 and α_2 has a height of 1373 in the parallel orientation and 8853 and 5538 when it is in the perpendicular; the height ratios are therefore 1.9/1 and 1.6/1, respectively. The total area under each curve is 5589.7 and 2228.4, which corresponds to a ratio of 2.5/1 in the parallel direction. For the perpendicular orientation, the total area is 37876 and 13040, which corresponds to a ratio of 2.9/1. The width of the peaks in the parallel direction is 1.7 eV, and 3.4 eV in the perpendicular orientation; approximately the same as the previous photon energy; see Figure 24.

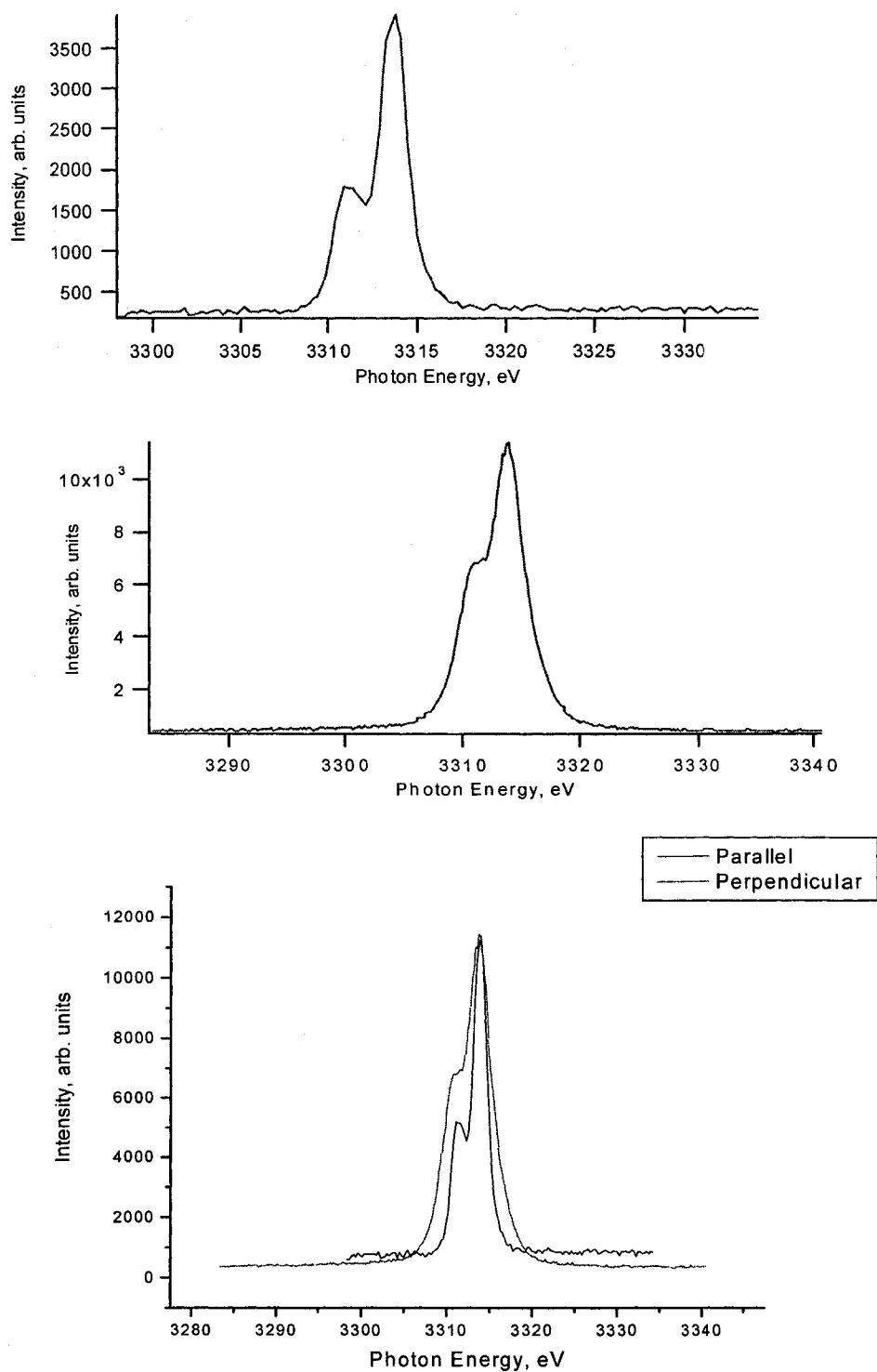


Figure 23. Parallel-polarized x-ray emission spectrum (top) and perpendicular polarized x-ray emission spectrum (middle) and a scaled comparison (bottom) at 3618 eV (K).

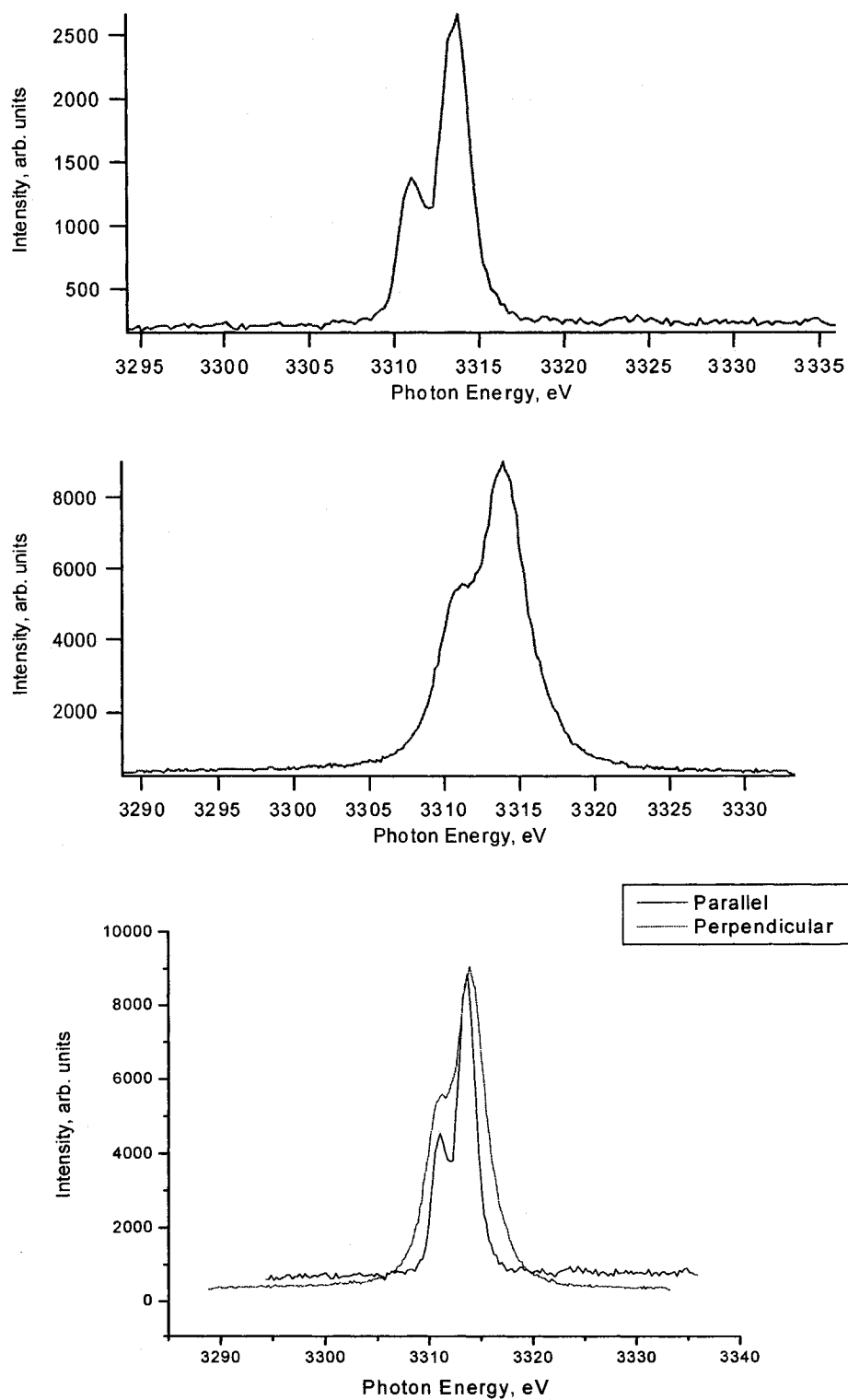


Figure 24. Parallel-polarized x-ray emission spectrum (top) and perpendicular polarized x-ray emission spectrum (middle) and a scaled comparison (bottom) at 3621.4 eV (K).

At the higher incident photon energy of 3629.1 eV, the parallel polarization has a narrower gap separating the two peaks; and the perpendicular polarization remains the same. At this energy, the height of α_1 is 3623 and α_2 is 1750 when the orientation is parallel; it is 7652 and 5047 when it is perpendicular; the height ratios are therefore 2.1/1 and 1.5/1, respectively. The total area under each curve is 8259.3 and 3449.5, with a ratio of 2.4/1 in the parallel direction and 29543 and 16060, which corresponds to a ratio of 1.8/1 in the perpendicular orientation. The width of the peaks in the parallel direction is 1.9 eV, and 3.4 eV in the perpendicular orientation; slightly larger in the parallel direction than the previous measurement. The gap separating the two peaks from one another still remain wide in the parallel orientation; see Figure 25.

When the incident photon energy was 3645 eV, the perpendicular and the parallel polarizations look similar to those at 3629.1 eV. The height of α_1 is 4547 and α_2 is 2273 in the parallel orientation and 6613 and 4248 in the perpendicular; the height ratios are therefore 2.0/1 and 1.6/1, respectively. The total area under each curve is 10638 and 4227.0 in the parallel direction, with a ratio of 2.5/1 and 26200 and 9619.8, which corresponds to a ratio of 2.7/1 in the perpendicular orientation. Peak width in the parallel direction is 1.9 eV, and 3.5 eV in the perpendicular orientation; nearly the same as the previous excitation energy; the tails on both of the peaks are broader at this excitation energy; see Figure 26.

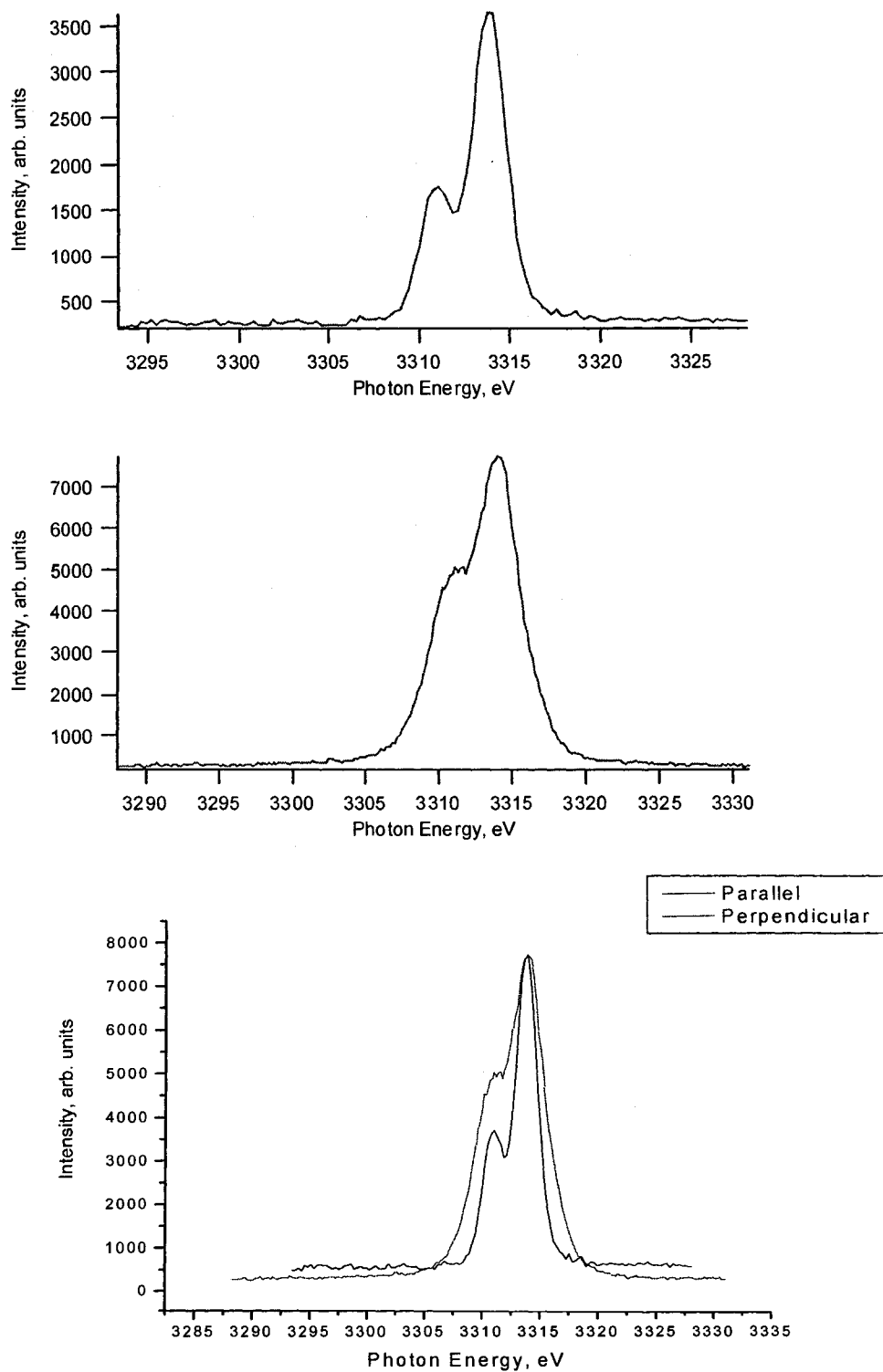


Figure 25. Parallel-polarized x-ray emission spectrum (top) and perpendicular polarized x-ray emission spectrum (middle) and a scaled comparison (bottom) at 3629.1 eV (K).

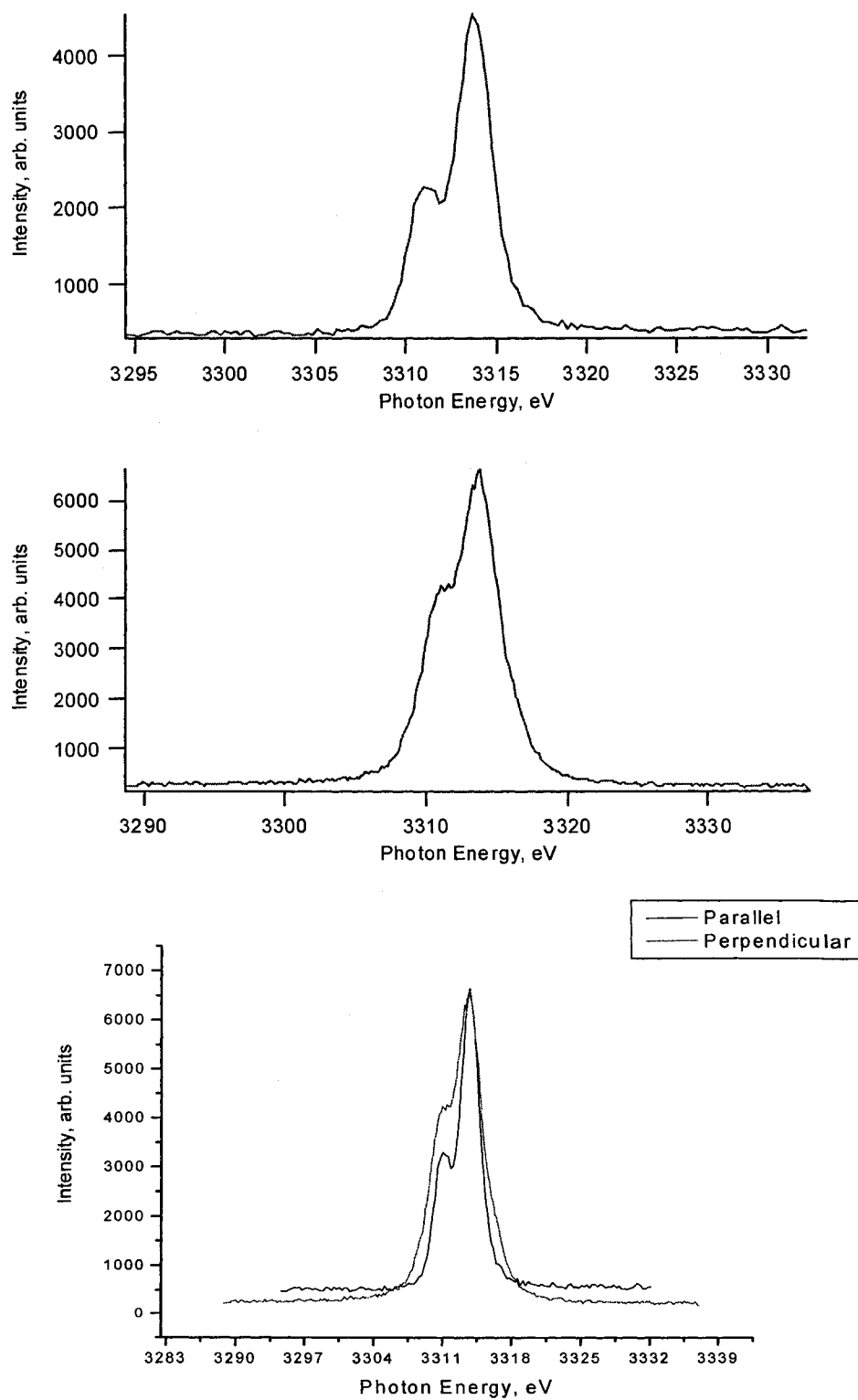


Figure 26. Parallel-polarized x-ray emission spectrum (top) and perpendicular polarized x-ray emission spectrum (middle) and a scaled comparison (bottom) at 3645 eV (K).

The final excitation energy considered is 3670 eV. This energy is presumed to be well above the ionization threshold. At this photon energy, the height of α_1 is 9807 and the height of α_2 is 5767 when the orientation is parallel and 14538 and 8946 when it is measured perpendicular; the height ratios are then 1.7/1 and 1.6/1, respectively. The total area under each curve is 29148 and 10300, with a ratio of 2.8/1 in the parallel direction and 62859 and 17791, which corresponds to a ratio of 3.5/1 in the perpendicular orientation. At this high energy, the width of the peaks in the parallel direction is 2.4 eV, and 3.6 eV in the perpendicular orientation; more or less the same as the two previous excitation energies. The separation of α_1 and α_2 is much narrower at this energy. The first peak, α_2 , almost appears as a shoulder; see Figure 27.

Freon-13

An absorption scan was run for freon-13 from 2810 eV to 2900 eV. From this scan, five energies were chosen to measure the x-ray emission spectra in both polarizations. The major pre-threshold feature seen in the absorption spectrum (2824.3 is attributed to the Cl 1s electrons being promoted to the $11a_1$ molecular antibonding orbital. The feature seen at 2828.7 eV corresponds to a Cl 1s electron being excited to the $4p$ Rydberg and the feature seen at 2830.0 corresponds to transition to the np Rydbergs. The chlorine ionization threshold occurs at 2831 eV, so the measurements taken at 2845 eV and 2875 eV occur above threshold [16-17]; see Figure 28.

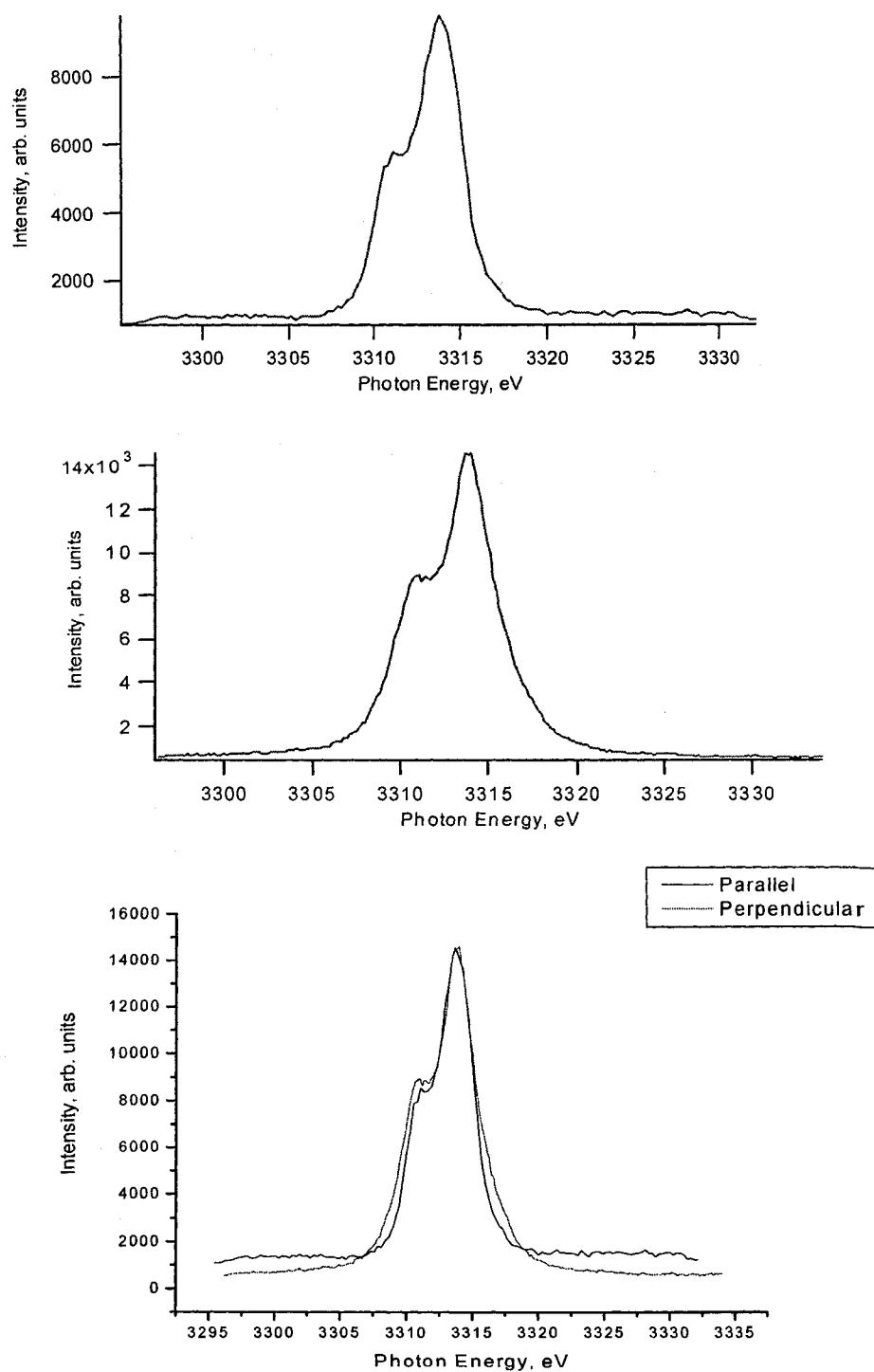


Figure 27. Parallel-polarized x-ray emission spectrum (top) and perpendicular polarized x-ray emission spectrum (middle) and a scaled comparison (bottom) at 3670 eV (K).

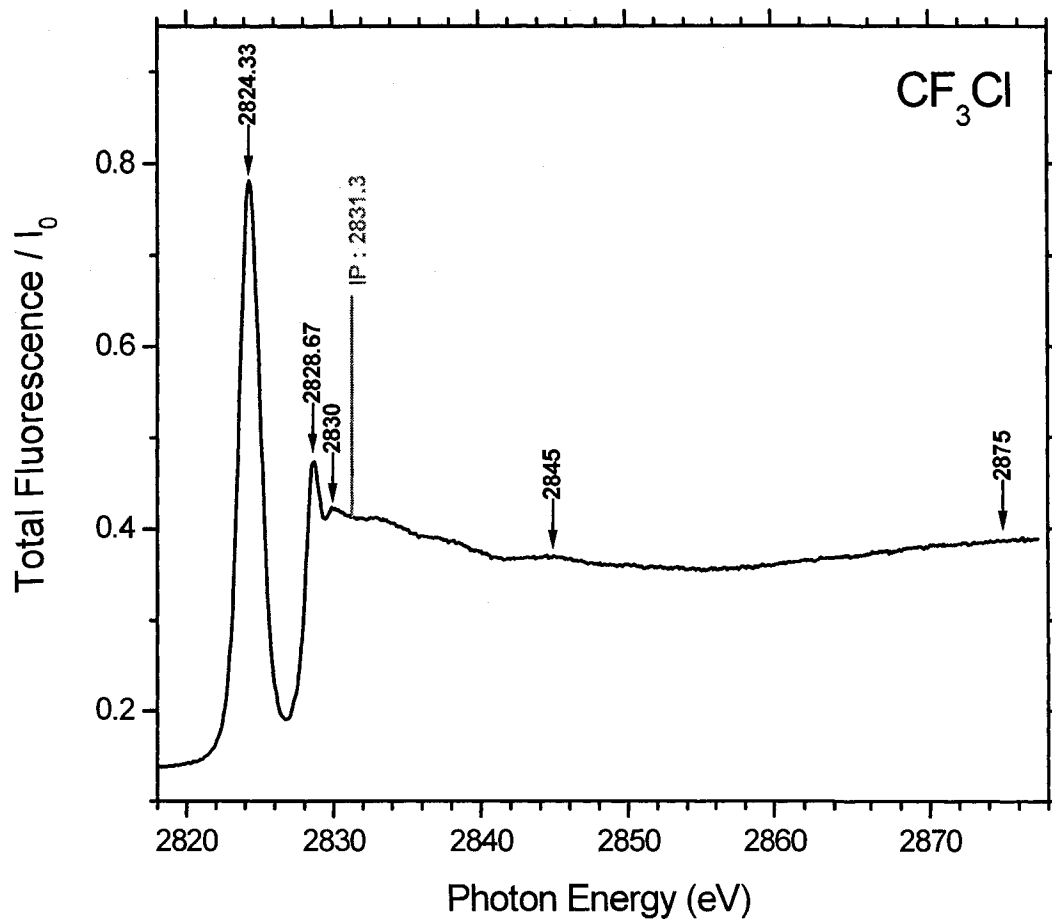


Figure 28. NEXAFS scan near the chlorine K-edge in CF_3Cl .

The first set of emission spectra were taken with the incident photon energy of 2824.3 eV, or on the $1s \rightarrow 11a_1$ resonance. The perpendicular and the parallel spectra look very similar; both have good separation of α_1 and α_2 . The top image in Figure 29 corresponds to the perpendicular polarized emission spectrum; α_1 has a height of 9084 and α_2 has a height of 6640. The bottom image is the emission spectrum taken in the

parallel polarization; α_1 has a height of 900 and α_2 has a height of 656. Both of the polarization directions have the same height ratio, 1.4/1. The area under α_1 is $1.88 \cdot 10^5$ and α_2 is $1.411 \cdot 10^5$ with a ratio of 1.33/1 in the perpendicular direction. In the parallel direction, the areas are 7549.6 and 5239.8 with a ratio of 1.44/1. The width of the peaks is 1.1 eV in the both the perpendicular polarized spectrum and the parallel polarized spectrum.

At the next pre-edge feature, $h\nu = 2828.7$, the spectra look similar to those on the main resonance. The height of α_1 is 4556 and α_2 2862 in the perpendicular direction; which gives a ratio of 1.60/1. In the parallel polarization, the height is 960 for α_1 and 535 for α_2 ; the height ratio is then 1.8/1. The total areas under the peaks in the perpendicular direction are 74305 and 59553, respectively. In the parallel direction they are 7528.6 and 4808.6. The intensity ratios at this energy are therefore 1.25/1 and 1.57/1. The widths of these peaks are roughly the same as in the previous energy; both polarizations having a width of 1.2 eV; see Figure 30.

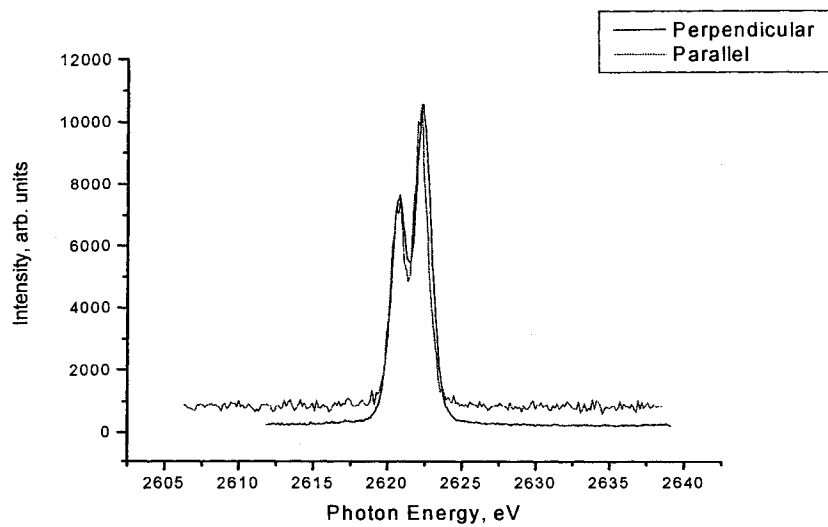
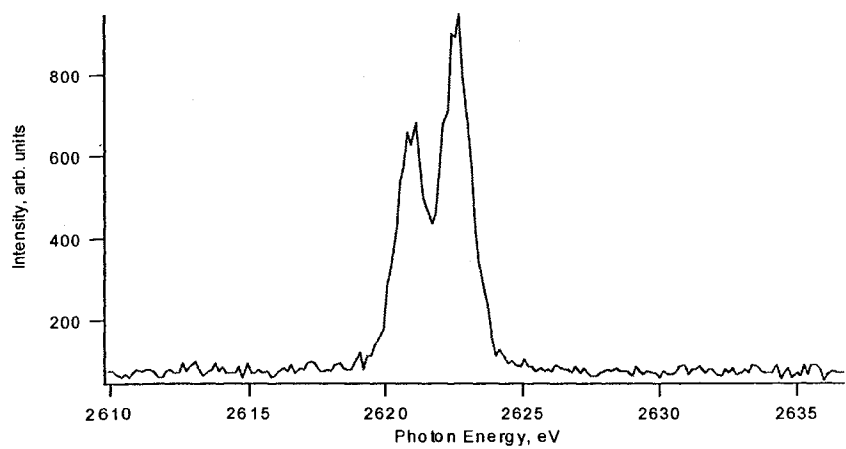
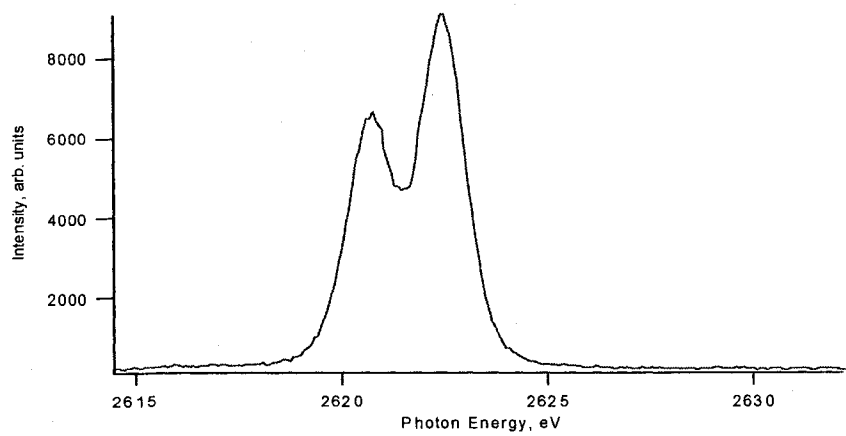


Figure 29. Perpendicular polarized x-ray emission spectrum (top) and parallel polarized x-ray emission spectrum (middle) and a scaled comparison (bottom) at 2824.3 eV (freon).

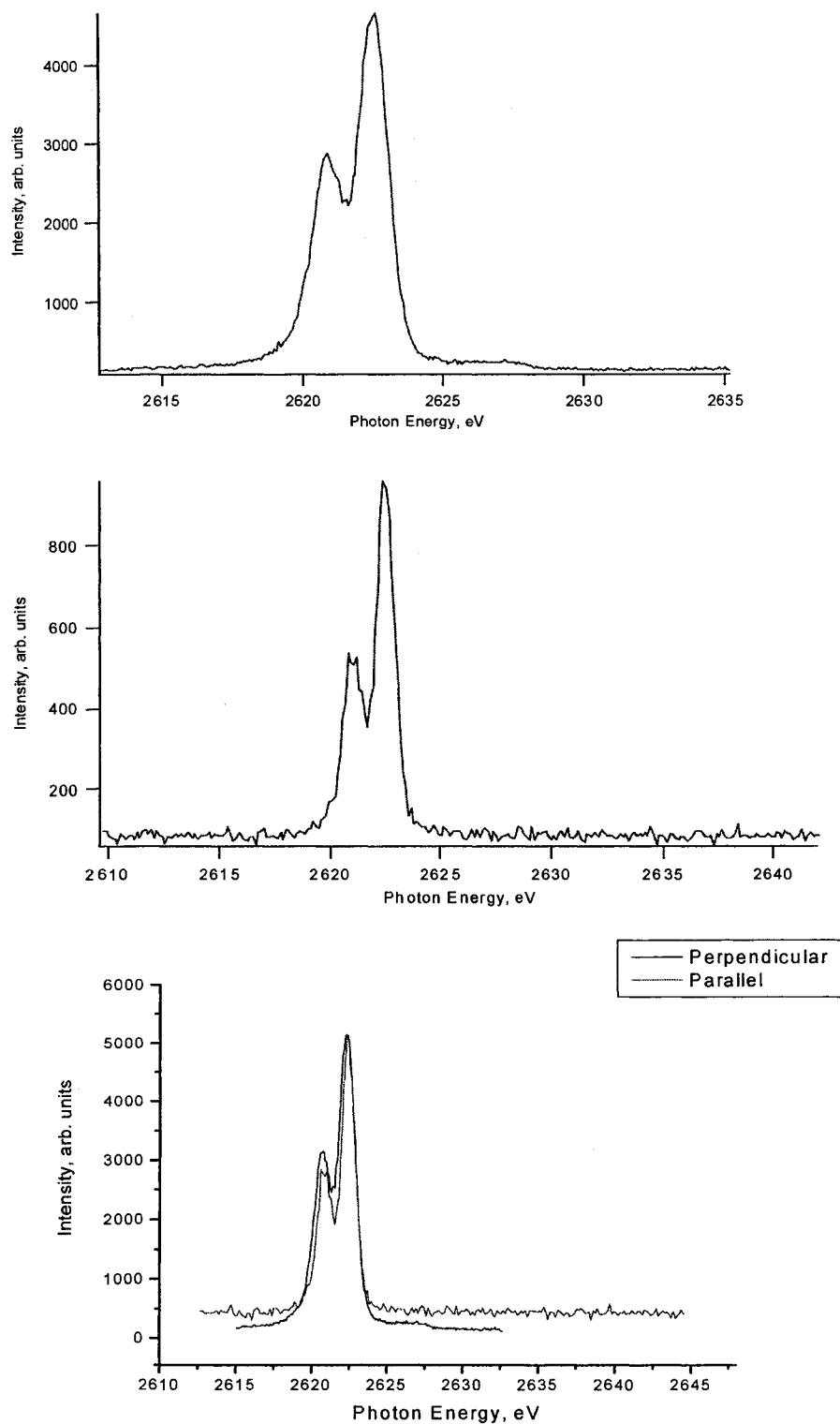


Figure 30. Perpendicular polarized x-ray emission spectrum (top) and parallel polarized x-ray emission spectrum (middle) and a scaled comparison (bottom) at 2828.7 eV (freon).

The last pre-edge energy considered in this work corresponds to an excitation energy of 2830.0 eV. At this energy, there is still a clear separation of both of the emission peaks, but it isn't as well defined as the two previous energies. The height of α_1 is 3452 and α_2 2050 in the perpendicular direction; this gives a ratio of 1.68/1. In the parallel polarization, the height is 936 for α_1 and 507 for α_2 ; the height ratio is then 1.85/1. The areas for the perpendicular direction are 68118 and 39934, respectively. In the parallel direction they are 2604.9 and 1083.4. The intensity ratios at this energy are therefore 1.70/1 and 2.40/1. The widths of these peaks are slightly different, it is 1.3 eV in the perpendicular polarization and 1.0 eV in the parallel; see Figure 31.

The excitation energy of 2845 is above the ionization threshold for this molecule at the Cl K-edge. The height of α_1 is 2359 and α_2 1396 in the perpendicular direction; this gives a ratio of 1.70/1. In the parallel polarization, the height is 849 for α_1 and 531 for α_2 ; the height ratio is then 1.60/1. The areas for the perpendicular direction are 87659 and 38365, respectively. In the parallel direction they are 8279.4 and 3167.5. The intensity ratios at this energy are therefore 2.28/1 and 2.20/1. The width of these peaks is the same in each orientation, or 1.7 eV; see Figure 32. At excitation energies above the ionization threshold, the shapes of the peaks are not as clearly defined. This is most noticeable in the parallel polarization where the two emission peaks are starting to merge together.

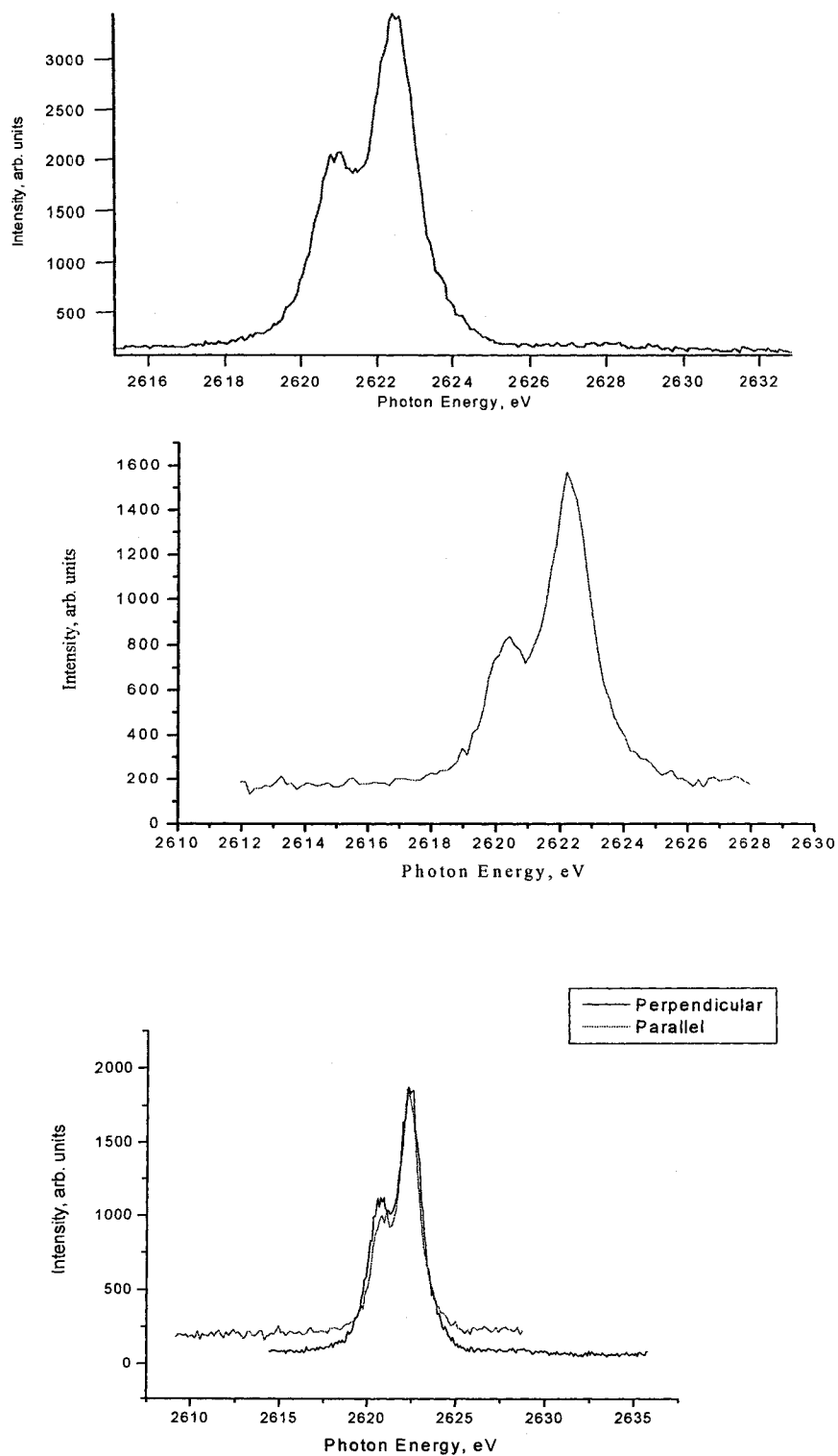


Figure 31. Perpendicular polarized x-ray emission spectrum (top) and parallel polarized x-ray emission spectrum (middle) and a scaled comparison (bottom) at 2830 eV (freon).

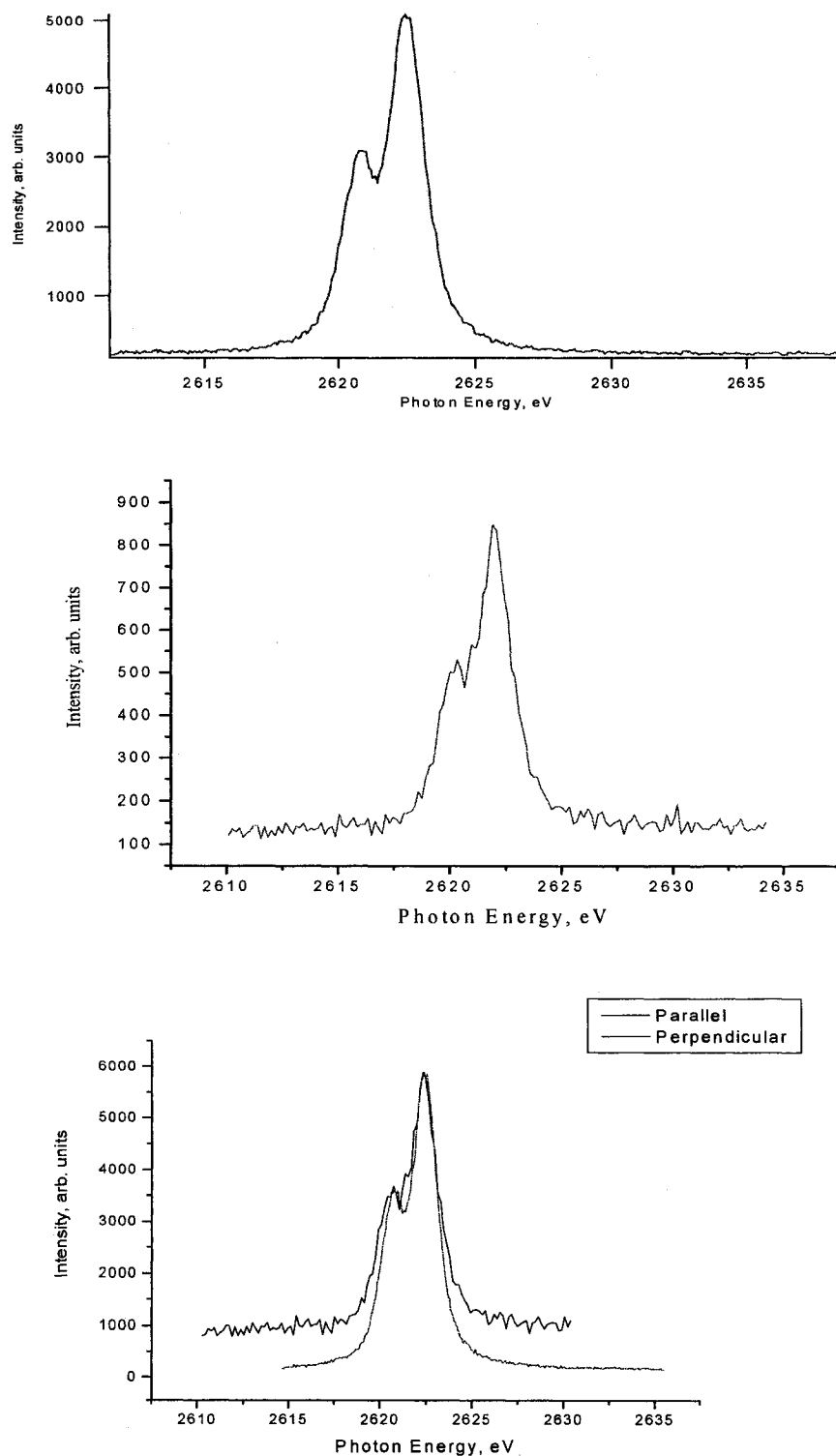


Figure 32. Perpendicular polarized x-ray emission spectrum (top) and parallel polarized x-ray emission spectrum (middle) and a scaled comparison (bottom) at 2845 eV (freon).

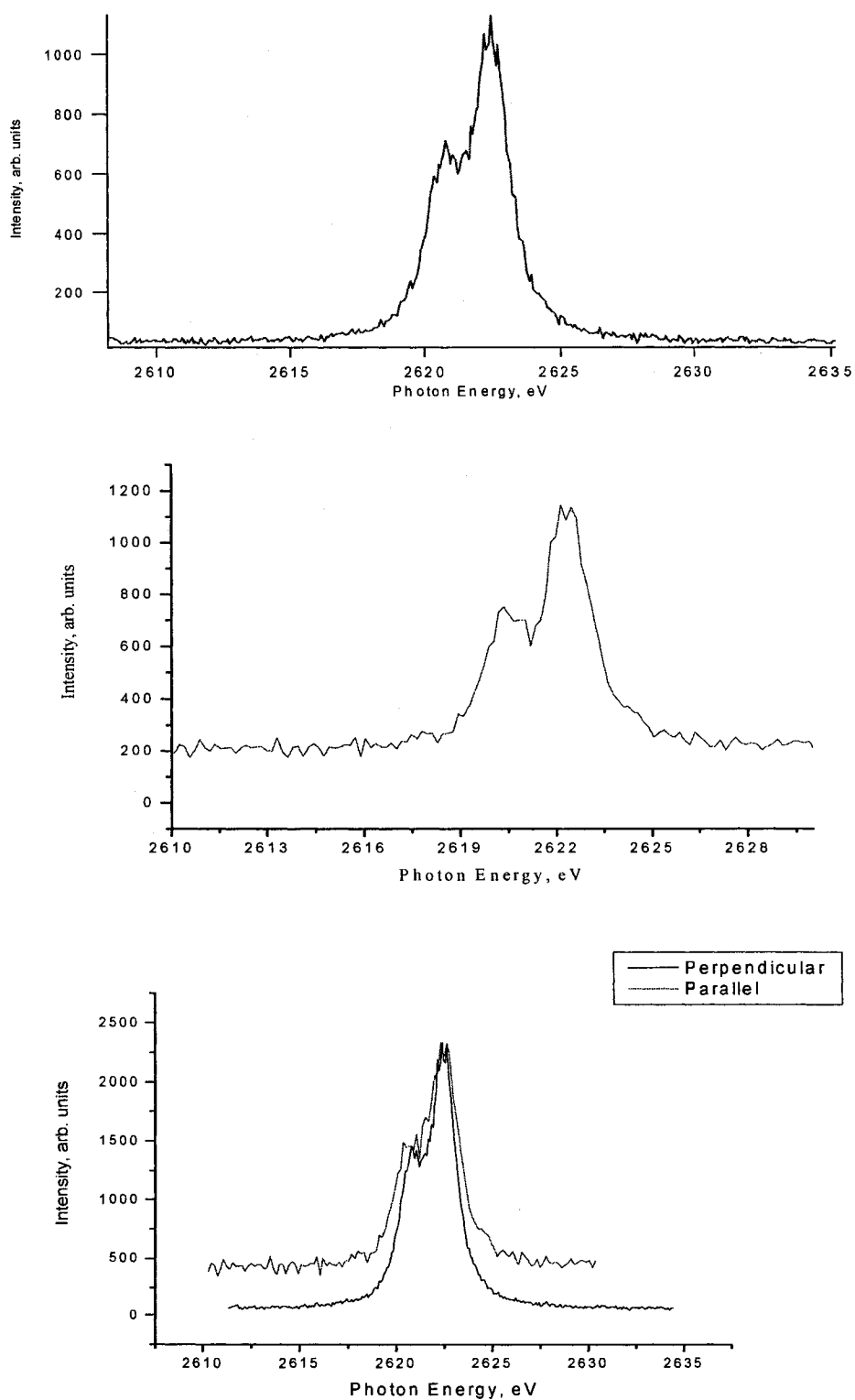


Figure 33. Perpendicular polarized x-ray emission spectrum (top) and parallel polarized x-ray emission spectrum (middle) and a scaled comparison (bottom) at 2875 eV (freon).

CHAPTER 6

CONCLUSION

When looking at the Cl K α emission spectra originating from solid KCl, it appears that the light collected in the perpendicular orientation yields well-resolved α_1 and α_2 emission spectra as opposed to that collected in the parallel orientation. The emission spectra in the perpendicular orientation were collected with the crystal slit most of the way out; so that most of the crystal was then being used to collect the spectra. The parallel polarized light was collected with the slit approximately 1 mm from the face of the crystal. With the slit in, only the center portion of the crystal is being utilized, and the energy resolution depends less on the curvature of the crystal. When the potassium emission spectra were collected, the opposite trend was seen. The parallel polarized potassium spectra were collected with the slit less than 1 mm away from the face, limiting the area of the crystal being used to a very small section, and improving resolution. Because the energy resolution is worse in the parallel orientation in the Cl spectra with the slit farther out, it is suspected that the crystal-bending device is not functioning properly. The purpose of the crystal bender is to focus the photons of the same energy striking the entire length of the crystal on to the same position on the detector, so it is possible that the crystal is bending into an ellipse instead of a circular arc.

Because of this issue, a full comparison of the solid KCl emission spectra is limited. The intensity ratios for the Cl K α spectra are consistent, around 1.7/1 in the perpendicular and in the parallel below threshold, and approximately 2 to 1 ratio above the threshold. From this data the ionization threshold is between 2836.3 eV and 2845.5, the parallel and the perpendicular spectra are more isotropic in the last three photon energies with approximately a 2 to 1 ratio. There is a small, if any, polarization dependence below the ionization threshold at the Cl-edge in KCl.

The same can be said for the potassium measurements, with the experimental settings used, a full comparison cannot be made. The first four photon energies seem to show a strong polarization dependence and the last two photon energies, 3645 eV and 3670 eV, seem to be more isotropic. Based on this information, the ionization threshold for potassium occurs between 3629.1 eV and 3645 eV.

There is also small polarization dependence of the gas-phase data collected. Above the ionization threshold, $h\nu = 2845$ and 2875 eV, the x-ray emission intensity is isotropic; the initial excitation does not produce a sample with its symmetry axes oriented in the direction of the synchrotron-radiation polarization direction. Emission intensity is therefore expected to be isotropic. Emission intensities are not as isotropic in the subthreshold regions, although the effect is small. On the main absorption feature, the intensity ratios are 1.3/1 in the perpendicular and 1.4/1 in the parallel, 1.2/1 and 1.6/1 when the excited photon is to the 4*p* Rydberg, and 1.7/1 and 2.4/1 when the excitation occurs to *np* Rydberg states. From these measurements, it is suggested that the greatest polarization effects for the Cl K α emission occur when the initial excitation is to more

atomic Rydberg states, however, more evidence and better resolved spectra are needed to further test this.

These are the first sets of measurements to originate from the x-ray emission spectrometer. They have been most useful as a diagnostic tool, to help indicate specific problems in the emission spectrometer, especially with the faulty crystal bender and the data acquisition program. A more advanced data gathering program will be needed, one that will start and stop with the storage ring refills and change the monochromator energy, and further tests will need be run to fine-tune the XES so that data will be more accurate, and the x-ray emissions are better focused onto the detector.

APPENDIX I

CHARACTER TABLES FOR C_{2v} AND C_{3v} MOLECULES

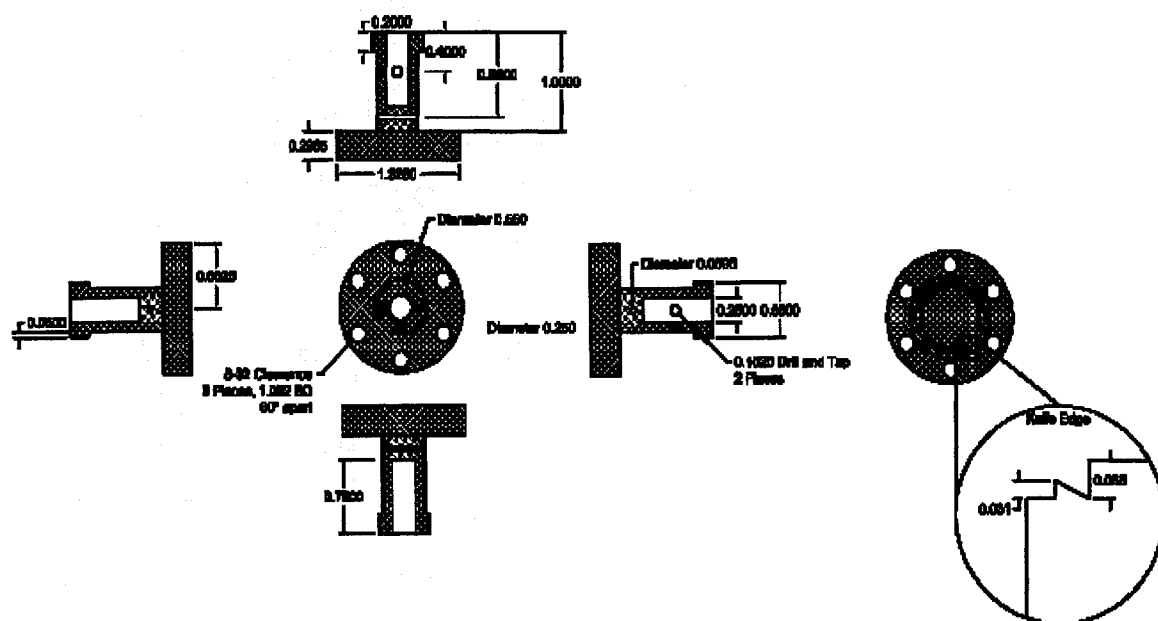
Character Tables:

C_{2v}	E	C_2	σ_v	σ_v'
A_1	1	1	1	1
A_2	1	1	-1	-1
B_1	1	-1	1	1
B_2	1	-1	-1	1

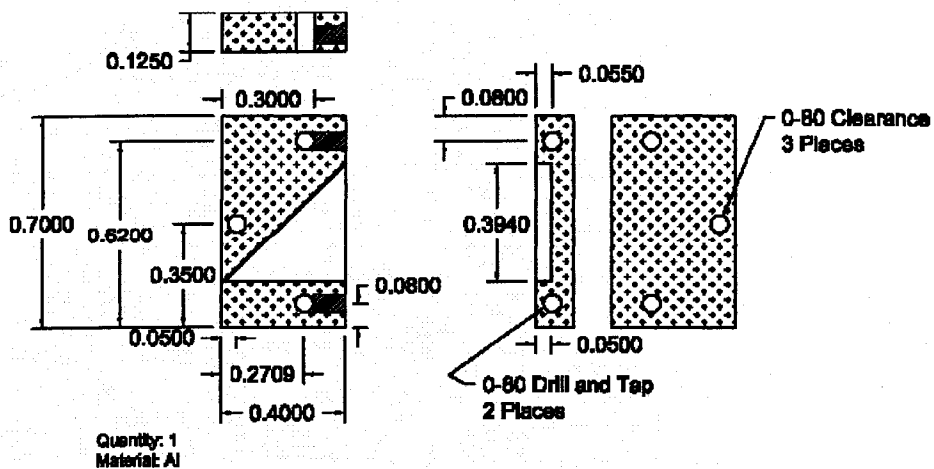
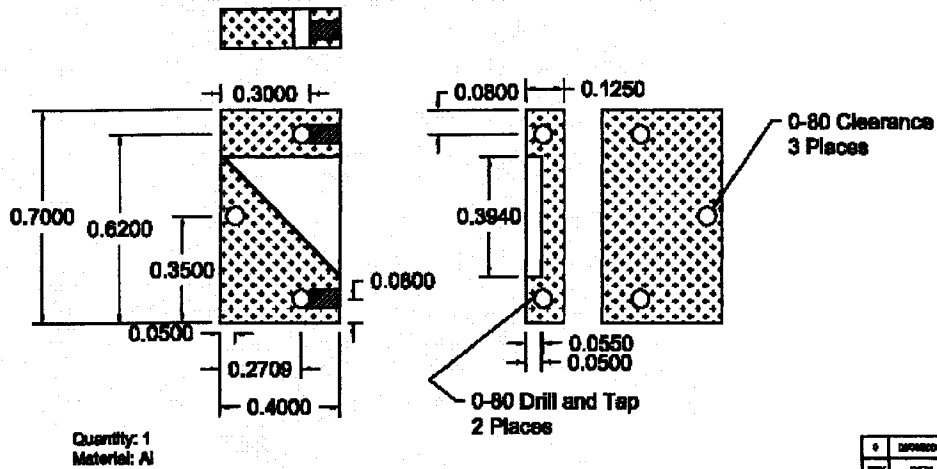
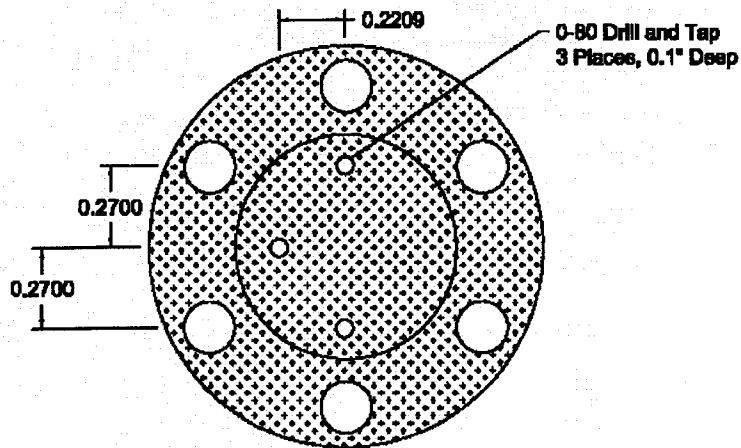
C_{3v}	E	$2C_3$	$3\sigma_v$
A_1	1	1	1
A_2	1	1	-1
E	2	-1	0

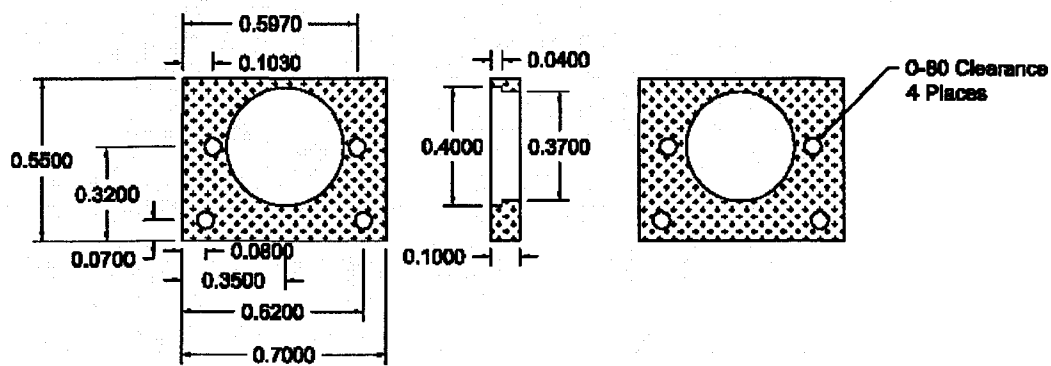
APPENDIX II

AUTOCAD DRAWING OF THE VARIOUS GAS CELL PARTS

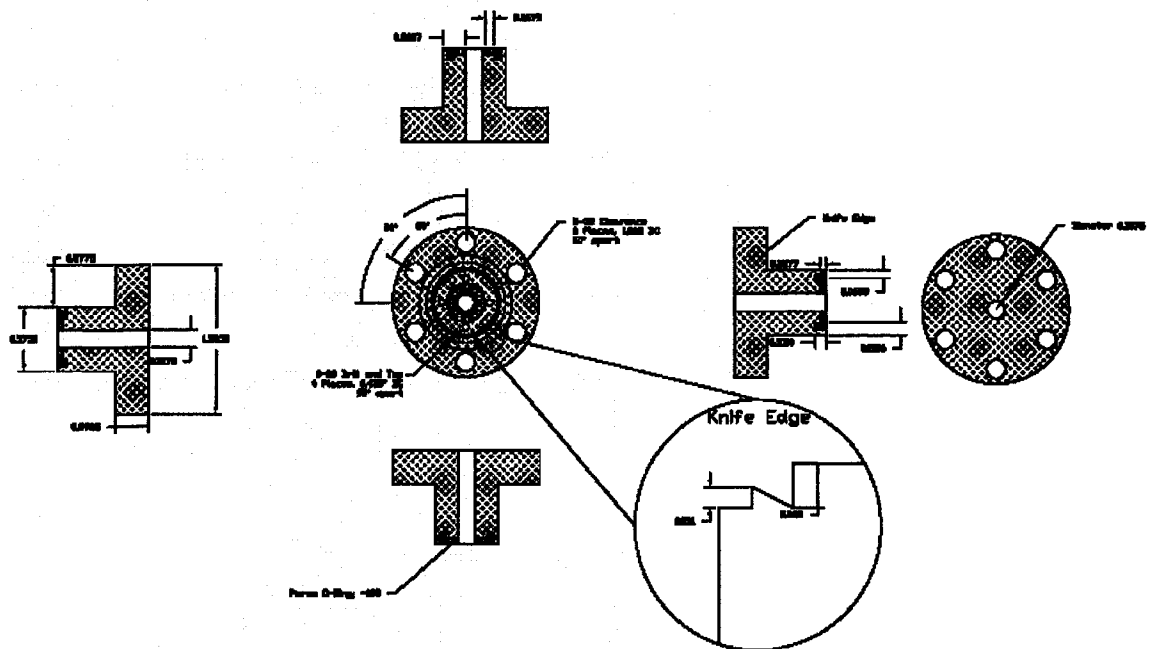


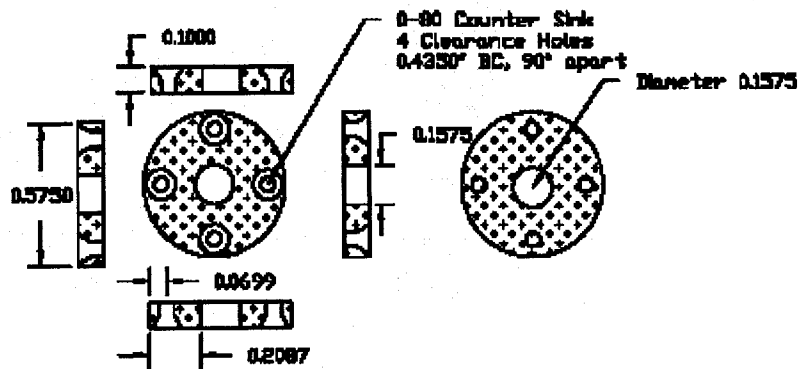
Gas Cell Mount: Holds the gas cell onto the sample manipulator.



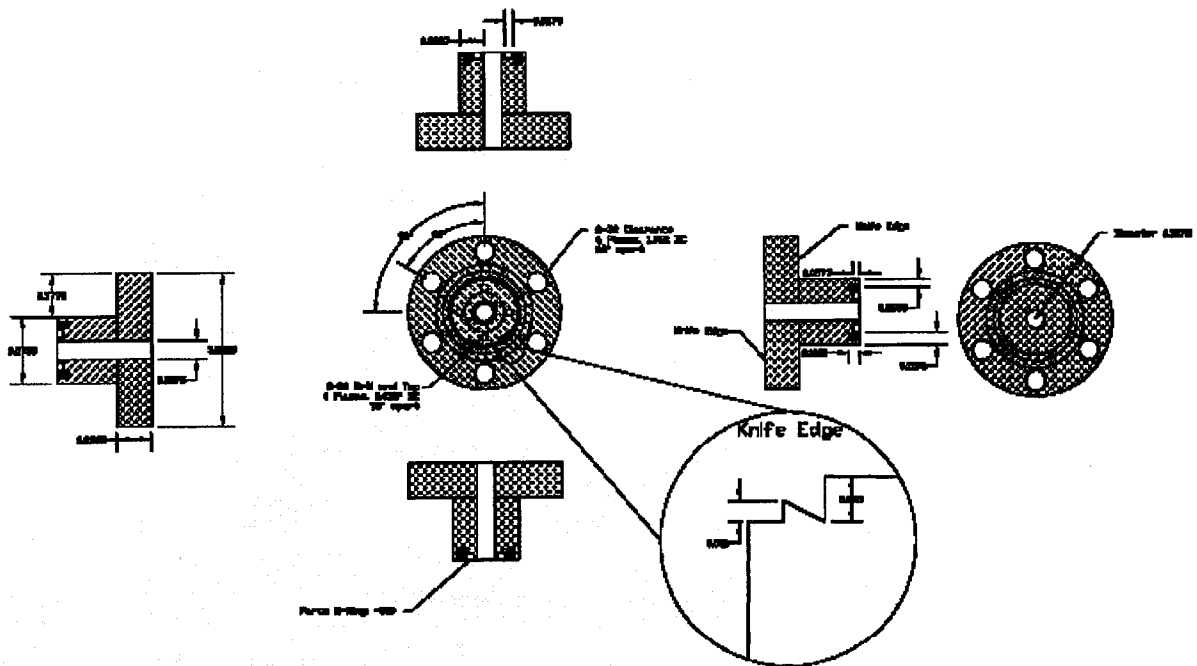


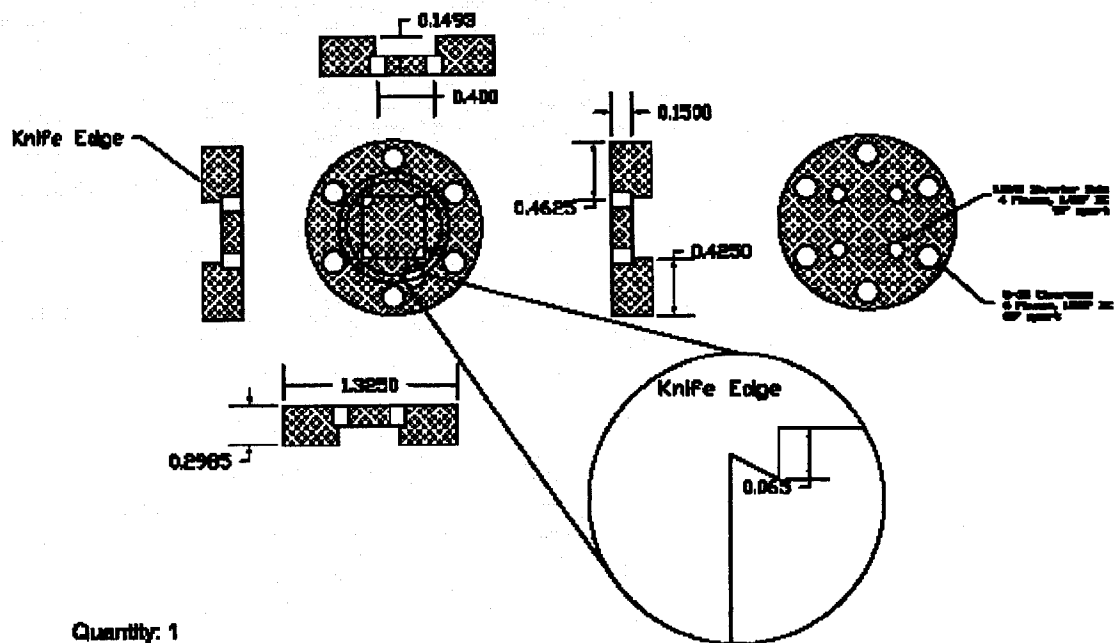
YAP Crystal and Prism Mount: these four pieces hold the crystal and prism below the gas cell and used to set the focus of the beamline.





Entrance Window Mount: (top) stainless steel piece that attaches to the cube, and
(bottom) aluminum piece where the window is glued.





Exit Window Mount and the Diode Mount: the diode to take absorption scans it attached to the back of the cube (downstream) from the entrance window.

REFERENCES

- [1] K. R. Wilson, J. G. Tobin, A. L. Ankudinov, J. J. Rehr, and R. J. Saykally, *Phys. Rev. Lett.* 85, 20 (2000).
- [2] V. L. Shneerson, W. T. Tysoe, and D. K. Saldin, *Phys. Rev. B.* 53, 15 (1996).
- [3] I. A. Levine, *Quantum Chemistry* (Prentice Hall, New Jersey, 2000).
- [4] M. A. Ratner and G. C. Schatz, *Introduction to Quantum Mechanics in Chemistry* (Prentice Hall, New Jersey, 2001).
- [5] P. W. Atkins and R. S. Friedman, *Molecular Quantum Mechanics* (Oxford University Press, New York, 1997).
- [6] J. Nordgren, P. Glans, K. Gunnelin, J.-H Guo, P. Skytt, C. S  the, and N. Wassdahl, *App. Phys. A* 65, 97 (1997).
- [7] P. Glans, P. Skytt, K. Gunnelin, J.-H Guo, J. Nordgren, F. Gel'mukhanov, A. Cesar, and H.   gren, *J. Elcetr. Spectr. Rel. Phenom.* 82, 3 (1996).
- [8] P. Glans, K. Gunnelin, P. Skytt, J.-H Guo, N. Wassdahl, J. Nordgren, H.   gren, F. Gel'mukhanov, T. Warwick, and E. Rotenberg, *Phys. Rev. Lett.* 76, 14 (1996).
- [9] A. Cesar, F. Gel'mukhanov, Y. Luo, H.   gren, P. Skytt, P. Glans, J.-H Guo, K. Gunnelin and J. Nordgren, *J. Chem. Physics* 106, 9 (1997).
- [10] P. Skytt, P. Glans, J.-H Guo, K. Gunnelin, C. S  the, J. Nordgren, F. Gel'mukhanov, A. Cesar and H.   gren, *Phys. Rev. Lett.* 77, 25 (1996).
- [11] K. Gunnelin, P. Glans, P. Skytt, J.-H Guo, J. Nordgren and H.   gren, *Phys. Rev. A* 57, 2 (1998).
- [12] P. Skytt, P. Glans, K. Gunnelin, J.-H Guo, J. Nordgren, Y. Luo and H.   gren, *Phys. Rev. A* 55, 1 (1997).
- [13] P. Skytt, P. Glans, K. Gunnelin, J.-H Guo and J. Nordgren, *Phys. Rev. A* 55, 1 (1997).
- [14] D. W. Lindle, P. L. Cowan, R. E. LaVilla, T. Jach, R. D. Deslattes, B. Karlin, J. A. Sheehy, T. J. Gil, and P. W. Langhoff, *Phys. Rev. Lett.* 60, 11 (1988).

- [15] D. W. Lindle, P. L. Cowan, T. Jach, R. E. LaVilla, R. D. Deslattes and R. C. C. Perera, Phys. Rev. A 45, 5 (1991).
- [16] S. H. Southworth, D. W. Lindle, R. Mayer, and P. L. Cowan, Phys. Rev. Lett. 67, 9 (1991).
- [17] R. C. C. Perera, P. L. Cowan, D. W. Lindle, R. E. LaVilla, T. Jach, and R. D. Deslattes, Phys. Rev. A 43, 7 (1991).
- [18] R. Mayer, D. W. Lindle, S. H. Southworth, and P. L. Cowan, Phys. Rev. A 43, 1 (1991).
- [19] J.-H Guo, Y. Luo, A. Augustsson, J.-E. Rubensson, C. S  the, H.   gren, H. Siegbahn, and J. Nordgren, Phys. Rev. Lett. 89, 13 (2002).
- [20] J. D. Mills, J. A. Sheehy, T. A. Ferrett, S. H. Southworth, R. Mayer, D. W. Lindle and P. W. Langhoff, Phys. Rev. Lett. 79, 3 (1997).

VITA

Graduate College
University of Nevada, Las Vegas

Amanda Hudson

Home Address:

819 Arrowhead Trail
Henderson, Nevada 89015

Degrees:

Bachelor of Science in Chemistry, 2001
University of Nevada, Reno

Publications:

O. Hemmers, R. Guillemin, E. P. Kanter, B. Krässig, D. W. Lindle, S. H. Southworth, R. Wehlitz, J. Baker, A. Hudson, M. Lotrakul, D. Rolles, W. C. Stolte, I. C. Tran, A. Wolska, S. W. Yu, M. Ya. Amusia, K. T. Cheng, L. V. Chernysheva, W. R. Johnson, and S. T. Manson. *Dramatic Nondipole Effects in Low-Energy Photoionization: Experimental and Theoretical Study of Xe 5s*. Phys. Rev. Lett. 91, 5 (2003).

Thesis Title: The Design and Performance of an X-Ray Emission Spectrometer using the Polarized K α Spectra of Chlorine and Potassium.

Thesis Examination Committee:

Chairperson, Dr. Dennis W. Lindle, Ph. D.
Committee Member, Dr. Boyd W. Earl, Ph. D.
Committee Member, Dr. Vernon F. Hodge, Ph. D.
Graduate College Representative, Dr. James C. Selser, Ph. D.